











## Modeling the High-Energy Ionizing Output from Simple Stellar and X-ray Binary Populations

KRISTEN GAROFALI <sup>1,2</sup> ANTARA R. BASU-ZYCH <sup>1,3,4</sup> BENJAMIN D. JOHNSON,<sup>5</sup> PANAYIOTIS TZANAVARIS,<sup>3,4,6</sup>  
ANNE JASKOT <sup>7</sup>, CHRIS T. RICHARDSON <sup>8</sup>, BRET D. LEHMER <sup>9</sup>, MIHOKO YUKITA <sup>2</sup>, EDMUND HODGES-KLUCK <sup>1</sup>,  
ANN HORNSCHEMEIER <sup>1</sup>, ANDREW PTAK <sup>1</sup> AND NEVEN VULIC <sup>10</sup>

<sup>1</sup>NASA Goddard Space Flight Center, Code 662, Greenbelt, MD 20771, USA

<sup>2</sup>William H. Miller III Department of Physics and Astronomy, Johns Hopkins University, Baltimore, MD 21218, USA

<sup>3</sup>Center for Space Science and Technology, University of Maryland, Baltimore County, Baltimore, MD 21250, USA

<sup>4</sup>Center for Research and Exploration in Space Science and Technology, NASA Goddard Space Flight Center, Greenbelt, MD 20771, USA

<sup>5</sup>Center for Astrophysics | Harvard & Smithsonian, 60 Garden Street, Cambridge, MA 02138, USA

<sup>6</sup>American Physical Society, Hauppauge, New York, NY 11788, USA

<sup>7</sup>Department of Astronomy, Williams College, Williamstown, MA 01267, USA

<sup>8</sup>Elon University, Elon, NC 27278, USA

<sup>9</sup>Department of Physics, University of Arkansas, Fayetteville, AR 72701, USA

<sup>10</sup>Eureka Scientific, Inc., Oakland, CA 94602-3017, USA

(Received 29 June, 2023; Accepted 3 November, 2023)

### ABSTRACT

We present a methodology for modeling the joint ionizing impact due to a “simple X-ray population” (SXP) and its corresponding simple stellar population (SSP), where “simple” refers to a single age and metallicity population. We construct composite spectral energy distributions (SEDs) including contributions from ultra-luminous X-ray sources (ULXs) and stars, with physically meaningful and consistent consideration of the relative contributions of each component as a function of instantaneous burst age and stellar metallicity. These composite SEDs are used as input for photoionization modeling with *Cloudy*, from which we produce a grid for the time- and metallicity-dependent nebular emission from these composite populations. We make the results from the photoionization simulations publicly available. We find that the addition of the SXP prolongs the high-energy ionizing output from the population, and correspondingly increases the intensity of nebular lines such as He II  $\lambda 1640, 4686$ , [Ne V]  $\lambda 3426, 14.3\mu\text{m}$ , and [O IV]  $25.9\mu\text{m}$  by factors of at least two relative to models without an SXP spectral component. This effect is most pronounced for instantaneous bursts of star formation on timescales  $> 10$  Myr and at low metallicities ( $\sim 0.1 Z_{\odot}$ ), due to the imposed time- and metallicity-dependent behavior of the SXP relative to the SSP. We propose nebular emission line diagnostics accessible with *JWST* suitable for inferring the presence of a composite SXP + SSP, and discuss how the ionization signatures compare to models for sources such as intermediate mass black holes.

### 1. INTRODUCTION

Over the past decade, spectroscopic observations of high redshift ( $z > 6$ ) galaxies and their nearby analogs have revealed the presence of strong high-ionization nebular emission lines (e.g., He II, [Ar IV], [Ne V]) and lines with high equivalent widths, indicating the presence of relatively hard ionizing spectra, recent ( $\lesssim 30$  Myr) star formation, and relatively low metallicities ( $\sim 0.1 Z_{\odot}$ )

(e.g., Garnett et al. 1991; Schaerer 1996; Guseva et al. 2000; Thuan & Izotov 2005; Izotov et al. 2012; Shirazi & Brinchmann 2012; Jaskot & Oey 2013; Stasińska et al. 2015; Stark 2016; Berg et al. 2018, 2019; Senchyna et al. 2017, 2019; Olivier et al. 2022). Attempts to model the observed nebular features of such “extreme emission line galaxies” (EELGs) have revealed that the spectral energy distributions (SEDs) from young, low-metallicity stellar populations have difficulty reproducing the observed strengths of a number of high-ionization emission line species, a problem that has been referred to as

the “high-energy ionizing photon production problem” (Berg et al. 2021).

Addressing this problem is key to understanding how the heating and reionization of the Universe proceeds at  $z > 6$ , a regime now becoming more accessible spectroscopically thanks to *JWST*. In the coming decade, second generation interferometers such as the Hydrogen Epoch of Reionization Array (HERA) will probe even earlier cosmic epochs ( $6 < z < 50$ ) through the cosmic 21-cm signal. This high-redshift 21-cm signal is sensitive to the UV to soft X-ray ( $< 2$  keV) radiation field produced by the first galaxies’ dominant ionizing populations. Initial results from HERA already suggest that the emergent 0.5–2.0 keV X-ray luminosity per galaxy star formation rate ( $L_X$  (0.5–2 keV)/SFR) from galaxies at  $z > 6$  is at least an order of magnitude higher than measured for local galaxies (HERA Collaboration et al. 2023). These results point to increased production efficiency of photons with energies  $\gtrsim 500$  eV from galaxies at high redshift, possibly due to increased formation efficiency of accreting compact objects at the lower metallicities and/or younger stellar population ages characteristic of early galaxies (e.g., Fragos et al. 2013a). Developing a comprehensive accounting of the major sources of high-energy ionizing photons in EELGs, both near and far, therefore requires a framework for modeling how *additional* ionizing sources—such as fast shocks, superbubbles, and X-ray binaries (XRBs)—evolve as a function of redshift-dependent properties such as metallicity and stellar population age (e.g., Allen et al. 2008; Oskina & Schaerer 2022; Simmonds et al. 2021).

One potential alternative source of high-energy ionizing photons is radiative shocks, which may be produced as a consequence of massive star evolution through winds and supernovae explosions (e.g., Izotov et al. 2012, 2021). For fast shocks, there are publicly available grids of emission line ratios for a range of shock properties (Allen et al. 2008). Based on such models, shocks appear capable of sufficient high-energy ionizing photon production to reproduce select observed nebular line intensities for some shock velocities (e.g., Thuan & Izotov 2005); however, it is not yet clear whether fast shocks are capable of simultaneously reproducing suites of high-ionization nebular lines (i.e., from UV to optical), particularly if there is a metallicity-dependence to the observed line ratios (e.g., Senchyna et al. 2017).

Numerous works have also investigated the need for changes to prescriptions used in *stellar* spectral population synthesis and photoionization modeling, such as changes to assumed abundance patterns (e.g., Berg et al. 2021; Grasha et al. 2021), the initial mass function (IMF) and associated products of binary evolution (e.g.,

Götberg et al. 2019; Senchyna et al. 2021), and/or assumptions about stellar rotation and line-driven winds for massive stars at very low metallicities (e.g., Telford et al. 2021). There are publicly available and well-vetted libraries for stellar atmosphere models and isochrones that allow for testing how these different prescriptions affect the ionizing output from stellar populations (see e.g., Conroy 2013, for a review of models). With stellar spectral population synthesis, these ingredients can be flexibly combined for a given IMF to produce the SEDs for simple stellar populations (SSPs)—populations at a single burst age and metallicity—for use in photoionization modeling and spectrophotometric fitting (e.g., Conroy et al. 2009; Conroy & Gunn 2010; Byler et al. 2017; Johnson et al. 2021). These tools enable investigation of how tweaks to stellar population models can address the high-energy ionizing photon production problem (e.g., Berg et al. 2019; Senchyna et al. 2021). However, presently available stellar population models, including those that model some of the products of binary evolution, still have difficulty reproducing the observed intensities of select high-ionization nebular emission lines (e.g., He II; Stanway & Eldridge 2019). This highlights the need for more comprehensive accounting of the products of binary evolution that may contribute to the ionizing photon budget.

Accreting stellar mass compact objects (i.e., XRBs) are one such product of binary evolution, and have long been considered as a potential source of high-energy ionizing photons (e.g., Garnett et al. 1991; Schaerer et al. 2019; Kovlakas et al. 2022). Recent photoionization modeling that combines XRBs with stellar populations hints that XRBs may be sufficient to reproduce observed high-ionization emission line strengths *in some cases* (e.g., Senchyna et al. 2020; Simmonds et al. 2021). However, drawing a cohesive picture of the efficacy of XRBs to addressing the high-energy ionizing photon production problem remains challenging due to the following issues: (1) differing prescriptions for intrinsic XRB SEDs and; (2) minimal consideration towards how to scale XRB power output relative to the stellar population as a function of star formation history (SFH) and metallicity. Critically, for XRBs we currently lack many of the ingredients necessary for truly flexible spectral population synthesis, and therefore a means to understand the XRB contribution to high-energy ionizing photon production. In this work, we take steps to address this via the development of a flexible framework for including XRBs alongside SSPs for use in photoionization modeling.

XRBs, and specifically those sources at the extreme bright-end of the luminosity function known as ultra-luminous X-ray sources (ULXs), are a compelling op-

tion for producing high-energy ionizing photons in high redshift galaxies and their local analogs for a few key reasons. Specifically, such sources (1) form swiftly ( $\gtrsim 3\text{--}5$  Myr) in multiple generations following a burst of star formation (e.g., Linden et al. 2010; Wiktorowicz et al. 2017; West et al. 2023), and are therefore capable of producing ionizing photons on longer timescales than single massive stars; (2) dominate the X-ray power output from normal star-forming galaxies (i.e., those without an actively accreting supermassive black hole) at high specific SFRs (e.g., Lehmer et al. 2016); and (3) have integrated luminosities directly proportional to SFR that increase with decreasing gas-phase metallicity, resulting in increased contribution to the photon budget in low-metallicity, highly star-forming galaxies (e.g., Prestwich et al. 2013; Basu-Zych et al. 2013, 2016; Brorby & Kaaret 2017). For ULXs specifically, there is also increasing evidence for the presence of powerful outflows (e.g., Pinto et al. 2016), which may additionally produce shocks (López et al. 2019; Gúrpide et al. 2022). ULXs may therefore be important sources of both radiative and mechanical feedback at the low metallicities and high specific SFRs characteristic of high redshift galaxies and their local analogs.

A key consideration for modeling the ionizing contribution from accreting stellar mass compact objects such as ULXs is that they should form as a consequence of the evolution of the stellar population. To address this, we present a methodology for constructing a simple X-ray population (SXP), analogous to an SSP (i.e., single age and metallicity), and an approach to a physically consistent coupling of the SXP to the corresponding SSP for use in photoionization modeling. This approach is aimed at providing a more comprehensive framework for investigating the XRB contribution to the high-energy ionizing photon production problem.

This paper is organized as follows: in Section 2 we present the main elements used in constructing the SXP and in Section 3 we outline how the SXP is scaled and added to the corresponding SSP to create the SED for a composite population. In Section 4 we describe our grid-based photoionization modeling set-up using the composite SXP + SSP SEDs. In Section 5 we present key results from the photoionization modeling for the nebular emission from the composite populations, and describe how to access our simulation results. In Section 6 we discuss the SXP model and photoionization simulation results in the context of X-ray detectability, recent literature results for the contribution of X-ray sources to the production of high-ionization emission lines, and alternative ionizing sources. Finally, in Section 7, we summarize our key findings.

## 2. CONSTRUCTING A SIMPLE X-RAY POPULATION

To construct the inputs for the photoionization modeling that follows, we apply the formalism of SSPs to accreting stellar mass compact objects. In what follows, we refer to models for single age and metallicity accreting compact object “populations” as “SXPs.” In constructing these SXPs we consider selection of the following three key ingredients: (1) power output for the population as a function of stellar population age and metallicity; (2) the dominant source type in the population; and (3) physically motivated *intrinsic* source spectra. In this section, we describe the SXP used in this work based on selections for these three ingredients.

### 2.1. Normalization as a Function of Metallicity and Instantaneous Burst Age

Constructing a true SXP requires a prescription for the normalization of X-ray emitting population as a function of burst age and metallicity. To describe this behavior, we use the theoretical predictions for the X-ray power output per stellar mass from XRBs as a function of age and stellar metallicity from the binary population synthesis models presented in Fragos et al. (2013b). We opt to use these theoretical predictions, as opposed to empirical measurements, for two key reasons. First, the evolution of XRB power output—particularly on finely resolved timescales  $\lesssim 100$  Myr that are important for luminous XRB formation—is not yet well-constrained observationally (e.g., Lehmer et al. 2017). In addition, empirical constraints on XRB radiative power as a function of time or metallicity are typically reported in terms of  $L_X/\text{SFR}$ , where the SFR is a quantity averaged over some extended timescale (i.e., 10 or 100 Myr). In this way, available empirical measurements are a time-averaged  $L_X$  for the *observed* XRB population. Such measurements are therefore not ideally suited to simulating the ionizing output from the *intrinsic* XRB population formed from an instantaneous burst of star formation, as we aim to do here.

A critical component of the selected theoretical population synthesis models from Fragos et al. (2013b) is therefore that the predictions are provided in terms of radiative power ( $L_X$ ) from the intrinsic XRB population per initial mass formed in a burst of star formation ( $M_0$ ). Nearly all other theoretical binary population synthesis models currently in the literature that focus on XRBs provide predictions in terms of *number counts* of sources per stellar mass as function of time and metallicity (e.g., Linden et al. 2010; Wiktorowicz et al. 2019). For the purposes of the photoionization modeling that follows,  $L_X/M_0$  is the preferred quantity since trans-

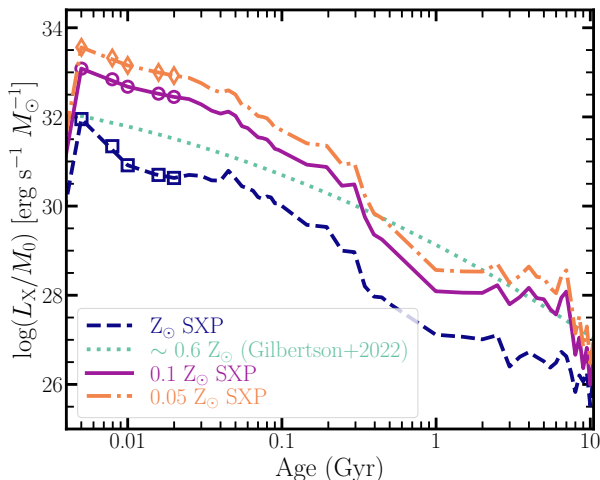


**Figure 1.** The adopted scaling of  $L_X/M_0$  for the SXP as a function of instantaneous burst age and metallicity, where  $M_0$  corresponds to the initial stellar mass ( $Z_\odot$ : dark blue dashed line,  $0.1 Z_\odot$ : purple solid line, and  $0.05 Z_\odot$ : orange dash-dot line) from theoretical binary population synthesis models (Fragos et al. 2013b). The instantaneous burst ages at which we model the SXP contribution in the photoionization simulations are marked with dark blue squares, purple circles, and orange diamonds for the  $Z_\odot$ ,  $0.1 Z_\odot$ , and  $0.05 Z_\odot$  cases, respectively. The SXP component in our models turns on for instantaneous bursts  $\geq 5$  Myr. Empirical results for  $L_X/M_0$  from star-forming galaxy stacks in the *Chandra* Deep Fields, for which the median metallicity ( $\sim 0.6 Z_\odot$ ) is intermediate to the theoretical scalings adopted here, are shown as a green dotted line for reference.

forming number counts to total radiative power is non-trivial, and requires additional assumptions about how the luminosities of different sources should be calculated from theoretical mass supply rates. The models from Fragos et al. (2013b) track the mass supply rate to the compact object population—both black holes (BHs) and neutron stars (NS)—as a function of time. Following prescriptions in Fragos et al. (2008, 2009), the bolometric  $L_X$  is calculated directly for persistent XRBs from the mass supply rate along with the mass and radius of the accretor, assuming different conversion efficiencies for BHs and NS. For transient XRBs, a modified version of this formalism is applied, considering typical duty cycles and outburst luminosities.

The Fragos et al. (2013b) binary population synthesis models used here provide published values of  $L_X/M_0$  for XRBs at three different stellar metallicities<sup>1</sup>:  $Z = 0.002$

( $0.1 Z_\odot$ ),  $Z = 0.02$  ( $Z_\odot$ ), and  $Z = 0.03$  ( $1.5 Z_\odot$ ), and burst ages from 0–10 Gyr. To calculate the normalization of the SXP as a function of age and metallicity, we select a set of seven discrete burst ages and three metallicities from the reference model in Fragos et al. 2013b (i.e., their Figure 2, data provided via private communication).

The seven discrete time steps ( $t_{\text{burst}} \sim \{1, 3, 5, 8, 10, 16, 20\}$  Myr) are selected to maximize  $L_X/M_0$  (i.e., capture a bounding case for XRB ionization), and to cover relevant timescales for important stages of massive star evolution. On these short burst timescales, the XRB population power output is dominated by high-mass XRBs (HMXBs), sources descended from the most massive stars ( $\gtrsim 8 M_\odot$ ). As such, we calculate the normalization of the SXP to reproduce the theoretical  $L_X$  ( $0.5\text{--}8$  keV)/ $M_0$  from the HMXB component of the reference model in Fragos et al. (2013b). We additionally elect to turn on the SXP with a delay time that accounts for the minimum time for the first BHs to form and begin accreting (e.g., Belczynski & Taam 2008; Linden et al. 2010). The first time step in the simulations with SXP contribution is 5 Myr.

Two of the three metallicities selected for our models include those available from the published theoretical population synthesis results, namely  $Z = 0.002$  ( $0.1 Z_\odot$ ) and  $Z = 0.02$  ( $Z_\odot$ ), where the  $0.1 Z_\odot$  scaling for  $L_X/M_0$  is relevant for nearby EELGs and sources at  $z \gtrsim 3$  (e.g., Shirazi & Brinchmann 2012; Madau & Dickinson 2014). We additionally add a third metallicity set at  $0.05 Z_\odot$ , though this metallicity was not originally included in the theoretical population synthesis models. To create normalizations for the SXP for this extremely metal-poor case, we assume the same dependence of  $L_X/M_0$  on post-starburst timescale as the  $0.1 Z_\odot$  model, but allow the absolute normalization of  $L_X/M_0$  to be a factor of  $3\times$  higher than for the  $0.1 Z_\odot$  at each time step. This scaling corresponds roughly to the upper bound on the observed  $\langle L_X/\text{SFR} \rangle$  from galaxies with  $12 + \log(\text{O}/\text{H}) \sim 7.4$  from Lehmer et al. (2021). Though speculative, we include this case for reference, noting that it will likely need to be revised either theoretically or observationally going forward.

In Figure 1, we show the adopted theoretical  $L_X/M_0$  as a function of instantaneous burst age for the three metallicities employed in the photoionization simulations that follow, where the symbols denote burst ages for which the SXP contribution is non-zero and therefore modeled (i.e., we do not display the 1 and 3 Myr time steps in this figure, as we assume there is

<sup>1</sup> Throughout, we assume  $Z = 0.02$  corresponds to  $Z_\odot$  for stellar metallicities. For abundances from Nicholls et al. (2017), this corresponds to a gas-phase metallicity  $12 + \log(\text{O}/\text{H}) = 8.76$ .



no SXP contribution on these timescales.<sup>2</sup> For reference, we also plot in this figure empirical results from Gilbertson et al. (2022) for  $L_X/M_0$  for a sample of star-forming galaxy stacks from *Chandra* Deep Fields. The galaxy stacks from the *Chandra* Deep Fields have median metallicity  $\sim 0.6 Z_\odot$ , intermediate to our selected metallicity range, illustrating that the empirical results are in qualitative agreement with the behavior of the adopted theoretical relations on the timescales of interest for these simulations.

The adopted theoretical values for  $L_X/M_0$  from Figure 1 can be considered as good approximations for the *average* radiative output from a population. For the purposes of our simulations, this is appropriate as we seek to simulate a well-sampled population; however, for observed samples the X-ray luminosity function (XLF) may not be as well-populated. Stochastic sampling of the XLF is particularly important to consider at very low SFRs ( $\lesssim 0.1 M_\odot \text{ yr}^{-1}$ ), where observed values for  $L_X/M_*$  or  $L_X/\text{SFR}$  can be subject to scatter of order  $\sim 1$  dex, especially for sources at the bright end of the XLF (Lehmer et al. 2021). We return to this point in Section 6.1 in discussing how results from these simulations should be compared against observations.

## 2.2. Source Type: Ultra-luminous X-ray Sources

With the adopted scaling for  $L_X/M_0$ , we next consider the source type that dominates the power output from the population. In star-forming galaxies without a central accreting supermassive black hole, XRBs dominate the galaxy-integrated X-ray point source emission. For predominantly young stellar populations ( $\lesssim 100$  Myr) HMXBs are the dominant accretor population, while in galaxies with older stellar populations low-mass XRBs (i.e., sources with low-mass donor stars) dominate the radiative output (e.g., Garofali et al. 2018; Lehmer et al. 2019, 2021).

Regardless of stellar population age, the total radiative power output from a population will be dominated by the sources that populate the bright end of the XLF. Such sources are ULXs, off-nuclear point sources with  $L_X > 10^{39} \text{ erg s}^{-1}$ . These luminosities, under the assumption of isotropic emission, exceed the Eddington limit for a  $10 M_\odot$  BH or  $1.4 M_\odot$  NS:

$$L_{\text{Edd}} = \frac{4\pi GMc}{\kappa_T} = 1.5 \times 10^{38} m \frac{1.7}{1+X} \text{ ergs}^{-1} \quad (1)$$

where  $M$  is the mass of the compact object (such that  $m \equiv M/M_\odot$ ),  $X$  is the hydrogen mass fraction (assumed to be  $X = 0.73$ , corresponding to solar composition),  $G$  is the gravitational constant,  $c$  is the speed of light, and  $\kappa_T = 0.2(1+X)$  is the Thomson scattering opacity.

Models to explain the extreme apparent luminosities from ULXs fall broadly into two categories: (1) isotropic emission from sub-Eddington accretion onto intermediate mass black holes (IMBHs; e.g., Colbert & Mushotzky 1999) or (2) super-Eddington mass transfer via modified accretion disks onto either stellar mass BHs or strongly magnetized NS (e.g., King et al. 2001; Begelman et al. 2006; Poutanen et al. 2007; King 2009). Recent results from X-ray timing studies favor the second scenario, as the detection of pulsations in an increasing number of ULXs indicates the presence of a NS for at least some fraction of the ULX population (e.g., Bachetti et al. 2014; Israel et al. 2017; Brightman et al. 2018). Broadband and high-resolution X-ray spectroscopy of ULXs also support the picture of stellar mass accretors with high mass transfer rates. In particular, the observed spectral turnover for ULXs at energies  $\gtrsim 3\text{--}8$  keV is incompatible with models for intermediate mass or supermassive BHs accreting at sub-Eddington rates (Gladstone et al. 2009a), and the detection of absorption lines for some ULXs provide evidence for the presence of fast outflows (Section 2.3.2; Pinto et al. 2016; Kosec et al. 2018a,b, 2021), and potentially strongly magnetized NS accretors (Walton et al. 2018; Brightman et al. 2022).

These findings suggest ULXs ( $L_X \sim 10^{39} - 10^{42} \text{ erg s}^{-1}$ , i.e., below the hyper-luminous regime) are a distinct class of stellar mass accretors with super-Eddington mass supply rates<sup>3</sup>. This in turn implies that ULXs are indeed the high luminosity extension of the XRB luminosity function. In this work, we treat ULXs as the bright extension of the HMXB luminosity function specifically, as we consider timescales relevant to formation and evolution of the most massive stars ( $\leq 20$  Myr, Section 2.1).

Given that they occupy the bright end of the XLF, ULXs in star-forming galaxies can surpass by

<sup>2</sup> In Section 5.2, we discuss relaxing the assumption that there is a delay-time for SXP formation. In the Appendix we show select line diagnostic results from simulations with no delay-time dependence, where we allow the immediate formation of the SXP alongside the SSP. The results from these no delay-time simulations at 1–3 Myr are similar to the results for the SXP contribution at 5 Myr shown throughout.

<sup>3</sup> As discussed in King et al. (2023), the phrase “super-Eddington accretion” can lead to ambiguity, as stellar mass BHs and NS in ULXs do not actually accrete matter at highly super-Eddington rates; instead, these authors suggest that for ULXs it would be more appropriate to refer to the mass supply or transfer rate as the super-Eddington quantity in question. We adhere to this convention throughout.

at least an order of magnitude the combined output of various HMXB sub-populations filling out the lower luminosity—and more highly populated—portion of the luminosity function (e.g., [Lehmer et al. 2021](#)). *In this work, we therefore choose to model the SXP as a population of ULXs.* Assuming a well-sampled XLF (i.e., high SFR) as we model here, a ULX-based SXP is a reasonable approximation for the total XRB population. Indeed, many highly star-forming galaxies (SFRs  $\geq 3 M_{\odot} \text{ yr}^{-1}$ ) show ULX-like spectra globally ([Garofali et al. 2020](#)). Because various HMXB sub-populations likely have different accretion state distributions and scaling relations with metallicity and stellar population age, approximating the SXP using ULXs considerably simplifies the modeling that follows. Hereafter, we refer to the SXP as “SXP<sub>ULX</sub>”, to indicate the source type modeled. This selection captures a bounding case for HMXB<sup>4</sup> contribution to production of high-energy ionizing photons in terms absolute normalization as emphasized above, as well as hardness of spectral shape (Section 2.3).

### 2.3. Model for Ultra-luminous X-ray Source SED

The efficacy of the SXP<sub>ULX</sub> in the production of high-energy ionizing photons is highly dependent on the shape of the *intrinsic* SED and normalization relative to the corresponding SSP (e.g., [Simmonds et al. 2021](#)). Unfortunately, this intrinsic shape for ULXs is difficult to measure observationally and therefore remains highly uncertain. At the typical extragalactic distances ( $\gtrsim 3$  Mpc) to ULXs, fluxes are  $< 10^{-12} \text{ erg s}^{-1} \text{ cm}^{-2}$ , such that high-resolution X-ray spectroscopy is currently feasible for a limited number ( $\sim 10$ ) of the brightest sources ([Kosec et al. 2018a](#)). At CCD-resolution, many more sources are available for spectral fitting, but these fits are often performed using phenomenological models with no obvious physical basis, which cannot be reliably extrapolated into wavelength regimes outside the observed bandpass. The lack of comprehensive multiwavelength catalogs for ULXs (from IR-to-X-ray) is a further limitation to measuring their intrinsic SEDs, resulting in large uncertainties especially in the extreme ultraviolet (EUV) to very soft X-ray regime ( $\sim 54\text{--}200$  eV). Critically, this is the wavelength regime responsi-

ble for setting the intensity of high-ionization nebular emission lines.

We therefore opt to model our SED (hereafter SED<sub>ULX</sub>) using analytic prescriptions from theoretical models for stellar mass compact objects with super-Eddington mass supply rates. In the sections that follow, we outline the key components of the SED<sub>ULX</sub>, and motivate our selections. The SED<sub>ULX</sub> employed throughout this work is qualitatively similar to empirical models derived from analyses of ULXs detected within their own optical nebulae, where high-ionization emission lines are also detected ([Berghea et al. 2010](#); [Berghea & Dudik 2012](#); [Kaaret & Corbel 2009](#); [Lebouteiller et al. 2017](#); [Simmonds et al. 2021](#)). In such analyses, both the broad-band X-ray data and the observed emission line strengths provide constraints on the form of the ULX SED, where the line emission is particularly useful for constraining the shape of the unseen EUV portion. We note that such a multi-wavelength approach has promise for constraining the shape of the intrinsic SED; however, there is as yet no comprehensive approach in this respect for ULXs given the lack of collated multiwavelength data sets.

#### 2.3.1. Accretor Type

As a starting point to constructing the SED<sub>ULX</sub>, we must select the mass of the accretor as well as the type (BH or NS), as the SED shape will depend not only on accretor mass and mass supply rate, but also on whether the accretion flow encounters a hard surface and/or a strong magnetic field (see Section 6.3.1). Because the selected  $L_X/M_0$  normalizations from Section 2.1 span burst ages  $\leq 20$  Myr, we choose a stellar mass BH ( $< 100 M_{\odot}$ ) as the accretor for the SED<sub>ULX</sub>. Theoretical binary population synthesis models show that the fraction of NS accretors contributing to the observed ULX population is still low on timescales  $< 20$  Myr post-starburst, and that accreting BHs may have ages  $\sim 4\text{--}40$  Myr during their ULX phase ([Middleton & King 2017](#); [Wiktorowicz et al. 2017, 2019](#)).

Given that we likewise elect to model the population at three discrete stellar metallicities ( $Z_{\odot}$ ,  $0.1 Z_{\odot}$ , and  $0.05 Z_{\odot}$ ), we construct the SED<sub>ULX</sub> model as a function of approximate typical BH masses for ULXs at each of these metallicities:  $8 M_{\odot}$  for  $Z \geq 0.1 Z_{\odot}$  and  $16 M_{\odot}$  for  $Z < 0.1 Z_{\odot}$ , following theoretical population synthesis results for ULXs ([Wiktorowicz et al. 2017](#)).

At present it is not clear theoretically or observationally what the typical BH mass is in a ULX as a function of burst age. Thus, we consider it a reasonable simplifying assumption at present to use approximate BH masses as a function of *metallicity only*. It is impor-

<sup>4</sup> There is no explicit ULX population included in the theoretical models from [Fragos et al. \(2013b\)](#), and we therefore use the HMXB component, corresponding to the bright end of the XLF, for normalizing the SXP; however, the theoretical models do allow for XRBs undergoing outbursts to exceed Eddington. We also note that empirical values for  $L_X/M_0$  from galaxy-integrated studies, where the populations can be assumed to be dominated by sources at the brightest end of the XLF, i.e., ULXs, appear relatively consistent with the theoretical scaling relations ostensibly for HMXBs employed here, as shown in Figure 1.

tant to note that while these selected BH masses factor into the parametrization of the  $\text{SED}_{\text{ULX}}$  shape (Section 2.3.3), they do not strongly affect the *normalization* of the  $\text{SED}_{\text{ULX}}$ , which is instead set by the theoretical scaling relations from Section 2.1, which are also key to setting the simulated nebular line intensities.

### 2.3.2. Accretion Flow Geometry & Components

Under the selection of a stellar mass accretor with super-Eddington mass supply rate for the  $\text{SED}_{\text{ULX}}$ , theory and observation alike suggest the presence of a strong outflow, which is a key component in defining the SED shape. In the supercritical regime the accretion flow consists of distinct zones delineated by the wind/outflow component (e.g., Shakura & Sunyaev 1973; Lipunova 1999; Poutanen et al. 2007; Abolmasov et al. 2009). We illustrate these zones in Figure 2, as follows:

- The hot inner region of the accretion flow before the wind launching zone ( $R < R_{\text{ph, in}}$ ).
- The region between the wind launching zone and so-called the spherization radius ( $R_{\text{ph, in}} < R < R_{\text{sph}}$ ), where the wind is optically thick. The spherization radius ( $R_{\text{sph}}$ ) can be thought of as the region where the disk is unstable and super-Eddington (i.e., the actual accretion rate is Eddington within this radius, and limited through the expulsion of matter from the disk as a wind).
- The region beyond the spherization radius where the wind becomes optically thin ( $R > R_{\text{sph}}$ ). The outer extent of the wind is given by the effective photospheric radius of the outflow,  $R_{\text{ph, out}}$ .

Under such a model, the launching of the disk wind leads to an evacuated “wind funnel,” wherein the hard inner disk emission is geometrically collimated and scattered by the wind. At much larger disk radii ( $R > R_{\text{sph}}$ ), the wind becomes optically thin and can be approximated as a pseudo-photosphere (i.e., a quasi-spherical component with a blackbody spectrum). This picture of the accretion flow is broadly consistent with CCD-resolution spectra of ULXs, which typically require multi-component models to fit their observed spectra (e.g., Gladstone et al. 2009b; Sutton et al. 2013; Middleton et al. 2015).

In defining our  $\text{SED}_{\text{ULX}}$  model, we therefore include a component representing the hot inner disk and wind funnel, as well as a component for the outflow. In addition, we consider the effects of Compton scattering and irradiation on the resultant SED shape. Irradiation—where

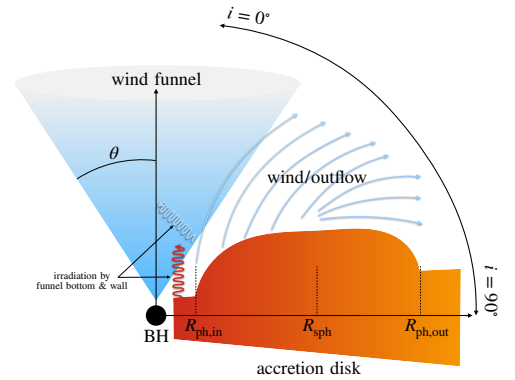


**Figure 2.** Cartoon depiction of the accretion flow geometry for the  $\text{SED}_{\text{ULX}}$  model. Key components and parameters are labeled, including the accretor (BH) and accretion disk, evacuated wind funnel and associated funnel opening angle ( $\theta$ ), the inner and outer photospheric radii ( $R_{\text{ph, in}}$ ,  $R_{\text{ph, out}}$ , respectively), the spherization radius ( $R_{\text{sph}}$ ), and the inclination angle ( $i$ ) with respect to an observer. The wind or outflow, which is launched from the accretion disk and assumed to be a quasi-spherical component, is shown by the blue arrows. Irradiating photons emanate from the hot inner accretion flow and funnel walls, as labeled.

one component of the accretion flow absorbs and re-emits radiation from another component—may be critically important in the context of  $\text{SXP}_{\text{ULX}}$  contribution to high-energy ionizing photon production. This is because reprocessed emission due to irradiation can produce a spectrum with a more substantial EUV component, where photon energies exceed ionization potentials for lines such as He II  $\lambda 4686$  and [Ne V]  $\lambda 3426$ . Given the geometry of the supercritical accretion flow described above, it is unlikely that there is direct irradiation of the outer regions of the accretion disk by hot inner disk photons (e.g., Gierliński et al. 2009). In the case of a ULX with an outflow, the wind likely blocks and reprocesses the hot inner disk emission. Irradiation may therefore occur via the wind irradiating the outer disk (Vinokurov et al. 2013; Yao & Feng 2019), or via “self-irradiation” of inner disk and funnel wall emission within the wind funnel itself (Abolmasov et al. 2009).

For the  $\text{SED}_{\text{ULX}}$  in this work, we choose to model the irradiated component as being due to self-irradiation within the wind funnel. This is because there are uncertainties in how effectively soft photons from the wind thermalize in the outer disk (Kaaret & Corbel 2009; Grisé et al. 2012a), and additional complexities in handling the geometry and radiative transfer for wind irradiation. To represent the supercritical accretion flow with self-irradiation, we opt to use the `sirf`, or “self-irradiated funnel”, template as implemented in `XSPEC` (Abolmasov et al. 2009). This particular template pro-

**Table 1.** Summary of calculated and selected parameters for the SED<sub>ULX</sub> model, as implemented via the `simpl(sirf)` templates in XSPEC. Parameter names follow nomenclature used in XSPEC, as described in the text.

Component	Name	Value	Units
(1)	(2)	(3)	(4)
<b>sirf</b>	$T_{\text{funnel, in}}$	Eq. 11	keV
	$r_{\text{ph, in}}$	Eq. 10	$R_{\text{sph}}$
	$r_{\text{ph, out}}$	Eq. 12	$R_{\text{sph}}$
	$\theta$	Eqs. 7–8	deg
	$i$	0	deg
	$\alpha$	0	...
	$\gamma$	4/3	...
	$\dot{m}$	Eq. 9	...
	irrad.	4	...
norm.	Fragos et al. (2013b)	...	
<b>simpl</b>	$\Gamma$	2.5	...
	Frac. Sctr	0.1	...
	Up Sctr. Only	0	...

vides a physical model coupling all components of the supercritical accretion flow, including the hot inner disk, outflow, and the effects of irradiation consistent with the previously described flow geometry. To additionally account for the effects of Compton scattering, we include the `simpl` (SIMple Power Law) convolution component, which Comptonizes flux output from the `sirf` model. Thus, our SED<sub>ULX</sub> is implemented as `simpl(sirf)` in XSPEC, with relevant parameters listed in Table 1. Under this accretion flow model, the mass supply rate relative to Eddington sets the physical parameters (i.e., characteristic radii and temperatures) that define the shape of the *intrinsic* spectrum, while the viewing angle ( $i$  in Figure 2) determines the shape of the *observed* spectrum. In this respect, the `sirf` template is ideal, as it allows for changing the inclination angle to simulate changes to the apparent emergent spectrum for an observer, a point we return to in more detail in Section 6.1.

### 2.3.3. Parametrization of SED Shape

We aim to construct the SED<sub>ULX</sub> model with as few *selected* parameter values as possible. Therefore, to the extent possible, we calculate parameter values for the `sirf` template analytically from a few key selected physical properties (see Shakura & Sunyaev 1973; Poutanen et al. 2007; Abolmasov et al. 2009, for prescriptions).

The primary selected properties influencing the SED<sub>ULX</sub> shape are the accretor mass and the shape of XLF, both of which are assumed to depend on metallicity. For the former, our model selections are described in Section 2.3.1. For the latter, we employ a model for the metallicity-dependent XLF. Below we describe the form of the XLF model, and outline how the physical properties (i.e., Table 1) defining the shape of the SED<sub>ULX</sub> are determined analytically from this model.

The XLF describes the number count of sources in bins of luminosity that contribute to the SXP<sub>ULX</sub>. To calculate this distribution of sources as a function of metallicity, we employ the empirical metallicity-dependent XLF from Lehmer et al. (2021):

$$\frac{dN_{\text{HMXB}}}{dL} = \text{SFR } A_{\text{HMXB}} \exp[-L/L_c(Z)] \times \begin{cases} L^{\gamma_1} & (L < L_b) \\ L_b^{\gamma_2(Z)-\gamma_1} L^{-\gamma_2(Z)} & (L > L_b) \end{cases} \quad (2)$$

In this model,  $\gamma_2(Z)$  is a metallicity-dependent bright-end slope (see Equation 2 from Lehmer et al. 2021), and  $\log L_c(Z)$  is a metallicity-dependent exponential cutoff luminosity (see Equation 3 from Lehmer et al. 2021). For the remaining model parameters that do not depend on metallicity ( $A_{\text{HMXB}}$ ,  $\gamma_1$ , and  $L_b$ ), we use the best-fit values from Table 2 in Lehmer et al. (2021).

The best-fit form of this XLF model is derived from a sample of 55 local ( $< 30$  Mpc) star-forming galaxies spanning gas-phase metallicities  $7.0 \leq 12 + \log(\text{O}/\text{H}) \leq 9.2$ . To populate the SXP<sub>ULX</sub> using this model, we restrict ourselves to sampling bins of luminosity between  $10^{39} \leq L_X \leq 10^{41}$  erg s<sup>-1</sup>. The lower limit corresponds roughly to the Eddington limit for stellar mass accreting compact objects, and the upper limit corresponds to the potential upper limit on  $L_X$  for accreting stellar mass compact objects, i.e., below the regime of hyperluminous sources (Tranin et al. 2023).

Because Equation 2 is an empirical model, sampling from this XLF results in *observed* ULX number counts in bins of *observed* luminosity ( $L_{\text{obs}}$ ). By contrast, the shape of the accretion flow model from Section 2.3.2 is set by *intrinsic* physical properties, which are often difficult to measure directly for a given ULX or a population of sources. As such, we must transform the observed XLF quantities (number counts, or relative contribution to the total population, and  $L_{\text{obs}}$ ) into the intrinsic physical properties from Table 1. To do so, we follow a methodology similar to the approach outlined in Kovelakas et al. (2022).

Taking this approach ( $L_{\text{obs}} \rightarrow$  intrinsic physical parameters) requires defining the intrinsic physical prop-



erties of interest. To begin with, the mass transfer rate is a parameter critical to defining the spectral shape. By definition, a source in an ultra-luminous accretion state will have a mass supply rate exceeding the Eddington rate:

$$\dot{M}_{\text{Edd}} = \frac{48\pi GM}{c\kappa_T} \simeq 3 \times 10^{-8} m M_{\odot} \text{ yr}^{-1} \quad (3)$$

where  $m$  is the mass of the accretor in units of  $M_{\odot}$ . It is often convenient to define a dimensionless mass transfer rate  $\dot{m}$ , as follows:

$$\dot{m} = \dot{M}/\dot{M}_{\text{Edd}} \quad (4)$$

A source in the ultra-luminous state would therefore be expected to have  $\dot{m} \gg 1$ . The *intrinsic* luminosity then depends logarithmically on the dimensionless mass transfer rate (Poutanen et al. 2007):

$$L_{\text{bol}}^{\text{int}} = L_{\text{Edd}}(1 + 0.6\ln(\dot{m})) \quad (5)$$

Following King (2009), the *observed*, or apparent, luminosity may differ from the intrinsic luminosity due to geometrical beaming, given by beaming factor  $b$ , such that:

$$L_{\text{obs}} = L_{\text{bol}}^{\text{int}}/b \quad (6)$$

The combination of Equations 5–6 connects the XLF-derived property  $L_{\text{obs}}$  with the intrinsic properties  $b$ ,  $\dot{m}$ , and  $L_{\text{Edd}}$ , where the Eddington limit is given by Equation 1 for the assumed BH mass  $m$ . The number of free intrinsic parameters can be further reduced given a reasonable assumption about the physical meaning of the beaming factor  $b$ . Under the formalism outlined in King (2009), the beaming factor  $b$  is related to the funnel opening angle ( $\theta$ , as shown in Figure 2) by  $b = \Omega/4\pi$ , where  $\Omega = 2 \times 2\pi(1 - \cos\theta)$  is the combined solid angle from both cones of the wind funnel. In this way, the beaming factor ( $b$ ) also sets the probability that the source is observed:

$$b = P_{\text{obs}}(\theta) = 1 - \cos\theta \quad (7)$$

For large funnel opening angles ( $\theta \sim 90^\circ$ ), the beaming factor approaches unity, and there is a high probability the source is observed. For very small opening angles, by contrast, the beaming factor is small and the observed luminosity of the central disk is boosted, but the probability that the source is observed at X-ray wavelengths is low. King (2009) suggest that the beaming factor itself may depend on the mass transfer rate, and

we adopt this view for our model to reduce the number of predetermined parameter values. Specifically, we parameterize  $b$  in terms of the mass transfer rate as follows:

$$b = \begin{cases} 1 & \dot{m} \leq 8.5 \\ (8.5/\dot{m})^2 & \dot{m} > 8.5 \end{cases} \quad (8)$$

By this definition, high mass transfer rates lead to small funnel opening angles, correspondingly small beaming factors, and therefore low probabilities for observing hard emission from the source.

Further combining Equation 8 with Equations 5–6 enables solving for  $\dot{m}$  in terms of  $L_{\text{obs}}$  and  $L_{\text{Edd}}$ . In particular, this can be accomplished via an analytic approximation as outlined in Kovelakas et al. (2022):

$$\dot{m} = \begin{cases} L_{\text{obs}}/L_{\text{Edd}} & L_{\text{obs}}/L_{\text{Edd}} \leq 1 \\ e^{(L_{\text{obs}}/L_{\text{Edd}}-1)} & 1 < L_{\text{obs}}/L_{\text{Edd}} \leq 3.14 \\ 8.5 \times \left(\frac{L_{\text{obs}}/L_{\text{Edd}}}{3.14}\right)^{4/9} & L_{\text{obs}}/L_{\text{Edd}} > 3.14 \end{cases} \quad (9)$$

We note that  $L_{\text{obs}}$  is determined from the metallicity-dependent XLF, and  $L_{\text{Edd}}$  is determined by the accretor mass. Therefore, given *only* selections for the form of the XLF and the typical BH mass as a function of metallicity, we can analytically calculate  $\dot{m}$ ,  $b$ , and  $\theta$  using Equations 7–9.

With  $\theta$ ,  $\dot{m}$ , and  $b$  specified as above, and with the selection for  $m$  from Section 2.3.1, it is relatively straightforward to calculate a number of the remaining critical parameters setting the shape of the `sirf` component of the model (see Table 1). The spherization radius where the outflow is launched is calculated as  $R_{\text{sph}} = \frac{18}{\cos\theta} R_{\text{S}} \dot{m}$ , where  $R_{\text{S}} = 2\frac{GM}{c^2}$  is the Schwarzschild radius<sup>5</sup>. The minimum inner radius for the photosphere ( $r_{\text{ph,in}}$ ) in units of this spherization radius ( $R_{\text{sph}}$ ) can be calculated as as the innermost stable circular orbit ( $R_{\text{isco}} = 6\frac{GM}{c^2}$ ) divided by  $\theta$ :

$$r_{\text{ph,in}} = \frac{1}{6\dot{m}} \quad (10)$$

The corresponding temperature at the inner edge of the wind funnel ( $T_{\text{funnel, in}}$ ), and the outer radius of the photosphere ( $r_{\text{ph,out}}$ ), also in units of the spherization radius, can be calculated analytically following Abolmasov et al. (2009):

<sup>5</sup> This is proportional to the dimensionless spherization radius from Poutanen et al. (2007), given as  $r_{\text{sph}} = 5/3 \times \dot{m}$ , but critically also depends on the geometry of the funnel.

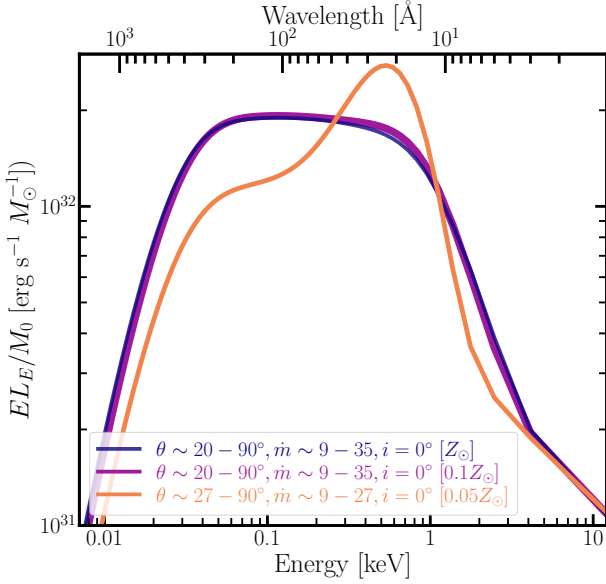


**Figure 3.** The intrinsic broad-band  $\text{SED}_{\text{ULX}}$  for the  $\text{SXP}_{\text{ULX}}$  (i.e., `simpl(sirf)` in `XSPEC`) for each of the three metallicities simulated in this work ( $Z_{\odot}$ : dark blue,  $0.1 Z_{\odot}$ : purple, and  $0.05 Z_{\odot}$ : orange). All SEDs are normalized to the same bolometric luminosity for plotting purposes. The shape of the intrinsic SED is set by the distribution of funnel opening angles ( $\theta$ ) and mass transfer rates ( $\dot{m}$ ) for the accreting population, where the distribution depends on metallicity. For all simulations in this work, we assume  $i = 0^{\circ}$ .

$$T_{\text{funnel, in}} = 0.038(\Omega' \tan^2 \theta r_{\text{ph, in}})^{-1/4} \times (2.8 + 0.6 \ln \dot{m}_3)^{1/4} \dot{m}_3^{-1/2} M_{10}^{1/4} \text{ keV} \quad (11)$$

$$r_{\text{ph, out}} \simeq \left[ \frac{2\Omega' \sqrt{\dot{m}}}{(1 + \alpha) \sqrt{\cos \theta}} \right]^{1/(1 + \alpha)} \quad (12)$$

where  $\dot{m}_3 = \dot{M}$  in units of  $10^3 \dot{M}_{\text{Edd}}$ ,  $\Omega' = -8\pi \ln \sin \theta$ ,  $M_{10}$  is the mass of the BH in units of  $10 M_{\odot}$ , and  $\alpha$  is the exponent describing the velocity law for the wind. Our Equation 11 corresponds to Equation 35 from [Abolmasov et al. \(2009\)](#), where we have assumed  $T_{\text{funnel, in}}$  is equal to the temperature at the bottom of the funnel ( $T_{\text{bot}}$ ) for the `sirf` template.

The remainder of the parameters for the `sirf` component of the model are selected, as summarized in Table 1, where notation corresponds to symbols used in `XSPEC`. In particular, the model has  $i = 0^{\circ}$  (such that the cloud in the photoionization modeling described in Section 4 sees all components of the inflow/outflow),  $\alpha = 0$  (no acceleration for the wind),  $\gamma = 4/3$  (default value, the adiabatic index for the inner parts of the accretion flow), and `irrad. = 4` (number of iterations for irradiation).

Finally, we convolve the `sirf` component with a Comptonization component (`simpl`) in order to reproduce the typical high-energy ( $> 2$  keV) shape of observed ULX spectra. All parameters values of the `simpl` component are selected, namely the photon power-law index  $\Gamma = 2.5$ , and the scattering fraction (10%). For observed ULXs fit with the `simpl` convolution component, the recovered Comptonization parameters are broadly consistent with those listed in Table 1; however, such parameters are typically not tightly constrained from observations (e.g. [Walton et al. 2013, 2014](#)). As such, we consider the  $\text{SED}_{\text{ULX}}$  shape at energies  $\gtrsim 2$  keV, which is set by the `simpl` component, critical for comparisons to apparent observed  $L_{\text{X}}$ , but not particularly physically informative in terms of shape.

The procedure for parametrizing the SED shape is performed on a *per luminosity bin* basis. The XLF from Equation 2 provides the characteristic  $L_{\text{obs}}$ , and therefore corresponding  $\dot{m}$ ,  $b$ , and  $\theta$ , for each bin, as well as the number of sources in each luminosity bin (i.e., relative contribution to the total). The  $\text{SED}_{\text{ULX}}$  for the total population is then the weighted sum of the SEDs from each luminosity bin. In this way, the resultant population-integrated  $\text{SED}_{\text{ULX}}$  represents sources with a range of mass transfer rates, and beaming factors/funnel opening angles. In Figure 3 we show the population-integrated  $\text{SED}_{\text{ULX}}$  for each of the three metallicities used in this work.

As is evident from Figure 3, the procedure outlined above results in a metallicity-dependent shape for the  $\text{SED}_{\text{ULX}}$ . In particular, for  $Z \gtrsim 0.1 Z_{\odot}$ , sources with the largest funnel opening angles ( $\theta \sim 90^{\circ}$ ) contribute  $\sim 35$ – $45\%$  of the total luminosity (going from  $Z_{\odot}$  to  $0.1 Z_{\odot}$ , respectively), while for  $Z \lesssim 0.05 Z_{\odot}$  sources with  $\theta \sim 90^{\circ}$  contribute 99% of the total population-integrated luminosity. This change in the fractional contribution of sources with different characteristic funnel opening angles/mass transfer rates is a consequence of the change to the shape of the XLF as a function of metallicity *and* the change to the typical BH (accretor) mass with metallicity. The former alters the number distribution of sources with luminosity, as the bright-end slope of the XLF becomes increasingly more flat with decreasing metallicity. The latter affects the Eddington limit (Equation 1), and therefore the threshold for a source with a given  $L_{\text{obs}}$  being mildly versus highly super-Eddington. For the typical accretor mass of  $8 M_{\odot}$  for the  $Z \geq 0.1 Z_{\odot}$  models, the Eddington limit is  $\sim 1.2 \times 10^{39} \text{ erg s}^{-1}$ . Taking this limit in conjunction with Equations 7–9, only sources with  $L_{\text{X}} \gtrsim 3.8 \times 10^{39} \text{ erg s}^{-1}$  will have  $\theta < 90^{\circ}$ . By contrast, for the typical BH mass of  $16 M_{\odot}$  for the  $Z \leq 0.05 Z_{\odot}$  models,

the Eddington limit increases to  $\sim 2.4 \times 10^{39}$  erg  $s^{-1}$ , implying that only sources with  $L_X \gtrsim 7.5 \times 10^{39}$  erg  $s^{-1}$  will have  $\theta < 90^\circ$ . Sources at these very high luminosities are quite rare at all metallicities for the adopted XLF model.

As a consequence of these model selections, highly super-Eddington sources—those with smaller funnel opening angles and therefore stronger EUV-emitting quasi-spherical outflow components—appear less frequently in the lowest metallicity model relative to the higher metallicity models. The  $SED_{ULX}$  models for  $Z \geq 0.1 Z_\odot$  are therefore flatter through the EUV than the  $SED_{ULX}$  model at  $0.05 Z_\odot$ . As a final note, we reiterate that this procedure sets only the metallicity-dependent shape of the  $SED_{ULX}$ . The overall normalization for the model is calculated following the theoretical scaling of  $L_X/M_0$  with starburst age and metallicity from Fragos et al. (2013b) as described in Section 2.1.

We make the  $SED_{ULX}$  models at each metallicity available as part of this work (Section 5.4), noting they represent *only* the accretion flow, and therefore do not account for any emission related to the putative donor star. We have implemented the  $SED_{ULX}$  without selecting a unique donor star in part because the distribution of such sources for ULXs, though the subject of intense study, is still not well-constrained theoretically or observationally (e.g., Liu et al. 2004; Copperwheat et al. 2005; Tao et al. 2011; Motch et al. 2011; Soria et al. 2012; Grisé et al. 2012b; Gladstone et al. 2013; Heida et al. 2014, 2016, 2019a,b; Lau et al. 2019; Wiktorowicz et al. 2017, 2021). Identifying unique optical, UV, or IR counterparts at the extragalactic distances to most ULXs remains challenging. Constraining donor stars SEDs through photometry or spectroscopy is likewise difficult given uncertainties such as the contribution of emission from the accretion flow itself, and effects of irradiation of the donor star. In the photoionization simulations that follow, the  $SED_{ULX}$  is always coupled to the SED for a stellar population, thereby making a range of potential donor stars available to the accretor population. We consider this a sensible choice for modeling the spectra or nebular emission from simple *populations*; however, comparison of this model to broad-band observations for an *individual* ULX would warrant matching the  $SED_{ULX}$  with the spectrum for an appropriate donor star, and therefore further customization of the  $SED_{ULX}$  model presented here.

### 3. CONSTRUCTING A PHYSICALLY CONSISTENT COMPOSITE POPULATION

In constructing a composite population with contributions from both stars and ULXs, we start from the

assumption that the  $SXP_{ULX}$  can be specified using the same parameters governing the evolution of the stellar population. Ideally, the  $SXP_{ULX}$  contribution would be determined directly from stellar population synthesis models themselves; however, there is currently no publicly available set of models for which properties of both the stellar and accreting compact object population are easily recoverable. Absent such models, our method aims to stitch together the  $SXP_{ULX}$  model with publicly available models for SSPs in a physically consistent way.

To specify the stellar component (i.e., SSPs) of the composite population, we opt to use Flexible Stellar Population Synthesis (FSPS) and the associated Python-FSPS bindings (Conroy et al. 2009; Conroy & Gunn 2010; Johnson et al. 2023). For the SSPs, we use the Binary Population and Spectral Synthesis (BPASSv2.2; Eldridge et al. 2017) models available in FSPS, which set the prescriptions for the IMF, as well as metallicity- and time-dependent properties of the spectra for the stellar population. We use the spectra from BPASS v2.2 that include products of binary evolution, noting that this version does not explicitly include accreting compact objects as part of the population. As a consequence of using the default BPASS SSPs included in FSPS, the IMF has an upper mass cutoff of  $100 M_\odot$ , a low-mass ( $0.1\text{--}0.5 M_\odot$ ) IMF slope of  $-1.30$ , and a high-mass ( $0.5\text{--}100 M_\odot$ ) IMF slope of  $-2.35$  (matching the IMF used in the theoretical models from Fragos et al. 2013b). For the BPASS models  $Z = 0.02$  corresponds to  $Z_\odot$ . By convention in FSPS, each SSP is normalized by stellar mass.

We construct a grid of BPASS SSPs in age and metallicity corresponding to the selected burst ages and metallicities at which we model the  $SXP_{ULX}$  ( $t_{\text{burst}} \sim \{1, 3, 5, 8, 10, 16, 20\}$  Myr, and  $Z = \{0.001, 0.002, 0.02\}$ ). Because the  $SXP_{ULX}(t_{\text{burst}}, Z)$  models we produce are already in terms of  $1 M_\odot$  stellar mass, we simply add them to the corresponding SSP to produce the composite  $[SXP_{ULX} + SSP](t_{\text{burst}}, Z)$ . This ensures some measure of physical consistency between the SSP and SXP, for example, accounting for the delay between formation of high mass stars and the appearance of the first X-ray emitting accreting BHs. This procedure also incorporates metallicity dependent effects on the SSP and SXP evolution. For example, the increase in radiative output from the  $SXP_{ULX}$  with decreasing metallicity shown in Figure 1 is likely the consequence of weaker line-driven winds for massive stars at low metallicities, which result in less mass and angular momentum loss from the binary. This in turn results in XRBs with more massive compact objects and tighter orbits, which facilitate

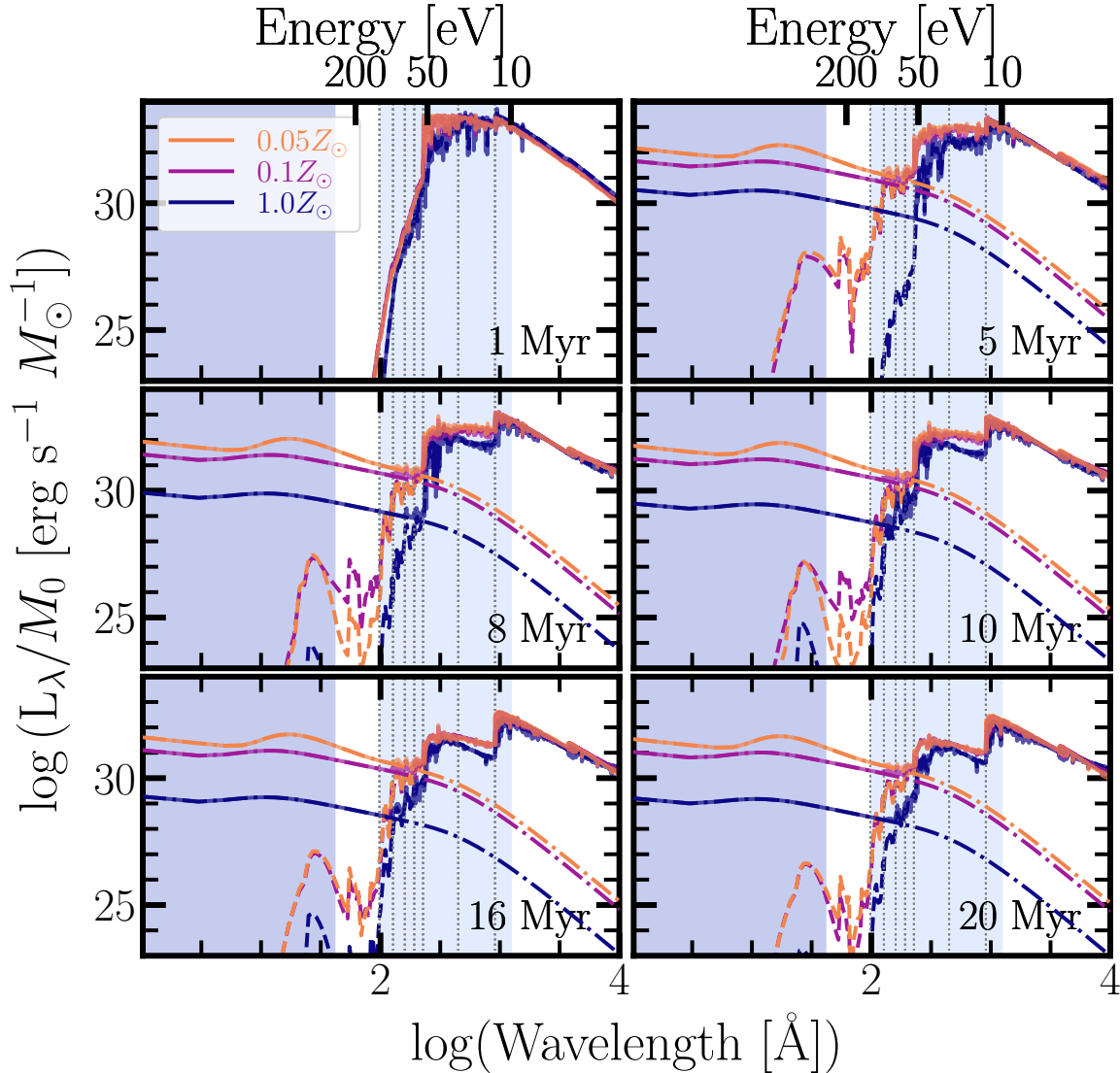


**Figure 4.** The composite  $\text{SXP}_{\text{ULX}} + \text{SSP}$  SEDs (solid lines) for the sampled metallicities (dark blue:  $Z_{\odot}$ , purple:  $0.1 Z_{\odot}$ , and orange:  $0.05 Z_{\odot}$ ) normalized to the initial stellar mass (in this case  $1 M_{\odot}$  formed in an instantaneous burst), where the burst age is annotated in each panel. In each panel, the dash-dot line shows the  $\text{SXP}_{\text{ULX}}$  component of the composite, while the dashed line denotes the SSP contribution. The dark blue shaded region indicates the 0.5–12 keV range, while the light blue shaded region shows the EUV regime. Grey dotted vertical lines mark the ionization potentials for select lines, from high to low energies (left to right): [Ne V], [Ne IV], [O IV], C IV, He II, [Ar II], and H. The addition of the  $\text{SXP}_{\text{ULX}}$  to the corresponding SSP substantially adds to the intensity at energies  $\gtrsim 54$  eV ( $\log(\text{Wavelength } \text{\AA}) = 2.36$ ), particularly for the low-metallicity models with  $t_{\text{burst}} > 10$  Myr.

more efficient mass transfer, thereby producing more luminous sources (Linden et al. 2010; Mapelli et al. 2010). Pairing a low metallicity  $\text{SXP}_{\text{ULX}}$  (high  $L_{\text{X}}/M_0$ ) with a high metallicity SSP would therefore be inconsistent, i.e., would assume that massive stars with strong line-driven winds typically produce XRBs with tight orbits and massive accreting compact objects.

In Figure 4 we show the  $[\text{SXP}_{\text{ULX}} + \text{SSP}](t_{\text{burst}}, Z)$  models normalized to  $1 M_{\odot}$  of initial stellar mass (solid lines), where each panel corresponds to the annotated

instantaneous burst age. The  $\text{SXP}_{\text{ULX}}$  and SSP components are shown as dash-dot and dashed lines, respectively. We do not display the 3 Myr burst, as it is very similar to the 1 Myr panel, prior to  $\text{SXP}_{\text{ULX}}$  formation. In all panels, the 0.5–12 keV bandpass is highlighted via the dark blue shaded region, while the EUV range is shown in light blue. These  $[\text{SXP}_{\text{ULX}} + \text{SSP}](t_{\text{burst}}, Z)$  models, which span wavelengths  $1\text{--}10^8 \text{\AA}$ , are used as the spectral input for photoionization modeling with Cloudy.



#### 4. PHOTOIONIZATION SIMULATIONS WITH Cloudy

We perform photoionization simulations using the [SXP<sub>ULX</sub> + SSP]( $t_{\text{burst}}$ ,  $Z$ ) models as input to Cloudy v17.02 (Ferland et al. 2017). To construct the Cloudy-specific input files for our photoionization simulation grid and organize the Cloudy output, we employ a modified version of the CloudyFSPS code (Byler 2018). Below we describe the Cloudy simulation set-up, relevant grid parameters, and saved output from the simulations.

For the cloud geometry in all simulations, we assume a closed spherical shell with a fixed inner radius  $R = 10^{19}$  cm and a constant density  $n_{\text{H}} = 100 \text{ cm}^{-3}$ . The cloud is ionized by a central source, which we set as the [SXP<sub>ULX</sub> + SSP]( $t_{\text{burst}}$ ,  $Z$ ) SED, implying coincident mixing between the SXP<sub>ULX</sub> and SSP components. This cloud set-up is most appropriate for radiation-bounded regions, while the assumed density is appropriate to HII regions. The chosen value for the inner radius ( $R$ ) corresponds to  $\sim 0.3\text{--}3 R_{\text{S}}$  over the entire simulation grid, where  $R_{\text{S}}$  is the Strömgen<sup>6</sup> radius.

We set  $i = 0$  for the SED<sub>ULX</sub> component of the [SXP<sub>ULX</sub> + SSP]( $t_{\text{burst}}$ ,  $Z$ ), which is equivalent to assuming an isotropic distribution of photons from the composite spectrum is incident on the cloud. This is a simplifying assumption, but reasonable for the production of high-energy ionizing photons as considered here. The outflow component of the SED<sub>ULX</sub> is quasi-spherical, and it is this component in particular that emits strongly in the EUV. We consider more complex geometrical effects beyond the scope of the present work, but note that although the cloud in all simulations is subject to an isotropic distribution of photons (effective  $i = 0$ ), simulation results can be post-processed with  $i > 0$  to simulate different viewing angles for an observer.

In setting the chemical composition of the cloud, we follow the prescriptions outlined in Richardson et al. 2022. In brief, we employ reference abundances and scaling factors with metallicity for these abundances from Nicholls et al. (2017). We include both Orion grains and polycyclic aromatic hydrocarbons (PAHs) in the cloud (Baldwin et al. 1991; Abel et al. 2008). We adopt

<sup>6</sup>  $R_{\text{S}} = (\frac{3Q_{\text{H}}}{4\pi\alpha(T_{\text{e}})n_{\text{e}}n_{\text{H}}})^{1/3}$ , where  $Q_{\text{H}}$  is the hydrogen ionizing photon rate,  $\alpha(T_{\text{e}})$  is the recombination rate,  $n_{\text{e}}$  is the electron density, and  $n_{\text{H}}$  is the hydrogen density. To obtain the range of  $R_{\text{S}}$  from our simulations, we calculate  $Q_{\text{H}}$  directly from the input SEDs, use  $\alpha(T_{\text{e}}) = 2.6 \times 10^{-13} \text{ cm}^3 \text{ s}^{-1}$  (corresponding to  $T_{\text{e}} = 10^4$  K, as in Jaskot & Ravindranath 2016), and assume  $n_{\text{e}} = n_{\text{H}} = 100 \text{ cm}^{-3}$ .

a metallicity-dependent prescription for the gas-to-dust ratio, such that the abundances of all grains are scaled from their default values to satisfy a broken power-law form for the gas-to-dust ratio (Equation 5 in Richardson et al. 2022). Finally, we include depletion on to dust grains using a custom set of depletion factors (Table 1 Richardson et al. 2022).

The [SXP<sub>ULX</sub> + SSP]( $t_{\text{burst}}$ ,  $Z$ ) models specify the SED of the central ionizing source normalized by initial stellar mass. In order to set the intensity of the composite population for the Cloudy simulations, we normalize each model by the dimensionless ionization parameter  $\mathcal{U}$ :

$$\mathcal{U} \equiv \frac{Q_{\text{H}}}{4\pi R^2 n_{\text{H}} c} \quad (13)$$

where  $Q_{\text{H}} \equiv \int_{\nu_0}^{\infty} \frac{f_{\nu}}{h\nu} d\nu$  is the rate of emitted photons capable of ionizing hydrogen (i.e.,  $h\nu_0 = 13.6$  eV),  $R$  is the inner cloud radius (hydrogen ionized region) in cm,  $n_{\text{H}}$  is the hydrogen number density in  $\text{cm}^{-3}$ , and  $c$  is the speed of light. By this definition, the dimensionless ionization parameter can be thought of as the density of photons relative to the density of atoms. For the simulations presented here we select seven values of  $\log \mathcal{U} = [-4.0, -3.5, -3.0, -2.5, -2.0, -1.5, -1.0]$ , a range that is typical for modeling HII regions or starbursts (e.g., Dopita et al. 2000; Kewley et al. 2013). Each model is therefore specified as [SXP<sub>ULX</sub> + SSP]( $t_{\text{burst}}$ ,  $Z$ ,  $\log \mathcal{U}$ ) before being run through Cloudy.

Because  $R$  and  $n_{\text{H}}$  remain fixed<sup>7</sup> in our models, changing  $\log \mathcal{U}$  amounts to changing  $Q_{\text{H}}$  and therefore the effective stellar mass, as more or fewer sources are needed for older and younger bursts, respectively, to produce sufficient ionizing photons to achieve the intensity specified by  $\log \mathcal{U}$ . Following the same convention as Byler et al. (2017), we define the rate of ionizing photons *per solar mass* as  $\hat{Q}_{\text{H}} \equiv Q_{\text{H}} / M_{\odot}$ , where  $Q_{\text{H}}$  is the rate of ionizing photons corresponding to the  $\log \mathcal{U}$  that sets the intensity for a given model in the Cloudy simulations. With this convention, output quantities can be recovered in terms of the initial stellar mass formed in the burst ( $M_0$ ) through multiplication by  $\hat{Q}_{\text{H}}/Q_{\text{H}}$ . Normalization of input or output intensities by  $M_0$  produces the intensity per  $1 M_{\odot}$  initial stellar mass formed in a burst. We specify this normalization throughout, where appropriate.

<sup>7</sup> We note that fixing  $R$  and varying only ionizing flux means certain geometric effects are not accounted for in these models; such geometrical effects can substantially change both high-ionization and neutral line emission (e.g., Ramambason et al. 2022).

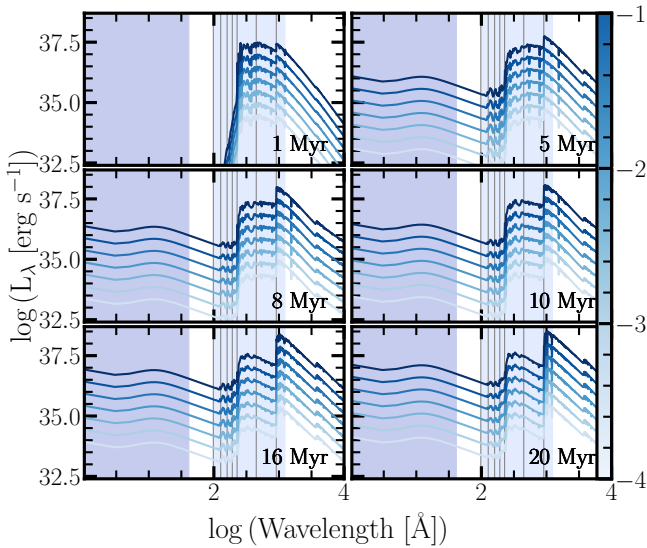


**Figure 5.** The composite SXP<sub>ULX</sub> + SSP SEDs at 0.1  $Z_{\odot}$  for a selection of instantaneous burst ages, normalized by a range of  $\log \mathcal{U}$  values, as noted in the colorbar. Models with high  $\log \mathcal{U}$  have the highest intensities, and correspond to the largest stellar mass formed in a burst. As in Figure 4, the darker blue shaded region shows the X-ray bandpass, the lighter blue shaded region encompasses the EUV regime, and the grey vertical lines denote a selection of relevant ionization potentials (13.6–126 eV, from right to left). Each composite SED is used as input for the `Cloudy` photoionization simulations.

With these parameters ( $t_{\text{burst}}$ ,  $Z$ , and  $\log \mathcal{U}$ ), the overall grid input to `Cloudy` consists of 147 separate models, corresponding to different combinations of the seven values for  $t_{\text{burst}}$ , three values for  $Z$ , and seven values for  $\log \mathcal{U}$ . In Figure 5, we show the [SXP<sub>ULX</sub> + SSP]( $t_{\text{burst}}$ ,  $Z$ ,  $\log \mathcal{U}$ ) models for select burst ages and the full range for  $\log \mathcal{U}$  for the 0.1  $Z_{\odot}$  case. The models with  $\log \mathcal{U} = -1$  have the highest intensities, or correspondingly, the largest stellar mass formed in a burst ( $Q_{\text{H}}/\hat{Q}_{\text{H}} \sim 10^4 - 10^6 M_{\odot}$  for  $\log \mathcal{U} = -1$  and  $t_{\text{burst}} = 1-20$  Myr).

We again employ a modified version of `CloudyFSPS` to create the relevant `Cloudy` input files for each model in the grid, execute `Cloudy` simulations, and organize the `Cloudy` output files. For each grid point, we allow the `Cloudy` simulations to iterate to convergence, up to a maximum number of five iterations, and set the stopping criteria for the calculations to when the cloud temperature falls below 100 K or the ionized fraction falls to 1%. Building on the nebular emission line lists presented in Byler et al. (2017) and Byler et al. (2018), we record intensities from 406 emission lines, spanning the far IR to the near UV. The full line list is included in the Ap-

pendix in Table A.1, including vacuum wavelength ( $\text{\AA}$ ), line name, and `Cloudy` specific line ID.

## 5. RESULTS

We highlight select results illustrating the importance of the time- and metallicity-dependence of the SXP<sub>ULX</sub> implementation, and provide potential diagnostics for investigating a SXP<sub>ULX</sub> ionizing contribution. We further describe the availability of our models and simulation results.

### 5.1. Characteristics of Nebular Emission Due to SXP<sub>ULX</sub> and Potential SXP<sub>ULX</sub> Diagnostics

A key result from the photoionization simulations is that the inclusion of the SXP<sub>ULX</sub> component does not significantly alter the *broad-band* colors in the UV-to-FIR relative to the case of the BPASS SSPs alone. This can easily be seen by looking at the enhancement in total nebular (line and continuum) emission due to the addition of the SXP<sub>ULX</sub>. In Figure 6 we show the fractional contribution of the nebular emission to the total flux as a function of wavelength and burst age in the top panel, and the percentage *enhancement* in this nebular flux due to the addition of the SXP<sub>ULX</sub> in the bottom panel. The nebular contribution to the total flux is high ( $> 50\%$ ) at all wavelengths on short burst timescales ( $\leq 5$  Myr, before the SXP<sub>ULX</sub> has turned on), and in the MIR for all burst timescales simulated here. However, as the bottom panel illustrates, the enhancement in nebular emission due to the inclusion of the SXP<sub>ULX</sub> is typically very small ( $< 5\%$ ). In the broad-band sense, the major effect of the SXP<sub>ULX</sub> is therefore to slightly prolong the ionizing output relative to the SSP alone, a consequence of the imposed age-dependence of our models relative to the BPASS SSPs.

Due to the shape of the SED<sub>ULX</sub> as extended through the EUV, a key outcome from the addition of the SXP<sub>ULX</sub> is a change to the intensity of lines with excitation potentials  $\geq 54$  eV. The `Cloudy` line list for our simulations (Table A.1) includes 63 lines redward of Ly $\alpha$  with ionization potential  $\geq 54$  eV (Kramida et al. 2022), of which 28 have ionization potentials in excess of 90 eV, including a number of so-called “coronal lines” (i.e., forbidden transitions with very high ionization potentials). In order to establish which of these high-excitation lines may be used as diagnostics for SXP<sub>ULX</sub> ionization, we consider lines redward of Ly $\alpha$  that satisfy the following criteria: (1) are relatively strong in the models with SXP<sub>ULX</sub> contribution, as measured in terms of median line flux relative to median flux in

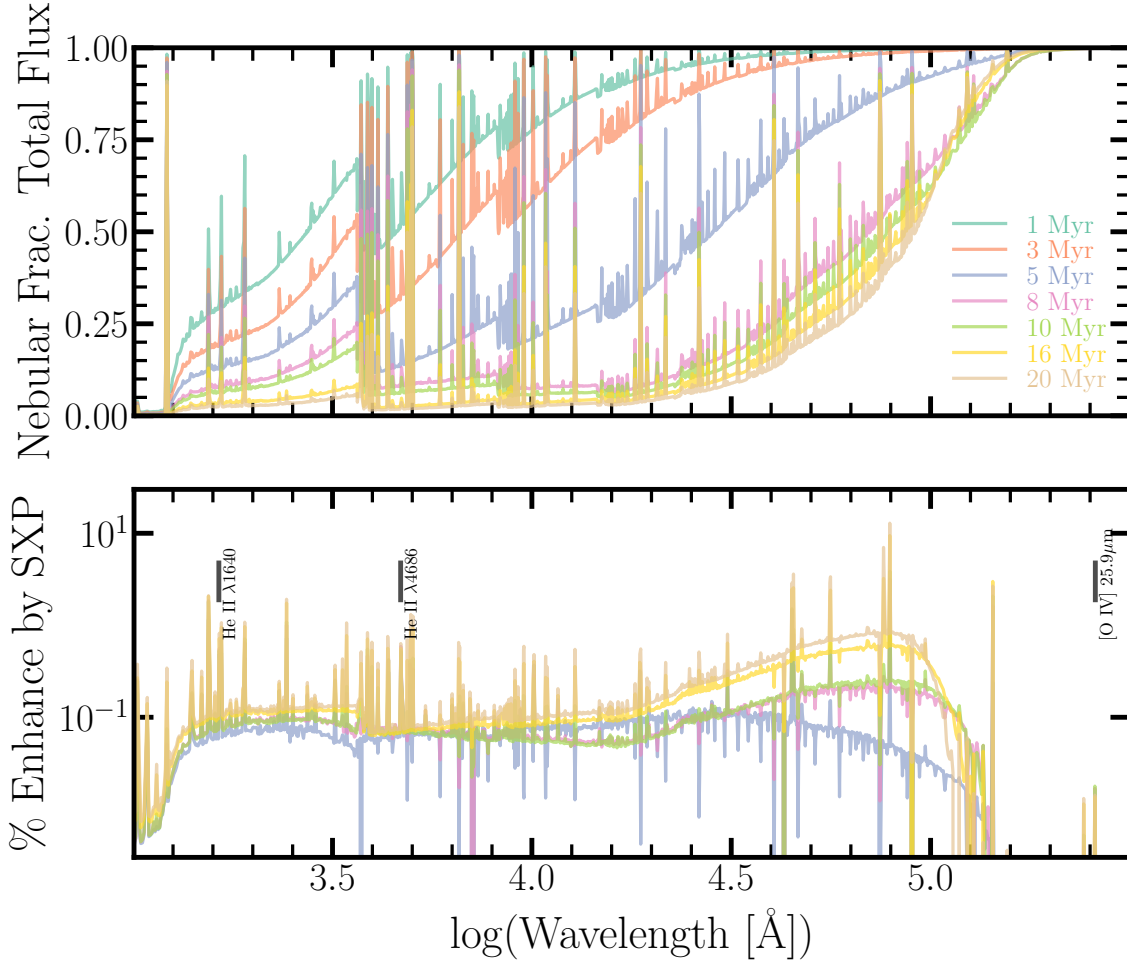


**Figure 6.** *Top:* The fractional contribution of the nebular line and continuum emission to the total flux (stellar and nebular) as a function of wavelength and instantaneous burst age for models with  $Z = 0.1 Z_{\odot}$  and  $\log \mathcal{U} = -1$ . *Bottom:* The percentage enhancement in nebular line and continuum flux due to the addition of the  $\text{SXP}_{\text{ULX}}$ . For all burst timescales simulated, the  $\text{SXP}_{\text{ULX}}$ -driven enhancement in the total nebular emission is typically small ( $< 5\%$ ). The black labels denote high-ionization species whose nebular *line* intensity is particularly enhanced due to the inclusion of the  $\text{SXP}_{\text{ULX}}$  component.

$\text{H}\beta$  or  $\text{Pa}\beta$ <sup>8</sup> (i.e.,  $\log(\tilde{f}_{\text{line}}/\tilde{f}_{\text{H}\beta}) \geq -3$  or  $\log(\tilde{f}_{\text{line}}/\tilde{f}_{\text{Pa}\beta}) \geq -3$ ); and (2) have a median enhancement in line flux by a factor of  $\sim 2\times$  relative to the SSP-only models ( $\log(\tilde{f}_{\text{line, SXP+SSP}}/\tilde{f}_{\text{line, SSP}}) \gtrsim 0.3$ ). There are only a select few emission lines satisfying both of these criteria: He II  $\lambda 1640$ , 4686, and [O IV] 25.8832  $\mu\text{m}$ . We annotate these lines in Figure 6, and note them in Table A.1 (\* flag).

In Figures 7–9 we show emission line diagnostic diagrams in the UV, optical, and IR, respectively, to highlight the potential for uncovering ionization due to an

$\text{SXP}_{\text{ULX}}$  using these lines. In general, diagnostic diagrams such as these are constructed using lines relatively close in wavelength to reduce the effects of reddening and make the lines used in the diagnostic accessible with a single instrument, reducing uncertainties due to cross-calibration. In all line diagnostic diagrams that follow, the  $[\text{SXP}_{\text{ULX}} + \text{SSP}](t_{\text{burst}}, Z, \log \mathcal{U})$  models (i.e., models *with*  $\text{SXP}_{\text{ULX}}$  contribution) are shown as the solid lines, where orange to dark blue lines represent metallicities from  $Z = 0.05$ – $1 Z_{\odot}$  and light blue to dark blue lines represent ionization parameters from  $\log \mathcal{U} = -4$  to  $-1$ . For all grids in the diagnostic plots, the star denotes the model with lowest metallicity ( $0.05 Z_{\odot}$ ) and highest ionization parameter ( $\log \mathcal{U} = -1$ ). The BPASS SSP-only models are shown as slightly transparent, dashed

<sup>8</sup> We use  $\text{H}\beta$  as the reference line for the high-ionization lines, which are mostly in the UV and optical, and  $\text{Pa}\beta$  for coronal lines in the IR.

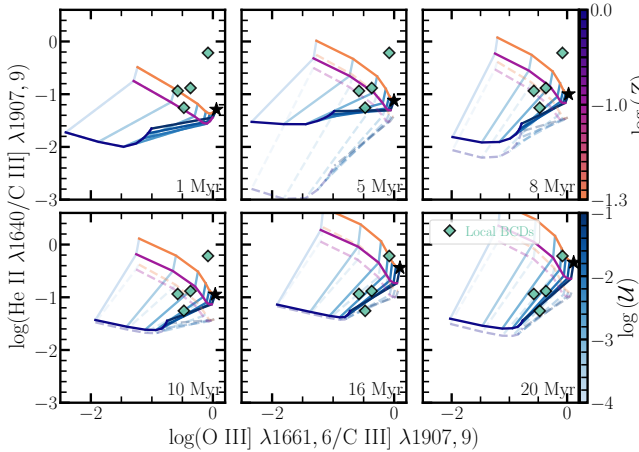


**Figure 7.** Potential UV diagnostic diagram for  $\text{SXP}_{\text{ULX}}$  ionization, as a function of instantaneous burst age. The  $[\text{SXP}_{\text{ULX}} + \text{SSP}](t_{\text{burst}}, Z, \log \mathcal{U})$  grid is shown as solid lines, where orange to dark blue lines represent metallicities  $0.05 Z_{\odot}$ – $Z_{\odot}$  and light blue to dark blue lines represent  $\log \mathcal{U} = -4$  to  $-1$ , as illustrated by the colorbars. In all panels, the star represents the  $0.05 Z_{\odot}$  and  $\log \mathcal{U} = -1$  grid point. The dashed transparent lines in the background show the corresponding grid with SSP ionizing contribution only. A sample of local BCDs for which these UV lines have been measured are shown as cyan diamonds, where the uncertainties in line ratios are smaller than the plotted points (Senchyna et al. 2017). The addition of the  $\text{SXP}_{\text{ULX}}$  hardens the ionizing spectrum at a given  $\log \mathcal{U}$ , thereby increasing the intensity of He II  $\lambda 1640$  relative to C III]  $\lambda 1907,9$ . This effect is more pronounced at solar metallicity for  $t_{\text{burst}} = 5$  Myr, following depletion of WR stars, and low metallicities with  $t_{\text{burst}} > 10$  Myr (bottom panels), following depletion of the most massive stars.

lines in the background with the same color scheme. In cases where the models with  $\text{SXP}_{\text{ULX}}$  contribution are indistinguishable from SSP-only models (e.g., burst ages  $< 5$  Myr), only solid lines are shown.

For the UV diagnostic in Figure 7, the  $(\text{O III}] \lambda 1661,6)/(\text{C III}] \lambda 1907,9)$  ratio is sensitive to the ionization parameter, C/O ratio (i.e., abundance pattern, see discussion in Section 5.3), and uses lines that are relatively strong in the UV (Byler et al. 2018). The He II  $\lambda 1640/\text{C III}] \lambda 1907,9$  ratio in this same diagram is sensitive to the hardness of the ionizing spectrum. For burst timescales where the  $\text{SXP}_{\text{ULX}}$  contributes ( $\geq 5$  Myr), this diagnostic illustrates that the ionizing spectrum is harder at all metallicities relative to the SSP-only models due to the inclusion of the  $\text{SXP}_{\text{ULX}}$ , resulting in stronger intensity of He II  $\lambda 1640$  relative to C III]  $\lambda 1907,9$  at the same ionization parameter.

For this set of line diagnostics, we compare the  $[\text{SXP}_{\text{ULX}} + \text{SSP}](t_{\text{burst}}, Z, \log \mathcal{U})$  grid to a sample of

local blue compact dwarf (BCD) galaxies from Senchyna et al. (2017) for which these same lines have been measured. While most of the data points from the BCDs (cyan diamonds) are consistent with both the SSP-only and  $[\text{SXP}_{\text{ULX}} + \text{SSP}](t_{\text{burst}}, Z, \log \mathcal{U})$  grid for ionization parameters  $\log \mathcal{U} \geq -3.0$ , the inclusion of the  $\text{SXP}_{\text{ULX}}$  increases the intensity of He II  $\lambda 1640$  relative to C III]  $\lambda 1907,9$ , particularly at low metallicities and older burst ages. The composite grid is therefore consistent even with the most extreme data point, but only at later times ( $> 10$  Myr). Given the relative sparsity of the metallicity sampling in our grids and in the absence of a more detailed age analysis—which we consider beyond the scope of this work—it is not clear from this qualitative comparison whether the SSP-only or  $\text{SXP}_{\text{ULX}}$  grid is preferred for such galaxies. Nonetheless, the comparison serves to illustrate how the addition of the  $\text{SXP}_{\text{ULX}}$  alters the parameter space spanned by the grid, therefore changing the range of physical properties consistent with the observed population. In the case of Figure 7, the addition of the  $\text{SXP}_{\text{ULX}}$  hardens the ionizing spectrum at a given  $\log \mathcal{U}$ , which in effect mimics an SSP with slightly lower metallicity.

For an optical emission line diagnostic we present Figure 8, where the  $[\text{N II}] \lambda 6584/\text{H}\alpha$  ratio is sensitive to metallicity and  $\log \mathcal{U}$  (among other parameters, e.g., Kewley et al. 2013), and the He II  $\lambda 4686/\text{H}\beta$  ratio again probes the hardness of the radiation field. Here we compare to a sample of star-forming galaxies with strong nebular He II emission from SDSS identified by Shirazi & Brinchmann (2012). A little under half of this sample lack Wolf-Rayet (WR) star features in their spectra (“Non-WR”; red triangles), while the remaining galaxies show evidence for broad emission line features due to the presence of WR stars (“WR”; blue circles). In general, SSP-only models have a difficult time reproducing the observed range of He II  $\lambda 4686/\text{H}\beta$ , as the dashed grids in Figure 8 illustrate. The  $[\text{SXP}_{\text{ULX}} + \text{SSP}](t_{\text{burst}}, Z, \log \mathcal{U})$  grid is capable of reproducing the observed intensities for a subset of these data points, notably those without clear WR features in their spectra and those with WR features at lower metallicities, but only for select grid points. In this case, the ability of the  $[\text{SXP}_{\text{ULX}} + \text{SSP}](t_{\text{burst}}, Z, \log \mathcal{U})$  grid to explain a subset of the galaxies with strong He II/ $\text{H}\beta$  where SSP-only models cannot is again a consequence of a harder radiation field due to the addition of the  $\text{SXP}_{\text{ULX}}$ . However, the magnitude of the increase to the ionizing photon rate due to the  $\text{SXP}_{\text{ULX}}$  is strongly dependent on SFH. In particular, the  $\text{SXP}_{\text{ULX}}$  contribution for this line ratio reaches a maximum for  $t_{\text{burst}} > 10$  Myr. This has important consequences for the compatibility of  $\text{SXP}_{\text{ULX}}$  models



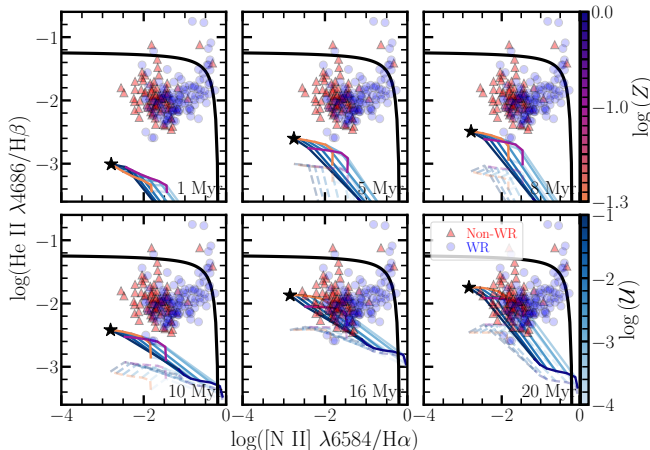


**Figure 8.** Same as Figure 7, but for a potential optical diagnostic diagram accounting for the inclusion of  $\text{SXP}_{\text{ULX}}$  ionization. The data points are a sample of star-forming galaxies from Shirazi & Brinchmann (2012) with strong nebular He II  $\lambda 4686$  emission (red triangles: galaxies without WR star features, blue circles: galaxies with WR star features). The black solid line is the empirically derived relation from Shirazi & Brinchmann (2012) to separate ionization due to star formation (below the line) versus ionization due to active galactic nuclei or composite populations (above the line). The models with  $\text{SXP}_{\text{ULX}}$  contribution overlap with the observed intensities for some of the Non-WR feature galaxies, particularly for  $t_{\text{burst}} > 10$  Myr and  $Z \leq 0.1 Z_{\odot}$ ; however, neither the  $[\text{SXP}_{\text{ULX}} + \text{SSP}](t_{\text{burst}}, Z, \log \mathcal{U})$  nor the SSP-only grids are capable of reproducing some of the more extreme galaxies, particularly those with detected WR features and higher N II/H $\alpha$  near the empirical maximum starburst line.

with the observed properties, such as age as inferred from equivalent widths (EWs), of some EELGs, a point we discuss in more detail in Section 5.2.

Interestingly, the observed WR feature galaxies at higher metallicities are difficult to reproduce using either the models with  $\text{SXP}_{\text{ULX}}$  ionizing contribution or SSP-only photoionization. This is primarily because such galaxies have large ratios of both He II  $\lambda 4686/\text{H}\beta$ , implying hard ionizing spectra, and  $[\text{N II}] \lambda 6584/\text{H}\alpha$ . We explore stellar population age in the context of this diagnostic in Section 5.2, metallicity in Section 5.3, and alternative ionizing sources in Section 6.3.2. Here we instead comment on the effect of stellar wind contamination of nebular emission. Lines such as He II can be produced either via stellar winds (broad emission line component) or photoionization (narrow emission line). Moderately good spectral resolution is therefore needed to distinguish the broad stellar from narrow nebular components for such lines (Brinchmann et al. 2008). If

not fully resolvable, residual emission from the broader stellar wind component could enhance the line intensity assumed to be purely nebular. It is likely that stellar wind contamination, if present, operates preferentially to inflate line intensities at higher metallicities, where line driven winds from massive stars are stronger (Vink et al. 2001). It is therefore important to consider the presence and magnitude of potential stellar wind contamination in observations of such nebular line species, particularly at higher metallicities, when comparing to the purely nebular line emission determined from photoionization simulations (e.g., Byler et al. 2018).

In the IR, we consider the diagnostic presented in Figure 9 for lines accessible with *JWST* (e.g., Weaver et al. 2010). Here the  $[\text{O IV}] 25.9\mu\text{m}/[\text{Ne III}] 15.66\mu\text{m}$  ratio is sensitive to hardness of the ionizing spectrum, while  $[\text{Ne III}] 15.66\mu\text{m}/[\text{Ne II}] 12.81\mu\text{m}$  is primarily sensitive to the ionization parameter. For this diagnostic, we include the classification regions from Richardson et al. (2022) for ionization due to pure star-formation (SF), SF/active galactic nuclei (AGN), and pure AGN, as well as the results from photoionization simulations for a  $10^3 M_{\odot}$  IMBH with fractional contribution 4–16% relative to a 20 Myr BPASS SSP (described in more detail in Section 6.3.2). The  $[\text{SXP}_{\text{ULX}} + \text{SSP}](t_{\text{burst}}, Z, \log \mathcal{U})$  grid is largely consistent with the pure SF region in this diagnostic, though offset from the SSP-only grid, again demonstrating how the addition of the  $\text{SXP}_{\text{ULX}}$  hardens the ionizing spectrum. The models including  $\text{SXP}_{\text{ULX}}$  contribution veer into the composite region for some of the solar metallicity  $t_{\text{burst}} = 5$  Myr models, and into the AGN ionization region only for lowest metallicities ( $\lesssim 0.1 Z_{\odot}$ ) and highest ionization parameters ( $\log \mathcal{U} > -3$ ) for bursts with  $t_{\text{burst}} > 10$  Myr. This indicates, not surprisingly, that the  $[\text{SXP}_{\text{ULX}} + \text{SSP}](t_{\text{burst}}, Z)$  photoionization signature looks less like pure SF when the fractional contribution of the  $\text{SXP}_{\text{ULX}}$  component relative to the SSP is most pronounced. As in Figure 7, this occurs when the strongest ionizing components of the stellar population are depleted, namely WR stars ( $\sim 5$  Myr at roughly solar metallicities) and the most massive stars that will explode as supernovae or collapse to a BH ( $> 10$  Myr). We note that the  $\text{SXP}_{\text{ULX}}$  grid does *not* significantly overlap with IMBH grids, suggesting some power in this emission line diagnostic for distinguishing between ionization due to BHs separated by orders of magnitude in mass; however, this too depends on how the accreting BH (at any mass) is scaled relative to the stellar population, a point that we return to in more detail in Section 6.3.2.

Finally, we comment on high-ionization lines that do not satisfy both criteria in terms of strength relative to

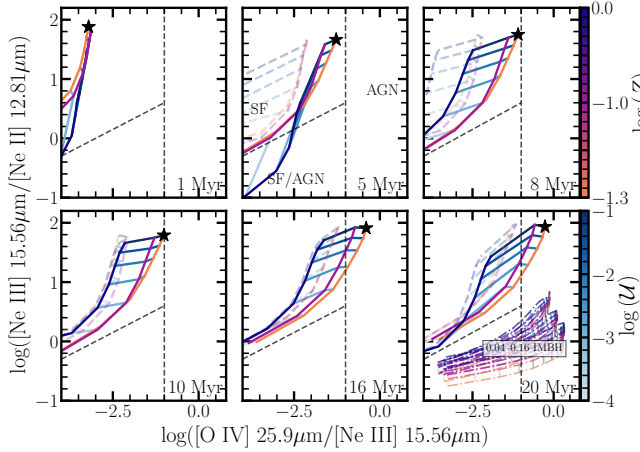


**Figure 9.** Same as Figure 7, but for a potential IR diagnostic diagram for SXP<sub>ULX</sub> ionization. The dot-dash grids are photoionization simulations of a  $10^3 M_{\odot}$  IMBH at different fractional contributions relative to a 20 Myr SSP from Richardson et al. (2022), where the color scheme is the same as for the [SXP<sub>ULX</sub> + SSP]( $t_{\text{burst}}$ ,  $Z$ ,  $\log \mathcal{U}$ ) grid for values  $\log \mathcal{U}$  and  $Z$  in common between the grids. The dashed lines show potential classification regions for pure star-formation ionization, composite star-formation and AGN ionization, and pure AGN ionization, also from Richardson et al. (2022), as annotated in the center top panel.

$H\beta$  or  $\text{Pa}\beta$  and enhancement relative to the SSP-only case. These lines fall broadly into three categories: (1) lines that are strong relative to  $H\beta$  or  $\text{Pa}\beta$ , but not significantly enhanced relative to the SSP-only models (flagged with † in Table A.1); (2) lines that are weak relative to  $H\beta$  or  $\text{Pa}\beta$ , but are significantly enhanced relative to the SSP-only models (flagged with ‡ in Table A.1); or (3) lines that are weak relative to  $H\beta$  or  $\text{Pa}\beta$  (including those with zero flux), and are not significantly enhanced relative to the SSP-only models (flagged with || in Table A.1). Lines flagged with † in Table A.1 have a median  $\log(\tilde{f}_{\text{line}}/\tilde{f}_{H\beta}) \sim -1.6$  and median enhancement of  $1.007\times$  in flux relative to the SSP-only models. By contrast, lines flagged ‡ in Table A.1 have  $\log(\tilde{f}_{\text{line}}/\tilde{f}_{\text{Pa}\beta}) \sim -6$ , but median enhancement of  $300,000\times$  in line flux relative to the SSP-only models. The latter case encompasses many coronal lines with ionization potentials  $> 90$  eV, i.e., the regime where the SSP provides relatively little flux, but the SXP<sub>ULX</sub> component is substantial. As such, there is a higher diagnostic potential for discerning the SXP<sub>ULX</sub> ionization contribution using coronal lines, many of which are in the IR, but only if the fractional contribution of the SXP<sub>ULX</sub> relative to the SSP is high enough to boost the line strengths into an easily detectable range.

We illustrate these two cases—moderately strong lines only marginally enhanced by the SXP<sub>ULX</sub> and weak lines heavily enhanced due to the addition of the SXP<sub>ULX</sub>—via additional emission line diagnostics in Figures 10–12. In Figure 10, we show the [SXP<sub>ULX</sub> + SSP]( $t_{\text{burst}}$ ,  $Z$ ,  $\log \mathcal{U}$ ) grid relative to the same sample of local BCD galaxies from as in Figure 7. Here, the grid with SXP<sub>ULX</sub> contribution is only slightly offset to higher values of C IV  $\lambda 1548,51/\text{O III } \lambda 1661,6$  compared to the SSP-only grid, reflecting the very modest enhancement in C IV  $\lambda 1548,51$  emission due to the SXP<sub>ULX</sub>. The lack of overlap between some of the galaxies and the grids in this diagnostic at later burst ages is likely a function of the adopted C/O ratio for the simulations in this work (see Section 5.3).

In Figures 11–12, we show emission line diagnostics in the optical and IR that include the high-ionization line [Ne V]. For these emission line diagnostics, the addition of the SXP<sub>ULX</sub> has a profound effect on the grid relative to the SSP-only case, given the ratio of [Ne V]/[Ne III] compares lines with ionization potentials of  $\sim 126$  eV and 64 eV, respectively. In Figure 11, the SSP-only models rarely reach  $\log([\text{Ne V } \lambda 3426]/[\text{Ne III } \lambda 3870]) > -5$ , while the grid with SXP<sub>ULX</sub> contribution begins to populate the composite region for low metallicities and high-ionization parameters (classification regions from Cleri et al. 2023). In Figure 12, the [SXP<sub>ULX</sub> + SSP]( $t_{\text{burst}}$ ,  $Z$ ,  $\log \mathcal{U}$ ) grid traces out a relatively narrow vertical track, distinct from the SSP-only and IMBH photoionization cases. However, for both of these diagnostics, the potential power for discerning SXP<sub>ULX</sub> contribution to the ionizing photon budget comes at the expense of line strength. The ratio of [Ne V]  $14.3\mu\text{m}/[\text{Ne III } 15.56\mu\text{m}]$  traced out by the grid with SXP<sub>ULX</sub> contribution spans roughly 10 orders of magnitude. Such lines are therefore undetectable for pure star-formation ionization and only potentially detectable (e.g., with *JWST*) with an SXP<sub>ULX</sub> ionizing contribution for a narrow range in  $\log \mathcal{U}$ ,  $t_{\text{burst}}$ , and  $Z$ . This implies that very high-ionization species such as [Ne V] or [Ar V] may be more reliable diagnostics of AGN or IMBH photoionization rather than SXP<sub>ULX</sub> ionizing contribution; however, the potential selection biases inherent in using particular lines should be considered in assessing the reliability of any such classification diagnostic (e.g., Richardson et al. 2022).

## 5.2. Consequences of Time Dependence of the SXP<sub>ULX</sub> Relative to the SSP

The key parameters affecting the time-dependence of the nebular emission from the [SXP<sub>ULX</sub> + SSP]( $t_{\text{burst}}$ ,  $Z$ ,  $\log \mathcal{U}$ ) grid are (1) the selection to impose a delay

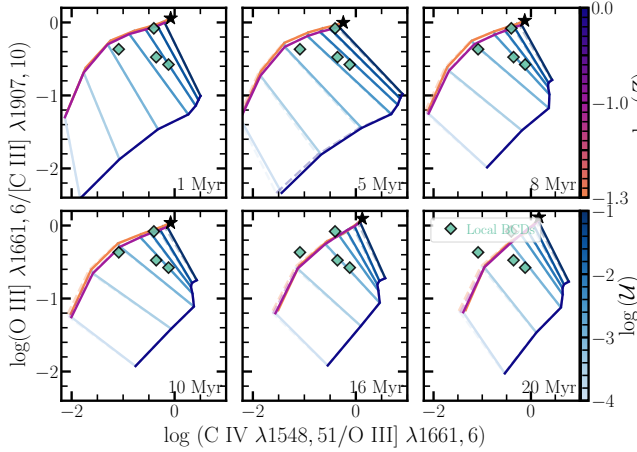


**Figure 10.** A UV emission line diagnostic where the SXP<sub>ULX</sub> contribution does not change the high-ionization line species appreciably relative to the SSP-only grid. The cyan diamonds are again a sample of local BCDs for which these UV lines have been measured (Senchyna et al. 2017).

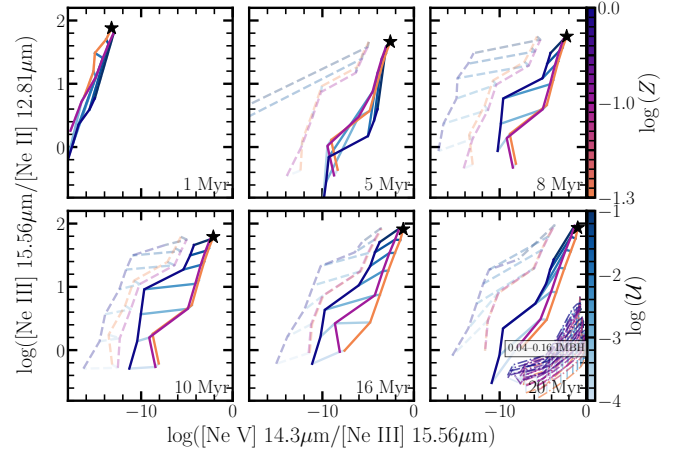


**Figure 12.** Same as Figure 11, but for a potential IR diagnostic, albeit using a weak coronal line that is highly sensitive to hardness of the ratio field. As in Figure 9, the IMBH models from Richardson et al. (2022) for a selection of IMBH fractional contributions are shown for reference.

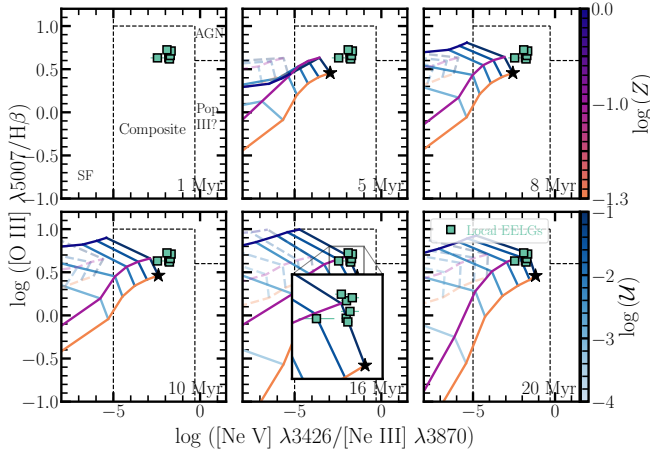


**Figure 11.** Same as Figure 7, but for a potential UV/optical diagnostic diagram for SXP<sub>ULX</sub> contribution. For these high-ionization lines, the SXP<sub>ULX</sub> contribution is substantial relative to the SSP-only case, but the high-ionization line intensities are generally weak except for select grid points (low metallicities and high  $\log \mathcal{U}$ ). The dashed lines illustrate classification regions for pure star-formation ionization, ionization from composite populations, ionization due to AGN, and potential ionization due to Pop III stars from Cleri et al. (2023). The cyan squares are the observed line ratios from a sample of local EELGs (Izotov et al. 2012; Berg et al. 2021; Olivier et al. 2022) that are consistent with select [SXP<sub>ULX</sub> + SSP]( $t_{\text{burst}}$ ,  $Z$ ,  $\log \mathcal{U}$ ) models in a very narrow range of grid space for older  $t_{\text{burst}}$  (e.g., see 16 Myr inset).

time for the SXP<sub>ULX</sub> to turn on and; (2) the combina-

tion thereafter with SSPs of *corresponding*  $t_{\text{burst}}$ . Imposing a delay time creates a scenario in which the SXP<sub>ULX</sub> prolongs the ionizing output of the population beyond that of the products of binary evolution already included in BPASS, as would be expected if the SXP<sub>ULX</sub> component is indeed descended from the stellar component, allowing time for compact object formation and accretion to begin. In this way, the SXP<sub>ULX</sub>, or accreting compact objects in general, are another way of rejuvenating the ionizing power from a population.

In spite of this, the magnitude of the *additional* contribution of the SXP<sub>ULX</sub> to the emergent nebular emission has time-dependent limits by virtue of being coupled to the time evolution of the SSPs. Although the absolute  $L_X/M_0$  scaling for the SXP<sub>ULX</sub> is largest for younger instantaneous bursts at all metallicities (Figure 1), the SXP<sub>ULX</sub> generally hardens the incident ionizing spectrum more profoundly *relative to the BPASS SSPs* at older burst ages. That is, the fractional contribution of the SXP<sub>ULX</sub> to the ionizing photon budget is typically highest for burst ages  $> 10$  Myr in the models considered here. This corresponds to the timescale on which the harder components of the stellar ionizing spectrum have been depleted (e.g., WR and other massive stars), while the SXP<sub>ULX</sub> component remains appreciable. Given the imposed delay time and coupling with BPASS SSPs, the SXP<sub>ULX</sub> contribution to the total rate of ionizing photons is  $\lesssim 2\%$  for burst ages between 5–10 Myr, and increases only to 5–7% on timescales  $> 10$  Myr.

The consequences of this time-dependence are particularly evident in Figures 8 and 11, where we compare

to observed samples of EELGs. In these figures, it is clear that the  $\text{SXP}_{\text{ULX}}$  ionizing contribution can only explain the high line ratios in the observed galaxies *for older*  $t_{\text{burst}}$ . This result has already been noted previously for other EELG samples. For example, a detailed investigation of the efficacy of different ionizing sources relative to a reference sample of metal-poor star-forming galaxies from [Plat et al. \(2019\)](#) found that products of binary evolution are capable of producing stronger high-ionization emission lines, but primarily for lower  $\text{EW}(\text{H}\beta)$ , which corresponds to older ages assuming a burst of star formation.

In addition to their strong high-ionization emission line ratios, many EELGs may in fact be characterized by young bursts of star formation. The sample of star-forming galaxies in [Plat et al. \(2019\)](#), have median  $\text{He II } \lambda 4686/\text{H}\beta \sim -1.9$ , and median  $\text{EW}(\text{H}\beta) \sim 160$ , corresponding to  $t_{\text{burst}} \sim 6$  Myr for BPASS burst models. Similarly, a sample of galaxies from SDSS DR7 and DR10 investigated by [Stasińska et al. \(2015\)](#) have median  $\text{He II } \lambda 4686/\text{H}\beta \sim -1.9$  and median  $\text{EW}(\text{H}\beta) \sim 110$ , corresponding to  $t_{\text{burst}} \sim 11$  Myr. While the models with  $\text{SXP}_{\text{ULX}}$  contribution can reach these values of  $\text{He II } \lambda 4686/\text{H}\beta$ , they only do so for  $t_{\text{burst}} > 10$  Myr, as illustrated in Figure 8. This timescale is incompatible with the measured  $\text{EW}(\text{H}\beta)$  values, assuming bursts of star formation, for some non-negligible portion of galaxies with strong  $\text{He II } \lambda 4686$  detections (e.g. [Stasińska et al. 2015](#); [Plat et al. 2019](#)). Thus, the  $\text{SXP}_{\text{ULX}}$  is unlikely to be a meaningful source of ionizing photons for the galaxies with very high EWs in such samples.

Figure 11 similarly underscores this point, where the local EELGs are consistent with the models with  $\text{SXP}_{\text{ULX}}$  contribution for a narrow range of the grid corresponding to  $\sim 0.1 Z_{\odot}$ ,  $\log \mathcal{U} > -2$ , and  $t_{\text{burst}} > 10$  Myr. However, five of the seven galaxies in this figure have measured  $\text{EW}(\text{H}\beta) \sim 100\text{--}260$ , corresponding to  $t_{\text{burst}} \sim 5\text{--}15$  Myr, and no clear correlation between EW and the strength of  $[\text{Ne V}] \lambda 3426/[\text{Ne III}] \lambda 3870$  ([Izotov et al. 2012](#)). The remaining galaxies presented in the figure have measured ages 1–10 Myr ([Olivier et al. 2022](#)). Assuming fidelity in these absolute ages (i.e., bursts of star formation), an  $\text{SXP}_{\text{ULX}}$  contribution may only be important for a small subset of these galaxies, with alternative source(s) required to explain the observed line intensities at high EWs (e.g., [Olivier et al. 2022](#)).

In summary, our models suggest select high-ionization emission line ratios can be produced by ionization due to an  $\text{SXP}_{\text{ULX}}$ , but only for  $t_{\text{burst}} > 10$  Myr and low metallicities. For galaxies where the SFH includes a young ( $< 10$  Myr) burst component, the  $\text{SXP}_{\text{ULX}}$  contribution to the ionizing photon budget is not significant enough

to reproduce the observed line ratios that include high-ionization lines such as  $\text{He II}$  or  $[\text{Ne V}]$ . This is because, for the models considered here, the pure stellar ionizing continuum is substantial for  $t_{\text{burst}} < 10$  Myr, resulting in strong emission from lines such as  $\text{H}\beta$ . This strong stellar ionizing flux effectively dilutes the  $\text{SXP}_{\text{ULX}}$  contribution, which primarily affects the high-ionization line (e.g.,  $\text{He II}$ ) rather than hydrogen ionization. We further illustrate this point in two ways. First, in Figure 13 we show nebular emission line luminosities normalized by stellar mass for  $\text{He II } \lambda 4686$ ,  $\text{H}\beta$ ,  $[\text{Ne V}] \lambda 3426$ , and  $[\text{Ne III}] \lambda 3870$  as a function of burst age. In comparing the evolution of the intensities of  $\text{He II}$  and  $\text{H}\beta$ , it is clear both lines reach their *absolute* maximum in intensity for  $t_{\text{burst}} \lesssim 3\text{--}5$  Myr; however, while the  $\text{H}\beta$  intensity drops by almost two orders of magnitude thereafter, the evolution of the  $\text{He II}$  intensity is much flatter over the same time span, owing to the  $\text{SXP}_{\text{ULX}}$  contribution, resulting in a higher ratio of  $\text{He II } \lambda/\text{H}\beta$  at later times. The same is true for  $[\text{Ne V}] \lambda 3426$  relative to  $[\text{Ne III}] \lambda 3870$ . For this ratio, it is also particularly evident when the  $\text{SXP}_{\text{ULX}}$  contribution turns for  $t_{\text{burst}} \geq 5$  Myr, as there is no appreciable  $[\text{Ne V}]$  emission prior to this.

To underscore the dominance of the stellar ionizing contribution relative to the  $\text{SXP}_{\text{ULX}}$  at early times, we reran the photoionization simulations without the strict delay-time dependence for the  $\text{SXP}_{\text{ULX}}$  component. For these “no-delay time” simulations, we extrapolated  $L_X/M_0$  from Figure 1 to burst ages 1–3 Myr, allowing the  $\text{SXP}_{\text{ULX}}$  to contribute to the ionizing budget at every time step. As Figure A.1 shows, the immediate formation of the  $\text{SXP}_{\text{ULX}}$  alongside a 1 Myr or 3 Myr burst only weakly increases  $\text{He II}/\text{H}\beta$ , given that the strength of the stellar ionizing continuum is still quite substantial on these timescales.

In this way, the addition of the  $\text{SXP}_{\text{ULX}}$  may contribute significantly to high-energy ionizing photon production only in some cases (e.g., EELGs characterized by bursts of star formation with  $\text{EW}(\text{H}\beta) < 120$ ). Such a caveat likely holds in general for other products of stellar or binary evolution with hard spectra that form preferentially on timescales  $\gtrsim 5$  Myr. The rejuvenating ionizing power from such sources simply comes too late to explain observed line intensities in high EW EELGs (e.g., [Jaskot & Oey 2013](#)). Other hard ionizing sources that are capable of operating on a range of timescales, including the earliest times post-starburst, *and* that have flexibility in their relative scaling with respect to the stellar population are therefore still required for EELGs with very young burst ages (e.g., shocks, very massive stars, IMBHs; [Senchyna et al. 2021](#); [Oskinova & Schaerer 2022](#)). To understand where the  $\text{SXP}_{\text{ULX}}$  ion-



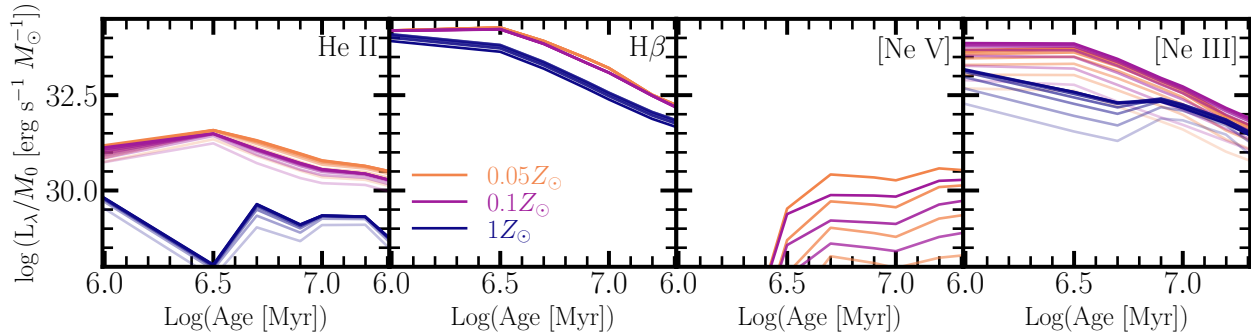


**Figure 13.** Nebular emission line luminosities normalized by stellar mass for He II  $\lambda 4686$ , H $\beta$ , [Ne V]  $\lambda 3426$ , and [Ne III]  $\lambda 3870$  as a function of burst age. As before, in each panel dark blue corresponds to  $Z_\odot$ , purple corresponds to  $0.1 Z_\odot$ , and orange corresponds to  $0.01 Z_\odot$  models. Increasing line opacity denotes increasing  $\log \mathcal{U}$ . The ratio of a high-ionization line (e.g., He II, [Ne V]) with significant SXP<sub>ULX</sub> contribution relative to a lower ionization line (e.g., H $\beta$ , [Ne III]) is largest at later times ( $> 10$  Myr), particularly for the lower metallicity models. This corresponds to the timescale on which the ionizing contribution from the stellar population has decreased significantly, while the SXP<sub>ULX</sub> ionizing contribution remains appreciable.

izing contribution may be most critical to high-energy ionizing photon production, measured SFHs or other proxies for age such as EW(H $\beta$ ) should be considered alongside emission line diagnostics when comparing observed samples with these models.

### 5.3. Consequences of Metallicity-Dependence of the SXP<sub>ULX</sub> and Adopted Abundance Patterns

The photoionization simulation results are based on the assumption that the metallicity of the SXP<sub>ULX</sub> corresponds to the stellar metallicity of the SSP, as would be expected if the SXP<sub>ULX</sub> and SSP form and evolve from the same parent stellar population. Consequently, a low-metallicity SSP, which already has a somewhat harder ionizing spectrum, will always be combined with an SXP<sub>ULX</sub> with higher formation efficiency ( $L_X/M_0$ ) than the SXP<sub>ULX</sub> combined with a solar-metallicity SSP.

The imprint of the metallicity-dependent normalization of the SXP<sub>ULX</sub> is particularly evident in emission line diagnostics that include metallicity-sensitive line ratios (e.g., [N II]/H $\alpha$ ). To illustrate the magnitude of this effect, we run simulations where we remove the correlation between the SXP<sub>ULX</sub> normalization and stellar metallicity. In these “no stellar metallicity dependence” simulations, we allow an SSP at a given  $t_{\text{burst}}$  to be coupled with an SXP<sub>ULX</sub> normalized using  $L_X/M_0$  from the orange curve (i.e., maximum) in Figure 1, regardless of the SSP metallicity. The results are shown in Figure A.2, where higher ratios of He II  $\lambda 4686$ /H $\beta$  are produced at a given [N II]/H $\alpha$ , particularly for the solar metallicity case. This results in much more overlap between the grid with the SXP<sub>ULX</sub> contribution and the observed data points, for a broader range of burst ages; however, we note that such an elevated  $L_X/M_0$  for ULXs

at solar metallicities is not supported by observations. Even allowing for variations due to stochastic sampling of the XLF, sources with  $L_X \gg 10^{39}$  erg s $^{-1}$  become more rare at higher metallicities, due to steepening of the bright end of the XLF with increasing metallicity (Lehmer et al. 2021). We therefore include this “no stellar metallicity dependence” example simply to illustrate the effects of our model choices.

While the SXP<sub>ULX</sub> may not be an efficient additional source of ionizing photons at high metallicity given the relations in Figure 1, other sources of high-energy ionizing photons may operate preferentially in this regime. For example, as pointed out in Shirazi & Brinchmann (2012), the sub-sample of galaxies with WR features in Figure 8 generally has higher metallicity, which correlates with higher stellar mass and SFR, and therefore potentially stronger stellar feedback. For such galaxies, this stronger stellar feedback (i.e., winds and supernovae) may drive shocks, which could be an additional source of high-energy ionizing photons (e.g., Section 6.3.3).

The choice to couple stellar and gas-phase metallicities and the adopted abundance patterns for these simulations are also of critical importance for select emission line diagnostics. Although  $L_X/M_0$  increases with decreasing metallicity thereby increasing the number of high-energy ionizing photons, at very low metallicities the absolute abundance of some elements will be low enough that this becomes the dominant factor in setting the line intensity (e.g., discussion in Senchyna et al. 2020). This can easily be seen in the shape of the [SXP<sub>ULX</sub> + SSP]( $t_{\text{burst}}$ ,  $Z$ ,  $\log \mathcal{U}$ ) grid in Figure 12, where the lowest metallicity models including SXP<sub>ULX</sub> contribution do not uniformly have

the strongest [Ne V]  $14.3\mu\text{m}$ /[Ne III]  $15.56\mu\text{m}$  ratios, as would be expected if  $\text{SXP}_{\text{ULX}}$  production efficiency (i.e.,  $L_{\text{X}}/M_0$ ) were the dominant factor in determining line strength.

Likewise, the adopted C/O ratio in the simulations affects the extent of the grids as presented in Figures 7 and 10. Our abundance pattern corresponds to  $\log(\text{C/O}) = -0.77$  for  $0.1 Z_{\odot}$ , and up to  $\log(\text{C/O}) = -0.33$  for  $Z_{\odot}$ . The former is close to the average value ( $\log(\text{C/O}) = -0.71$ ) measured from metal-poor star-forming dwarf galaxies from Berg et al. (2019), and within the large (0.17 dex) intrinsic dispersion on that value. Adopting a lower C/O ratio would shift the grids in Figure 10 up and to the left (Byler et al. 2018), thereby making the the models consistent with the full observational sample at all time steps.

The abundance ratios of C/O, N/O, and C/N in particular can be strongly affected by chemical enrichment history *and* the ability of a given galaxy to retain enriched gas for subsequent generations of star formation. These abundance ratios may therefore be a complex function of SFH, which modifies the dominant channel for enrichment (e.g., core-collapse supernovae versus asymptotic giant branch stars), and properties like the galaxy potential well. Given these complexities, we do not attempt a more detailed investigation of abundance pattern prescriptions here. However, we do note that the simulations presented in this work rest on the assumption that gas-phase and stellar metallicities are tied, whereas in some environments these may be decoupled (e.g., Steidel et al. 2016). If such a situation arises preferentially at higher redshifts because, for example, SFHs and therefore enrichment histories are substantially different than for local reference samples, the models presented here would not be an appropriate reference point given the adopted abundance patterns. Fortunately, *JWST* is now capable of directly probing abundance ratios out to these high redshifts (e.g., Arellano-Córdova et al. 2022), which will provide much improved constraints for tuning model abundance patterns going forward.

#### 5.4. Availability of Models

We make our models and simulation results available in two separate formats, as outlined below.

First, via a standalone github repository<sup>9</sup> (Garofali 2023), we provide the emission line intensities for all points in the grid ( $7 t_{\text{burst}} \times 3 Z \times 7 \log \mathcal{U}$ ) corresponding to the  $[\text{SXP}_{\text{ULX}} + \text{SSP}](t_{\text{burst}}, Z, \log \mathcal{U})$  model pre-

sented in this work (i.e., with all parameters specified in Section 4.) In this same repository, we provide code examples in `python` for reading and plotting simulation results, allowing users to quickly plot the  $[\text{SXP}_{\text{ULX}} + \text{SSP}](t_{\text{burst}}, Z, \log \mathcal{U})$  grid for different emission line diagnostics. Users can therefore compare data or other model grids to these simulations including  $\text{SXP}_{\text{ULX}}$  contribution. We likewise provide Table A.1 in a machine-readable format, such that lines can be selected on the basis of relevant flags included in the table notes.

We additionally make the models, including both spectra ( $\text{SED}_{\text{ULX}}$ ) and nebular and line continuum output from `Cloudy`, available directly from `FSPS`<sup>10</sup>, and `Python-FSPS` (Johnson et al. 2023). Accessing the nebular models with  $\text{SXP}_{\text{ULX}}$  contribution is only supported for BPASS SSPs in this release of `Python-FSPS`. The  $\text{SXP}_{\text{ULX}}$  contribution can be turned on by specifying the `add_xrb_emission = True` flag when initializing a stellar population model. With this flag specified, one can toggle on or off line and continuum emission (`add_neb_emission` and `nebelineinspec` parameters), switch between models with and without dust grains<sup>11</sup> in the cloud (`cloudy_dust` parameter), and change gas-phase metallicity and ionization parameter (`gas_logz` and `gas_logu` parameters) in the usual way.

The models included in `FSPS` are of a larger grid size ( $10 t_{\text{burst}} \times 11 Z \times 7 \log \mathcal{U}$ ) than the results presented here, but include a reduced line list (166 nebular emission lines). The larger grid size and reduced line list are required for parity in implementation with existing nebular models already included in `FSPS`. The expanded grid included in `FSPS` encompasses all the values of  $t_{\text{burst}}$ ,  $Z$ , and  $\log \mathcal{U}$  from the grid presented in this work. It includes three supplementary points in  $t_{\text{burst}} = \{2, 4, 12\}$  Myr, where the earlier bursts occur before the  $\text{SXP}_{\text{ULX}}$  has turned on, and the later supplementary  $t_{\text{burst}}$  is intermediate to timescales presented in this work for which the  $\text{SXP}_{\text{ULX}}$  provides some ionizing contribution. The expanded grid also includes 8 supplementary values in  $Z$ , namely  $Z = \{0.003, 0.004, 0.006, 0.008, 0.01, 0.014, 0.03, 0.04\}$ . Including these additional  $Z$  grid points requires interpolating the relations from Fragos et al. (2013b) shown in Figure 1. We therefore recommend proceeding with caution if employing models in `FSPS` that include the supplementary  $Z$  values quoted above, as the behavior of  $L_{\text{X}}/M_0$  as a function of  $Z$  and  $t_{\text{burst}}$  for these models is more uncertain. The reduced

<sup>10</sup> <https://github.com/cconroy20/fps/commit/4c527a9>

<sup>11</sup> Although we only present models in this work that include dust grains in the cloud, the models available in `FSPS` include simulations run both with and without dust grains in the cloud.

<sup>9</sup> <https://github.com/kgarofali/sxp-cloudy/tree/v1.0>

line list included in FSPS has been carefully selected to include lines that are most significant as  $\text{SXP}_{\text{ULX}}$  ionization diagnostics, as well other important nebular diagnostics. The lines included in the reduced list are bolded in Table A.1.

From FSPS, one can build SEDs for a population with or without  $\text{SXP}_{\text{ULX}}$  contribution, including consideration of nebular line and continuum emission. In this way, users can simulate spectro-photometric data for populations including  $\text{SXP}_{\text{ULX}}$  contribution for use in SED fitting codes (e.g., Johnson et al. 2021; Doore et al. 2023).

## 6. DISCUSSION

We have already presented potential UV, optical and IR emission line diagnostics for  $\text{SXP}_{\text{ULX}}$  ionization in Section 5. Here we present best practices for diagnosing  $\text{SXP}_{\text{ULX}}$  ionization when using X-ray observations, and summarize the results from this work relative to recent literature results for photoionization due to high-energy sources. We additionally present a brief discussion of alternative sources of hard ionizing photons and their connection to the  $\text{SXP}_{\text{ULX}}$  model presented here.

### 6.1. Caveats For Applying $\text{SXP}_{\text{ULX}}$ Formalism to X-ray Observations: Model Assumptions

The emergent  $L_X$  (0.5–8 keV) from the  $\text{SXP}_{\text{ULX}}$  models is very similar to the input  $L_X$  (i.e., Figure 1), as the hard photons are attenuated very little by the cloud. However, comparison of the simulation results with X-ray observations likely requires a more careful transformation of the intrinsic  $L_X$  from the simulations into a model for observed X-ray counts. We must consider of factors such as line of sight absorption (e.g., Wilms et al. 2000), viewing angle (e.g., Abolmasov et al. 2009; Kouvlikas et al. 2022), source variability (e.g., Earnshaw et al. 2018), and instrumental effects. Such considerations likely require a full forward-modeling approach (e.g., Gilbertson et al. 2022), but could allow the use of relatively low count X-ray data in spectro-photometric fitting (e.g., Doore et al. 2023). Nevertheless, implementation will be non-trivial, and we defer full consideration to a future work. Here, we instead provide caveats relevant for interpreting the simulation results with respect to the observations, given factors affecting X-ray detectability.

A primary consideration in interpreting  $L_X$  values from the photoionization simulations is that the  $\text{SED}_{\text{ULX}}$  model assumes a specific geometry appropriate to a supercritical accretion flow. In such a model, the wind or outflow component creates an effective funnel geometry, which collimates and scatters the harder

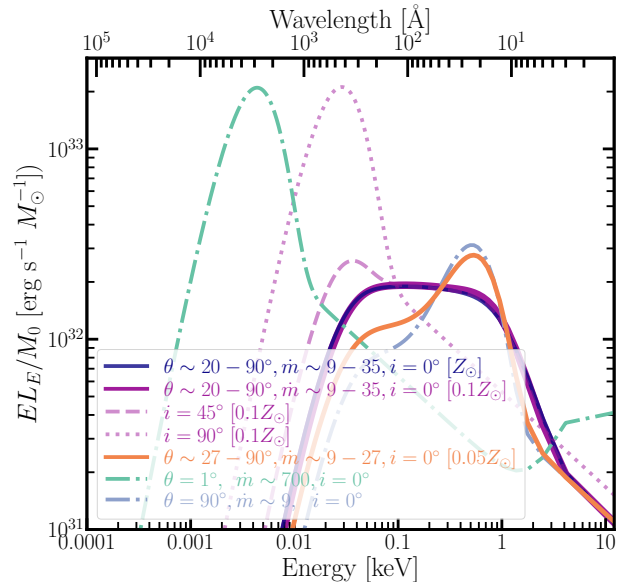


**Figure 14.** Same as Figure 3, but now illustrating the effect on the observed and intrinsic SED from changing the inclination angle ( $i$ ), and the mass transfer rate/funnel opening angle ( $\dot{m}/\theta$ ), respectively. The  $\text{SED}_{\text{ULX}}$ , which is the intrinsic model for the photoionization simulations where  $\theta$  and  $\dot{m}$  have a distribution of values, is shown via the solid lines for each of the three metallicities simulated in this work ( $Z_{\odot}$ : dark blue,  $0.1 Z_{\odot}$ : purple, and  $0.05 Z_{\odot}$ : orange). For the  $0.1 Z_{\odot}$  case, we show three viewing angles for observers:  $i = 0^{\circ}$  (solid purple line, face-on inclination),  $i = 45^{\circ}$  (dashed purple line, intermediate inclination), and  $i = 90^{\circ}$  (dotted purple line, edge-on inclination). We additionally show via dash-dot lines two bounding cases for the shape of the intrinsic SED, where the values of  $\theta$  and  $\dot{m}$  are still tied to one another, but single-valued for the whole population:  $\theta = 1^{\circ}$  for all sources (light green), and  $\theta = 90^{\circ}$  for all sources (light blue).

inner disk emission for face-on viewers and may obscure this component for more edge-on viewing angles (e.g., Begelman et al. 2006; Poutanen et al. 2007; King et al. 2023). Under this geometry, the observed  $L_X$  depends on inclination angle ( $i$ ), and also on the mass supply rate ( $\dot{m}$ ) itself. We discuss how changes to each of these parameter values changes the observed and intrinsic SED for the population, respectively.

In all simulations, we assume  $i = 0^{\circ}$ , such that the cloud sees all components of the accretion flow. In Figure 14, we show the effect on the *observed* SED shape from changing the viewing angle for the  $0.1 Z_{\odot}$  case. The intrinsic model ( $i = 0^{\circ}$ ) is shown by the solid purple line, while the SED for an intermediate viewing angle ( $i = 45^{\circ}$ ) is shown with the dashed purple line, and for a perfectly edge-on inclination ( $i = 90^{\circ}$ ) by the dotted purple line. The transition from a face-on to an edge-

on viewing angle reduces the apparent (observed) hard-band X-ray emission, and increases the apparent EUV–to–UV emission as the quasi-spherical outflow component begins to dominate the line-of-sight emission.

In this same figure, we also show the effect on the *intrinsic* SED from changing the dominant mass transfer rate ( $\dot{m}$ ) and therefore funnel opening angle ( $\theta$ ) assumed for the population. In the  $\text{SED}_{\text{ULX}}$  model (dark blue, purple, and orange solid lines), the ratio of  $L_{\text{obs}}/L_{\text{Edd}}$  sets the mass transfer rate, and therefore beaming factor and funnel opening angle. Because  $L_{\text{obs}}$  is sampled from the metallicity-dependent XLF, the  $\text{SED}_{\text{ULX}}$  is constructed from a *distribution* of values in  $\dot{m}$ ,  $b$ , and  $\theta$ . We show the effect of assuming  $\dot{m}$  is single-valued for the entire  $\text{SXP}_{\text{ULX}}$  via the light green and blue dash-dot lines in this figure. The light green line corresponds to the case where all sources in the population are highly super-Eddington ( $\dot{m} \sim 700$ ,  $\theta = 1^\circ$ ), while the light blue line corresponds to a population of entirely mildly super-Eddington accretors ( $\dot{m} \sim 9$ ,  $\theta = 90^\circ$ ). For a population with solely highly super-Eddington mass transfer rates, where all sources have very small funnel opening angles, the SED shape is dominated by the outflow component, which is a pseudo-blackbody peaking in the UV. By contrast, for the population composed solely of sources with mildly super-Eddington mass transfer rates, the accretion disk component dominates the emission, resulting in an SED that peaks at soft X-ray wavelengths. The  $\text{SED}_{\text{ULX}}$  model employed in this work is intermediate to these two bounding cases, as it includes contribution from sources ranging from mildly to highly super-Eddington, and it accordingly spans EUV to hard X-ray wavelengths.

The diversity of observed spectral shapes for ultra-luminous sources may therefore be explained by differences in both funnel opening angle and viewing angle. For example, ultra-luminous supersoft sources (e.g., Soria & Kong 2016; Urquhart & Soria 2016) may represent accreting compact objects with modest mass supply rates and large funnel opening angles viewed edge-on, while ultra-luminous UV sources may be compact objects with higher mass transfer rates likewise viewed edge-on (e.g., Kaaret et al. 2010).

Unfortunately, the dependence of mass transfer rate (or lack thereof) on funnel opening angle, and corresponding distribution of funnel opening angles is not well-known for either the intrinsic or the observed ULX population. Some binary population synthesis models suggest that the dominant accretor population (i.e., BH versus NS) and the timescale on which they appear will affect the fraction of the population that is strongly beamed (e.g., Wiktorowicz et al. 2019). In this respect,

the form of the  $\text{SED}_{\text{ULX}}$  used in this work is not exhaustive. The key assumptions for the  $\text{SED}_{\text{ULX}}$  model are that the distribution of observed luminosities for the population is described by the empirical metallicity-dependent XLF, that these observed luminosities can be mapped back to an intrinsic mass transfer rate ( $\dot{m}$ ), and that the mass transfer rate itself is tied to the beaming factor and funnel opening angle ( $\theta$ ). The latter two selections are made to reduce the number of predetermined parameter values. The former selection to adopt a particular functional form for the XLF, including using best-fit parameter values from Lehmer et al. (2021), is analogous to making a selection for the form of the IMF, which often includes selection of parameters such as slope and upper mass limit cutoff.

Different assumptions about typical values for ULX parameters such as  $\theta$  and  $\dot{m}$ , or even the form of the XLF for ULXs, will therefore propagate to the intensities of high-ionization nebular emission lines. In practice, this could work to either increase or decrease the line intensities, or perhaps even alter the strict age-dependence for particular line ratios given a model that is extreme enough in the EUV. A more detailed investigation of the effect of these parameters on the resultant nebular emission is therefore beyond the scope of the present work.

Despite these caveats about model assumptions, we demonstrate the applicability of our models to observations via a comparison of simulated and observed He II  $\lambda 4686/\text{H}\beta$  as a function of  $L_{\text{X}}/\text{SFR}$  (a typical observable for HMXB and ULX populations; e.g., Mineo et al. 2012; Kovelakas et al. 2020). For the observational comparison set, we use a sample of star-forming dwarf galaxies for which there are spectra from SDSS, *HST*/COS, and MMT, and X-ray coverage from *Chandra* (Senchyna et al. 2020). Given the aforementioned caveats to X-ray detectability, comparison of our simulations with this observed sample rests on the assumption that the observed  $L_{\text{X}}$  corresponds roughly to the  $L_{\text{X}}$  from the intrinsic (simulated) population. Additionally, given the discussion in Section 5.2, we must consider whether the SFH assumed for the simulated results is appropriate to the observed sample (i.e., line intensities, SFRs, and  $L_{\text{X}}$  are time-averaged in a similar way). For the observed sample, line intensities are derived from the spectroscopic data, and the corresponding SFRs and values for  $L_{\text{X}}$  (or upper limits) are determined from the same spectroscopic aperture, or within  $1.4''$  of the aperture for the X-ray data. SFRs are measured using calibration constants derived from BPASS appropriate to the effective age and metallicity of the stellar population assuming continuous star formation.



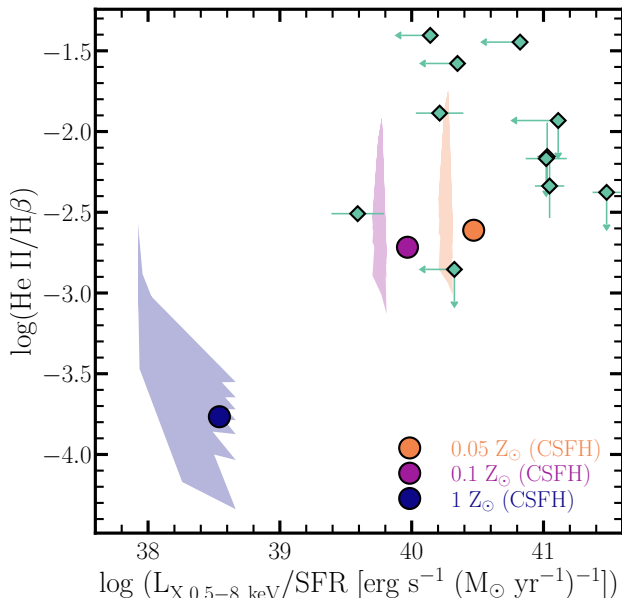


**Figure 15.** The emergent  $L_X$  (0.5–8 keV)/SFR relative to the strength of He II  $\lambda 4686/H\beta$  from photoionization simulations with SXP<sub>ULX</sub> contribution for both continuous star formation (circles) and instantaneous bursts (shaded regions). As before, metallicities are color-coded and labeled. Observed values for a sample of star-forming dwarfs from Senchyna et al. (2020) are shown as green diamonds. The low metallicity simulations are consistent with all but the most extreme observed values and upper limits for the line ratios and  $L_X/SFR$ ; however, this requires instantaneous bursts where  $t_{\text{burst}} > 10$  Myr. Models with continuous SFHs produce  $L_X/SFR$  in the range of the observed galaxies and upper limits, but much lower ratios of He II  $\lambda 4686/H\beta$ .

To produce a simulated comparison set, we consider both burst and continuous SFH cases. The burst properties are easily recoverable from the simulations, as shown in figures throughout. To recover the continuous SFH case, we integrate the simulated line intensities and SXP<sub>ULX</sub>  $L_X$  (both in terms of stellar mass) assuming a constant SFR of  $1 M_{\odot} \text{ yr}^{-1}$ . The results are shown in Figure 15, with the continuous SFH models as circles and the burst models as shaded regions, where the extent of the region encompasses the range of simulated  $\log \mathcal{U}$  and  $t_{\text{burst}}$ . The most extreme line ratios are achieved for high  $\log \mathcal{U}$  and older  $t_{\text{burst}}$ . The simulations can reproduce much of the observed range of He II  $\lambda/H\beta$  (green diamonds) for reasonable  $L_X/SFR$  (i.e., overlap with detections, or are below upper limits); however, this is true only for instantaneous bursts of star formation where  $t_{\text{burst}} > 10$  Myr. For the continuous SFH case, the models produce much more modest He II  $\lambda/H\beta$  and there is much less overlap with the observed sample.

This demonstrates that the assumed SFH is of critical importance in such comparisons, and that, as discussed in Section 5.2, proxies for age are integral to determining the importance of SXP<sub>ULX</sub> high-energy ionizing contribution.

As some of the observed galaxies in Figure 15 have values of  $L_X/SFR$  in excess of the simulated results, we briefly comment on the effects of sampling in making such comparisons. In general, testing for agreement between the simulated results for  $L_X$  and an observed population is best achieved when the observed population has a well-sampled XLF. This typically holds in the high SFR regime ( $\gtrsim 3 M_{\odot} \text{ yr}^{-1}$ ), where the effects of stochastic sampling of the XLF are on the order of, or smaller than, the model uncertainties on  $L_X$ , and where the strict linear scaling of  $L_X$  with SFR holds (Grimm et al. 2003; Justham & Schawinski 2012; Lehmer et al. 2021). In the low SFR regime, on the other hand, integrated  $L_X$  (obs) can be subject to large ( $\sim 0.7$  dex) scatter due to stochastic sampling of an XLF that, for HMXBs and ULXs, flattens at the bright end (e.g., Lehmer et al. 2021). Similar but far less severe considerations about statistical sampling apply when determining and comparing SFRs. Empirical or model-derived calibration constants for different SFR indicators are based on the assumption of a fully populated IMF and SFR indicators which have equilibrated. In other words, typical calibration constants are appropriate for regions physically large enough for the IMF to be well-sampled and for which the SFH has been continuous long enough for a given SFR indicator to reach equilibrium (e.g., 5–100 Myr Kennicutt 1998; Kennicutt & Evans 2012). The galaxies in Figure 15 that are X-ray detected with the highest  $L_X/SFR$  ( $\gtrsim 10^{41} \text{ erg s}^{-1}$ ) are some of the most distant galaxies ( $D > 200$  Mpc) in the sample, such that the spectroscopic apertures encompass large areas on the sky, making it unlikely that statistical sampling affects the measured SFRs. These galaxies have measured SFRs in the range  $0.003\text{--}6 M_{\odot} \text{ yr}^{-1}$ , and therefore may be subject to significant sampling effects at the low SFR end; however, stochastic sampling is likely not enough to explain their high X-ray production efficiencies, even at the very low SFR end, making them  $\sim 2\sigma$  outliers relative to empirical scaling relations at low metallicities (Lehmer et al. 2021). These galaxies may therefore represent cases where alternative high-energy ionizing sources with  $L_X/SFR$  well in excess of average XRB scaling relations contribute to the observed line ratios (e.g., Section 6.3.2).

Taken together, the discussion presented here implies that in order to determine whether  $L_X$  from a given SXP<sub>ULX</sub> is consistent with observations requires model-

ing the effects of inclination, both on the *observable* spectral components and their *apparent* luminosities (e.g., Kovelakas et al. 2022), as well as consideration of the effects of sampling. The former is a critical consideration in the context of these simulations, as it implies an SXP<sub>ULX</sub> may be intrinsically very luminous, and therefore efficient at producing high-energy ionizing photons, while potentially being difficult to detect in X-rays. The latter is important because all line intensities (either for bursts or calculated for continuous SFH) are simulated assuming a population average  $L_X$ . For highly star-forming galaxies, the population average  $L_X$  may be a good approximation; however, if these conditions do not hold for an observed sample, comparison with simulation results may result in erroneous inferences about population age, metallicity, and/or source(s) of ionization.

### 6.2. Comparison with Recent Literature

There have been a number of works in the literature exploring the efficacy of X-ray sources in the production of high-energy ionizing photons, with a particular recent emphasis on the X-ray contribution to production of He II  $\lambda 4686$  in high-redshift galaxies and their analogs (e.g., Kehrig et al. 2018, 2021; Schaerer et al. 2019; Senchyna et al. 2020; Simmonds et al. 2021; Oskinova & Schaerer 2022; Kovelakas et al. 2022; Umeda et al. 2022; Ramambason et al. 2022). The most recent investigations fall broadly into two categories: (1) full photoionization simulations of the ionizing effect of an X-ray source coupled to a stellar population; and (2) analytic approximations for the X-ray source contribution to select line intensities, such as He II  $\lambda 4686$ . We focus on the former here for parity with our own implementation.

In Figure 16 we show in yellow the SED<sub>ULX</sub> for a 5 Myr instantaneous burst of star formation at  $0.1 Z_\odot$ . We select the  $0.1 Z_\odot$ , 5 Myr grid point for this comparison, as it has the highest ionizing photon production efficiency ( $\xi_{\text{ion}}$ ) for any grid point with SXP<sub>ULX</sub> contribution ( $\log(\xi_{\text{ion}}) \sim 25.4$  [Hz erg<sup>-1</sup>]), similar to the range of ionizing photon production efficiencies for EELGs (e.g., Olivier et al. 2022). Here the SED<sub>ULX</sub> has been normalized to  $1 M_\odot$  stellar mass formed, corresponding to  $L_X$  (0.5–8 keV)  $\sim 1 \times 10^{33}$  erg s<sup>-1</sup>. The corresponding SSP is shown in green, while the composite of these two components is shown in black. The additional labeled SEDs (“MCD”, “DIS”, “BB”, “I Zw18”, and “ $Z \sim 0.3 Z_\odot$  galaxy ensemble”) are selections from the literature that have previously been used in photoionization simulations or targeted as high redshift analogs for SED studies. Below, we briefly summarize salient points from

recent investigations using these SEDs, and compare to our findings based on the SXP<sub>ULX</sub> framework.

The photoionization simulations performed in Senchyna et al. (2020) explored the effect of HMXBs on production of He II  $\lambda 4686$  and [Ne V]  $\lambda 3426$ . The authors couple an HMXB model, represented via a multi-color disk SED (“MCD”, green dotted line in Figure 16) at different BH masses ( $\sim 10$ – $100 M_\odot$ ) to BPASS stellar populations ( $Z = 0.001$ – $0.020$ ) assuming continuous star formation. The HMXB component is scaled to the stellar population for a range of X-ray production efficiencies ( $L_X/\text{SFR} = 10^{40}$ – $10^{44}$  erg s<sup>-1</sup> ( $M_\odot$  yr<sup>-1</sup>)<sup>-1</sup>). Much like our approach, they used a modified version of CloudyFSPS to initialize the Cloudy input grid, employing a similar range in  $\log \mathcal{U}$ . With these simulation inputs, the authors conclude that the observed range of He II  $\lambda 4686/H\beta$  can only be reproduced for extremely high X-ray production efficiencies ( $L_X$  (0.5–8 keV)/SFR  $> 10^{42}$  erg s<sup>-1</sup> ( $M_\odot$  yr<sup>-1</sup>)<sup>-1</sup>). Such extreme X-ray production efficiencies are not observed, even in nearby extremely metal-poor galaxies, and are likely excluded by reionization-era constraints (Lehmer et al. 2021; HERA Collaboration et al. 2023). In Figure 15 we compare our model line predictions with the observational sample from Senchyna et al. (2020) which they used, in part, to draw the conclusion that HMXB ionization is insufficient to explain the observed range of He II  $\lambda 4686/H\beta$ . As already discussed in Section 6.1, our simulations are able to reproduce more of the observed range of He II  $\lambda 4686/H\beta$  within the observed range of  $L_X/\text{SFR}$ , but primarily for instantaneous bursts with  $t_{\text{burst}} > 10$  Myr at low metallicities. Under the assumption of a continuous SFH, as in Senchyna et al. (2020), our models are not able to reproduce the more extreme values of He II  $\lambda 4686/H\beta$  at the simulated range of  $L_X/\text{SFR}$ . This underscores the importance of the assumed SFH in setting line ratios; however, even for similar assumptions about the SFH, our models produce stronger He II  $\lambda 4686/H\beta$  at a given  $L_X/\text{SFR}$  as compared with Senchyna et al. (2020), which we attribute to differences in the assumed SED shape. Our SED<sub>ULX</sub> is much flatter through the EUV than the multi-color disk model, and therefore produces more ionizing EUV photons per  $L_X$ .

The importance of the form of the SED to the production of high-energy ionizing photons was highlighted in the Cloudy photoionization simulations from Simmonds et al. (2021). These authors explored the photoionizing effect of ULXs using several empirical models for the ULX SED coupled to a BPASS SSP (1 Myr instantana-

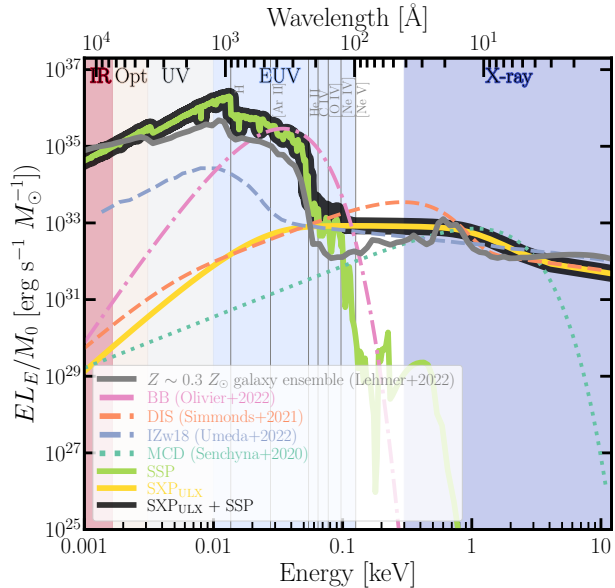


**Figure 16.** The intrinsic SED for the composite model (SXP<sub>ULX</sub> + SSP, solid black line) with  $t_{\text{burst}} = 5$  Myr and  $Z = 0.1 Z_{\odot}$ , normalized to  $1 M_{\odot}$  stellar mass formed. The stellar population and SED<sub>ULX</sub> components of the composite are shown in green and yellow, respectively. Various SEDs from the literature that have previously been used in photoionization simulations are shown in different colors and line styles for comparison, all normalized to the same  $L_X$  (0.5–8 keV) (or, in the case of the “BB”,  $L_{\text{EUV}}$ ) as the SED<sub>ULX</sub>. As a grey solid line, we also show the intrinsic SED, including contributions from stars, hot gas, and HMXBs, from recent modeling of an ensemble of low-metallicity galaxies (Lehmer et al. 2022). All SEDs have been normalized to the same 0.5–8 keV luminosity for plotting purposes. The grey vertical lines mark ionization potentials for select lines, as labeled.

neous burst with  $Z = 0.005^{12}$ ) again for a similar range in  $\log \mathcal{U}$  as employed here. In their simulations, the ULX contribution is scaled relative to the BPASS SSP for a range of  $L_X/\text{SFR}$ , motivated by empirical scalings and scatter therein. These authors find they can reproduce some of the observed range of He II  $\lambda 4686/\text{H}\beta$  for reasonable X-ray production efficiencies ( $L_X/\text{SFR} \simeq 10^{40} - 10^{41} \text{ erg s}^{-1} (M_{\odot} \text{ yr}^{-1})^{-1}$ ), roughly in agreement with our findings for instantaneous bursts and the SED<sub>ULX</sub> model.

In general, the simulation results presented in Simmonds et al. (2021) also achieve higher values of He II  $\lambda 4686/\text{H}\beta$  than our grids with SXP<sub>ULX</sub> contribution, at least for their most optimistic SED model

(“DIS” from Berghea & Dudik 2012, as shown via the orange dashed line in Figure 16). We attribute differences in high-energy ionizing photon production efficiency between simulations, ostensibly both for ULX-type sources, in part to differences in adopted SED shape, and in part to treatment of how the ULX component is scaled relative to the stellar population as a function of metallicity and burst age. As is evident from Figure 16, the “DIS” model has a stronger soft X-ray excess than our SED<sub>ULX</sub>, leading to a different shape when extended into the EUV, particularly around 54 eV where He II  $\lambda 4686$  has its ionization potential. While our SXP<sub>ULX</sub> simulations are run coupled to a range of SSPs with  $L_X/M_0$  scaled as a function of burst age and metallicity, the simulations in Simmonds et al. (2021) are performed by scaling the ULX component to a single BPASS SSP (1 Myr,  $\sim 0.3 Z_{\odot}$ ) using a range of  $L_X/\text{SFR}$ . This amounts to relaxing the assumptions used here for scaling of the SXP<sub>ULX</sub> formation efficiency with SSP metallicity and age, and the requirement for a delay time for ULX formation. In this way, the approach in Simmonds et al. (2021) complements the average efficiencies employed in the SXP<sub>ULX</sub> simulations: using a broad range of  $L_X/\text{SFR}$  for a given  $Z$  and  $t_{\text{burst}}$  is akin to simulating a large degree of scatter in the X-ray production efficiency for that SSP.

The investigation from Lehmer et al. (2022) did not perform photoionization modeling, but targeted a sample of star-forming, low-metallicity galaxies with excellent multi-wavelength coverage, including X-ray detections from *Chandra*. This multi-wavelength coverage enabled direct measurements of the high-energy emission, including contributions from HMXBs and hot gas, relative to stellar emission from high-redshift analog galaxies. In this work, the authors constrain the stellar component of the galaxies in their sample using broadband photometry from *GALEX*, SDSS, PanSTARRS, 2MASS, and WISE, and measure the hot gas and HMXB contributions using data from *Chandra*. The empirically-constrained intrinsic SED from the full ensemble of galaxies (grey line in Figure 16) is produced from the physically motivated models for the stars, hot gas, and HMXBs that describe the observed multi-wavelength data, after removal of attenuation and nebular and dust emission. This SED is qualitatively similar to the SXP<sub>ULX</sub> + SSP model used in this work (black line in Figure 16), albeit with some differences in the EUV range, particularly around 54 eV. This is the regime where the SED from Lehmer et al. (2022) is dominated by emission due to hot gas and stars, with an HMXB contribution that is a factor of  $\approx 2\text{--}10\times$  lower than that of the hot gas emission. In our models, there

<sup>12</sup> These authors list the metallicity of the BPASS SSP as  $12 + \log(\text{O}/\text{H}) = 8.1$ . For their adopted abundances from Grevesse et al. (2010), this corresponds to  $\sim 0.3 Z_{\odot}$ , which we assume corresponds to the BPASS  $Z = 0.005$  model.

is no hot gas component, but the ULX contribution remains appreciable relative to the stellar ionizing continuum across the EUV range, which explains the difference between the two models. However, it is important to note that the contribution from HMXBs or ULXs relative to any hot gas component is subject to large fluctuations owing to stochastic sampling of the XLF, especially at low SFRs as discussed in Section 6.1. As such, the HMXB-to-hot gas normalization could differ by an order of magnitude from the value used for the grey model in Figure 16, depending on the host galaxy SFR and metallicity. Comprehensive accounting of high-energy ionizing photon production from a given star-forming galaxy will therefore benefit from consideration of stellar and XRB components, as presented here, as well as hot gas or shock components, as presented in Lehmer et al. (2022) and Oskinova & Schaerer (2022), and discussed in Section 6.3.3.

While the simulations and observed samples in Senchyna et al. (2020), Simmonds et al. (2021), Lehmer et al. (2022), and this work explore HMXBs and ULXs specifically, there are other recent approaches to the high-energy ionizing photon production question that take a more agnostic approach to source type. In Umeda et al. (2022), the authors attempt to parametrically constrain the EUV shape of the intrinsic ionizing spectra for a sample of extremely metal-poor galaxies. To do so, they construct SEDs consisting of parametrized power-law and blackbody components which they run through Cloudy. They then use MCMC to determine the parameters of these SED components that best describe a set of observed high-ionization emission lines from the sample of extremely metal-poor galaxies. Their best-performing models for each galaxy are then compared with more physical SEDs, in this case BPASS SSPs coupled to different ionizing sources such as ULX or AGN, to infer physical properties of the ionizing population. In Figure 16, we show the results of this approach for one of their galaxies, I Zw18 (blue dashed line), for which there exist excellent broad-band multi-wavelength coverage (i.e., X-ray, optical, and high-ionization nebular emission lines). We note that the results are remarkably consistent with our  $\text{SED}_{\text{ULX}}$  component, despite very different approaches in (re)constructing the intrinsic ionizing spectrum.<sup>13</sup> In general, using their full galaxy sample, Umeda et al. (2022) show that the intensity of the

observed high-ionization emission lines requires different combinations of BPASS SSPs (in terms of burst age) and ULX-like components with various scaling factors relative to the SSPs. Our  $[\text{SXP}_{\text{ULX}} + \text{SSP}](t_{\text{burst}}, Z)$  grid is constructed with these various scaling factors determined from theoretical binary population synthesis models, while in Umeda et al. (2022) the characteristic burst ages and necessary scaling factors for the high-energy ionizing photon production are inferred from the best parametric fits after comparison with physical models. The two approaches are therefore quite complementary, and highlight that determining the sources that contribute to high-energy ionizing photon production may require consideration of not only different sources of ionizing photons, but also their relative contributions as a function of stellar population age and metallicity.

As a final point of comparison, we highlight the results from Olivier et al. (2022), where the authors fit the high-ionization emission lines in a set of nearby EELGs with very young ( $\lesssim 10$  Myr) and metal-poor ( $\sim 0.1 Z_{\odot}$ ) stellar populations. These authors find that BPASS SSPs alone cannot reproduce the observed strengths of some of the highest ionization potential species, such as He II and [O IV]. To reproduce the strengths of such lines, they opt to add an 80,000 K blackbody to the BPASS SSPs scaled to a relatively large fractional contribution (45–55%) to the total luminosity. We show such a blackbody component in Figure 16 as the pink dash-dot line (“BB”). As already discussed in Section 6.1, the  $\text{SED}_{\text{ULX}}$  includes a pseudo-blackbody component, albeit at slightly different temperature and normalization than the blackbody employed in Olivier et al. (2022). However, the temperature of the roughly blackbody component of the  $\text{SED}_{\text{ULX}}$  and its relative contribution to the total composite SED depends on the specific assumptions about the accretion flow geometry, accretor type and mass, and mass supply rate, and our  $\text{SED}_{\text{ULX}}$  model is certainly not exhaustive in these respects. Thus, an EUV blackbody source that is not easily detectable at X-ray wavelengths as employed in Olivier et al. (2022) is not necessarily incompatible with an SXP origin (e.g., Figure 14).

These results highlight a few crucial considerations for simulating photoionization due to an SXP-like source. Namely, the results depend heavily on the assumed SED shape for this additional ionizing component, and on how the component is scaled relative to the stellar population. Unfortunately, we still do not have tight empirical constraints on either of these ingredients for the case of ULXs specifically, or XRBs more broadly. However, as these photoionization simulation results suggest, select high-ionization emission lines may offer an addi-

<sup>13</sup> The ionizing spectra appear more discrepant in the UV-to-IR range, however, this regime was not the focus of the modeling in Umeda et al. (2022), and therefore had the smallest contribution (in terms of data sets used) to constraining the best-performing model.



tional lever arm for inferring the shape of unseen portions of the SED. The approaches presented in Umeda et al. (2022) and Olivier et al. (2022), for example, have the potential to be very powerful, but the recovered best-performing models depend critically on the suite of lines available for fitting as well as the set of parametric models considered. Whether using parametric or physically-motivated models as inputs to the photoionization simulations, larger grids are likely necessary going forward. We consider the recent approaches highlighted here important first steps in this process.

### 6.3. Alternative Ionizing Sources

For the  $\text{SXP}_{\text{ULX}}$  model used in this work, we have assumed the accretor is a stellar mass BH ( $\sim 10\text{--}100 M_{\odot}$ ) and have constructed the  $\text{SED}_{\text{ULX}}$  accordingly. In this section, we discuss the effects of changing these assumptions about the accretor (both mass and type), and additional processes capable of producing high-energy ionizing photons.

#### 6.3.1. Neutron Star ULXs

While the simulations presented here consider only the case of stellar mass BH accretor for ULXs, there is now direct and growing observational evidence for NS accretors in ULXs, via the detection of pulsations (e.g. Bachetti et al. 2014; Fürst et al. 2016; Israel et al. 2017; Carpano et al. 2018). Swapping the BH for a NS accretor in the  $\text{SXP}_{\text{ULX}}$  would result in a few fundamental differences, both in terms of longevity of the ionizing output relative to the stellar population and potentially the SED shape.

For the SSPs considered in this work ( $t_{\text{burst}} \leq 20$  Myr) BHs should dominate the accretor demographics, while NS likely become the main accretor population at later times (e.g., Wiktorowicz et al. 2019). The addition of NS ULXs to the  $\text{SXP}_{\text{ULX}}$  would therefore further prolong the ionizing output of a population, beyond that of the most massive stars and binaries, and the BH  $\text{SXP}_{\text{ULX}}$  presented here. Furthermore, because the stellar ionizing contribution begins to wane considerably on timescales  $> 20$  Myr after the massive star population is depleted, any additional source of high-energy photons present on these timescales will provide a larger fractional contribution to the overall ionizing photon budget. However, the contribution of different accretor demographics to the total  $L_X/M_0$  will be both SFH- and metallicity-dependent, and such a population breakdown for the scaling relations is not yet well-constrained theoretically or observationally.

In addition to timescale differences, the spectral shape and upper limit for the luminosity may well be different

for NS accretors relative to stellar mass BHs in the supercritical regime. This is primarily due to the fact, in the case of a NS, the Eddington limit and accretion flow geometry may be modified by the presence of a strong magnetic field. In calculating the Eddington limit, the electron scattering cross section is typically given as the Thomson scattering cross section; however, in the presence of a strong magnetic field, this cross section may be reduced, effectively changing the radiation pressure term in Equation 1, and increasing the Eddington limit for a given mass (Paczynski 1992). Indeed, there is recent evidence for cyclotron resonance scattering features in the spectra of both a ULX and a hyper-luminous X-ray source ( $L_X > 10^{41}$  erg  $\text{s}^{-1}$ ), which implies the presence of an accreting NS with very strong magnetic field (Brightman et al. 2018, 2022). It is important to note, however, that an increase in Eddington limit due to a NS with a strong magnetic field is not mutually exclusive with a strongly super-Eddington mass supply rate (e.g., Bachetti et al. 2022), which may also lead to driving an outflow (e.g., King & Lasota 2016; King et al. 2017).

A strong dipole field also funnels accreted material onto the poles of the NS (i.e., creates an accretion column) and possibly further modifies the picture of the supercritical accretion flow presented in Section 2.3.2, depending on how the extent of the Alfvén radius ( $R_M$ ) compares to the spherization radius ( $R_{\text{sph}}$ ). King et al. (2023) present a very detailed review and discussion of the current landscape of models for supercritically accreting NS, both pulsing and non-pulsing. Despite this attention to modeling, there exists no, to our knowledge, energetically self-consistent model in e.g., XSPEC for a NS ULX that allows for modeling the effects of a strong magnetic field as well as inclination-dependence on the resultant SED. We consider further investigation of the NS ULX contribution to the  $\text{SXP}_{\text{ULX}}$  a promising avenue for future study, but outside the scope of the present work.

#### 6.3.2. Intermediate Mass Black Holes

Moving up in the mass scale, IMBHs ( $100 M_{\odot} \leq m \leq 10^6 M_{\odot}$ ) have been proposed as an additional source of ionizing photons relative to stellar populations (e.g., Hatano et al. 2023). As relatively massive BHs with moderate to low mass transfer rates relative to Eddington, IMBHs may also have SEDs with a substantial EUV component. In Figure 17, we compare the  $\text{SED}_{\text{ULX}}$  with IMBH SEDs for a  $10^3 M_{\odot}$  BH and  $10^5 M_{\odot}$  BH based on the `qsosed` model (Kubota & Done 2018), all normalized to the same  $L_X$  (0.5–8 keV) for plotting purposes. As Figure 17 shows, it can be difficult to distinguish be-

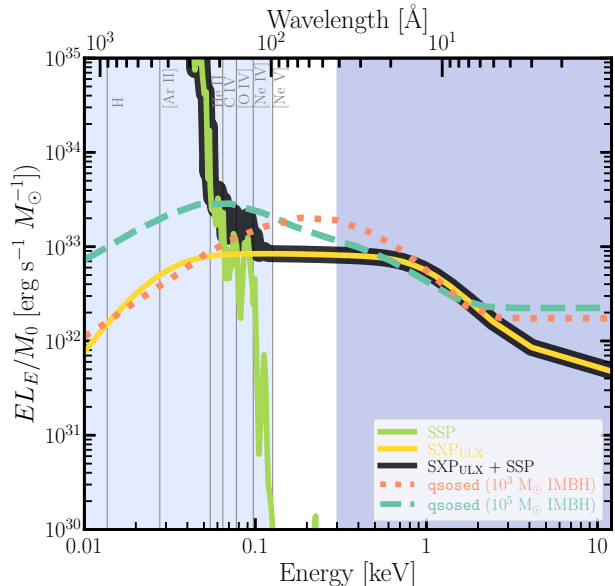


**Figure 17.** Similar to Figure 16, but for a comparison with  $10^3 M_\odot$  and  $10^5 M_\odot$  IMBH SEDs (orange dotted and green dashed lines, respectively), as employed in the photoionization simulations from Richardson et al. (2022). All SEDs are normalized to the same  $L_X$  (0.5–8 keV) for plotting purposes. In the absence of broad-band X-ray coverage, it can be difficult to distinguish between the SXP<sub>ULX</sub> and IMBH SEDs, particularly the sources are similar in bolometric luminosity and sub-dominant relative to the stellar population. However, differences in the intrinsic SEDs in the EUV-to-soft X-ray regime may result in some diagnostic power for distinguishing between these different ionizing sources using high-ionization nebular emission lines. Ionization potentials for a selection of lines are labeled and marked by grey vertical lines.

tween a ULX and IMBH for sources of similar bolometric luminosity that are sub-dominant with respect to the stellar population, particularly in the absence of broad-band X-ray coverage. However, differences in the SED shapes in the EUV imply there is diagnostic power with high-ionization lines for discerning ionization by accreting BHs of different masses. We provide a preliminary exploration of this via a comparison with select results from the IMBH photoionization simulations presented in Richardson et al. (2022).

The full set of IMBH photoionization simulations from Richardson et al. (2022) is expansive, encompassing different BH masses, prescriptions for the IMBH SED, mixing methodologies between the IMBH and stellar population, and a relatively fine gridding in stellar metallicity and  $\log \mathcal{U}$ . We compare only with the subset of their results most closely matching our simulation inputs and set-up. Namely, we show only their simulations for a  $10^3 M_\odot$  IMBH (qsosed model) combined with a 20 Myr

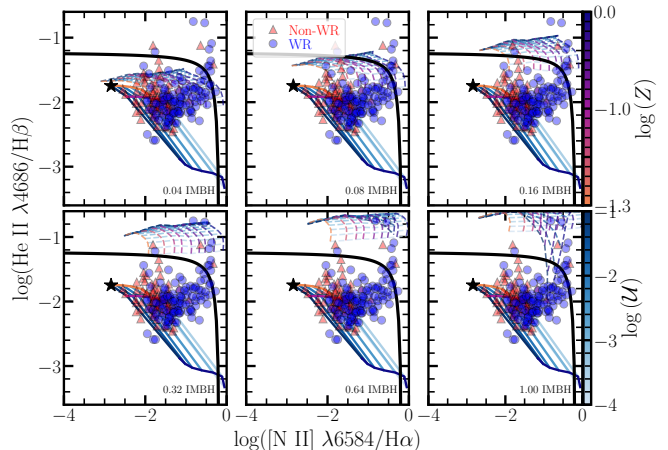


**Figure 18.** Similar to Figure 8, but with each panel showing only the 20 Myr [SXP<sub>ULX</sub> + SSP]( $t_{\text{burst}}$ ,  $Z$ ,  $\log \mathcal{U}$ ) grid (solid lines), relative to grids covering similar  $\log \mathcal{U}$  and  $Z$  with different fractional IMBH contributions (dashed lines) from Richardson et al. (2022), where the IMBH contribution is annotated in the lower right of each panel. Emission line diagnostics including high-ionization species such as He II  $\lambda 4686$  can be useful for distinguishing between ionization due to SF versus accreting black holes across the mass scale (i.e., SXP<sub>ULX</sub>, IMBH, AGN); however, classification regions depend on the fractional contribution of the additional ionizing source (e.g., SXP<sub>ULX</sub> or IMBH) relative to the stellar population, and whether this contribution scales strongly as a function of metallicity and burst age.

BPASS SSP assuming coincident mixing and a closed cloud geometry for grid points with  $-2 \leq \log(Z) \leq 0$  and  $-4 \leq \log \mathcal{U} \leq 1$ . In Figures 9 and 12 we plot their simulation results for IMBHs with fractional contributions  $\leq 16\%$  relative to the 20 Myr SSP (bottom right panels).

The comparisons in Figures 9 and 12 illustrate that there is strong diagnostic potential with very high-ionization line species for distinguishing between the ionizing impact of BHs across orders of magnitude in mass (e.g., Cann et al. 2018; Richardson et al. 2022). Offsets between the IMBH grids and grid with SXP<sub>ULX</sub> contribution in these emission line diagnostics are driven primarily by SED shape, suggesting these particular line ratios are sensitive to BH mass. However, this implies the diagnostic power hinges on assumed SED shape for a given BH mass, as well as typical fractional contribution of the BH ionizing component relative to the stellar population.

To more clearly show the differences due to changing IMBH ionizing fraction, in Figure 18 we instead plot different fractional contributions of the IMBH (from 4–100%) relative to the SSP in each panel, as compared

only with the 20 Myr  $[\text{SXP}_{\text{ULX}} + \text{SSP}](t_{\text{burst}}, Z, \log \mathcal{U})$  grid from this work. As before, the black solid line represents the empirically derived star formation/AGN demarcation, which the grid with  $\text{SXP}_{\text{ULX}}$  contribution never exceeds, and the IMBH grids only exceed for ionizing contribution  $\geq 16\%$ . In addition to the fractional contribution relative to the stellar population, differences between the grids in this diagnostic space also depend critically on how the additional ionizing component is scaled with respect to the metallicity of the stellar population. For example, the IMBH simulations that we compare to do not include a metallicity-dependence for the scaling of the IMBH component relative to the SSP. In this way, the IMBH grids are produced in a fashion similar to our “no metallicity-dependence” model (e.g., Figure A.2), and can therefore achieve more extreme line ratios across a range in metallicities from solar to sub-solar. If instead the typical IMBH mass scales with stellar population metallicity, some regions of the IMBH grids as presented here would potentially be excluded. Harnessing the full power of such emission line diagnostics for investigating BH ionizing impact across the mass scale will therefore likely require careful consideration of typical host galaxy environments for ULXs and IMBHs, and how this affects their scaling and mixing with stellar populations (e.g., Polimera et al. 2022; Richardson et al. 2022).

### 6.3.3. Shock Ionization

While the grid with  $\text{SXP}_{\text{ULX}}$  contribution presented here is capable of reproducing some of the range of observed line ratios for high-ionization emission lines, the models fail elsewhere. This implies the need either for tweaks to the  $\text{SXP}_{\text{ULX}}$  implementation, or consideration of some alternative energetic process.

Here we explore the ionizing impact of fast radiative shocks, which have been considered by many others as a potential source of the requisite high-energy ionizing photons to explain the observed line intensities in select EELGs (e.g., Thuan & Izotov 2005; Izotov et al. 2012; Plat et al. 2019; Izotov et al. 2021). However, instead of suggesting fast shocks as an *alternative* source of ionizing photons relative to the  $\text{SXP}_{\text{ULX}}$ , we consider them as an *additional* source related to the  $\text{SXP}_{\text{ULX}}$  itself.

The accretion flow model prescribed for the  $\text{SXP}_{\text{ULX}}$  in this work includes a quasi-spherical outflow component, which will likely interact with the surrounding medium. The interaction of ULX outflows with the interstellar medium is fairly well motivated by observations. A number of nearby ( $\lesssim 10$  Mpc) ULXs have been observed to sit inside large ( $> 100$  pc) bubbles. Such nebulae may be radiatively or mechanically in-

flated (e.g., Cseh et al. 2012; King et al. 2023). Several very bright ULXs show more direct evidence for the presence of fast outflows via the detection of blue-shifted absorption lines in high-resolution X-ray spectra (Poutanen et al. 2007; Pinto et al. 2016; Kosec et al. 2018a,b). Very recently, a detailed optical spectroscopic study of a ULX with direct evidence for fast outflows, as well as a bubble detection, confirmed the ULX wind or jet likely drives bubble expansion (Gúrpide et al. 2022). And indeed, investigation of the emission line diagnostics for such ULX bubbles reveal signatures of shock and photoionization (e.g., Abolmasov et al. 2007; López et al. 2019; Gúrpide et al. 2022). Therefore, in at least *some* cases, ULX feedback is sufficient to inflate a bubble and drive both shock and photoionization.

The  $\text{SED}_{\text{ULX}}$  model employed here, by virtue of including the outflow component, is therefore capable of driving shock ionization as well as photoionization, though we model only the latter in this work. Detailed shock and precursor ionization model grids are available from MAPPINGS (Allen et al. 2008), which may in principle be matched to a corresponding  $\text{SXP}_{\text{ULX}}$  to simulate the combined signature of shock and photoionization. However, including the effects of shocks self-consistently alongside  $\text{SXP}_{\text{ULX}}$  photoionization, assuming the shock is driven by the  $\text{SXP}_{\text{ULX}}$  itself, will likely require more than the addition of separate grids. In all simulations presented here we assume the gas is uniformly distributed in the cloud, but the presence of shocks related to the  $\text{SXP}_{\text{ULX}}$  (or indeed the stellar population) could preferentially displace gas from certain regions of the cloud. This may lead to shock ionization occurring in regions with different density than where the primary photoionization is occurring (e.g., Izotov et al. 2021). Such a non-uniform density may also alter the intensities of typical strong lines such as [O III], which is produced in the inner regions of the cloud. If gas is displaced from the central regions, this would amount to effectively lowering the ionization parameter for species such as [O III], relative to species produced elsewhere in the cloud (e.g., Kewley et al. 2013). It is clear a more careful treatment of joint consideration of  $\text{SXP}_{\text{ULX}}$  shock and photoionization is warranted in terms of timescales, cloud properties, and mixing methodologies to understand the overall effects on typical line diagnostics. Given the modeling complexities, we defer consideration of joint  $\text{SXP}_{\text{ULX}}$  shock and photoionization to a future related work.

As a final note, we remark that the presence of relatively ubiquitous ULX outflows implies the potential for feedback that can strongly shape the interstellar medium, akin to feedback from stellar winds and su-

pernovae. For example, a  $10^7 M_{\odot}$  instantaneous burst of star formation yields  $\sim 10^{40}$  erg  $s^{-1}$  mechanical luminosity over the course of 10 Myr as the most massive stars evolve and explode as supernovae (e.g., [Leitherer et al. 1999](#); [Prestwich et al. 2015](#)). From Figure 1, a  $\lesssim 0.1 Z_{\odot}$  SXP<sub>ULX</sub> provides  $\sim 10^{39}$ – $10^{40}$  erg  $s^{-1}$  mechanical luminosity for the same instantaneous burst, assuming ULX mechanical luminosity on par with radiative output. For at least some observed ULXs, it appears mechanical power from the outflow actually exceeds radiative power, suggesting the above estimate may even be a lower limit for SXP<sub>ULX</sub> feedback (e.g. [Justham & Schawinski 2012](#); [Pinto et al. 2016](#); [Gúrpidé et al. 2022](#)). Feedback from an SXP<sub>ULX</sub> could therefore contribute to favorable conditions for ionizing photon escape (e.g., similar to the scenario for stellar populations from [Jaskot & Oey 2013](#)). Indeed, resolved studies of Lyman continuum leakers at X-ray wavelengths suggest ULXs could be an important source of mechanical feedback, facilitating the escape of ionizing photons by carving channels in the surrounding medium ([Prestwich et al. 2015](#); [Kaaret et al. 2017](#)). An SXP<sub>ULX</sub> with strong outflow component could therefore be important for (1) producing high-energy ionizing photons via both shock and photoionization; (2) facilitating ionizing photon escape; and (3) producing the soft ( $< 2$  keV) photons that can more efficiently heat the intergalactic medium prior to the epoch of reionization (e.g., [Das et al. 2017](#); [HERA Collaboration et al. 2023](#)). As such, continued attention to modeling SXP<sub>ULX</sub>-like sources is extremely relevant to high redshift studies.

## 7. SUMMARY

In this work, we have presented a framework for combining a “simple X-ray population” alongside the corresponding simple stellar population in a physically consistent and meaningful manner in order to simulate and explore their combined ionizing impact as a function of (1) instantaneous burst age and (2) metallicity. Using our combined SED as input to the photoionization code `Cloudy`, we have produced a nebular line and continuum emission grid, which we make publicly available. Our principal findings can be summarized as follows:

- The addition of the SXP<sub>ULX</sub> prolongs the ionizing output relative to single massive stars or the products of binary evolution already included in BPASS. This is a consequence of the physically robust combination of an SXP<sub>ULX</sub> to the corresponding BPASS SSP with relative scaling factors determined as a function of burst age and stellar metallicity. Namely, the SXP<sub>ULX</sub> is scaled with an increasing fractional contribution as a function of

decreasing stellar metallicity, in line with empirical constraints, and combined only with an SSP of the corresponding age, following the expectation that the SXP<sub>ULX</sub> evolves from the parent stellar population.

- For the burst timescales modeled here ( $t_{\text{burst}} \leq 20$  Myr) the ionizing photons due to the SXP<sub>ULX</sub> contribute no more than  $\sim 5\%$  to the total nebular line and continuum emission. Broad-band FIR-to-UV colors are therefore not strongly affected by the addition of this component, relative to the case of a stellar-only ionizing component.
- Given that the SXP<sub>ULX</sub> has an SED which is relatively flat through the EUV, the addition of this component increases the intensity lines with ionization potentials  $\gtrsim 54$  eV such as He II  $\lambda 1640, 4686$  and [O IV]  $25.9\mu\text{m}$  by a factor of at least two relative to the BPASS SSPs alone. Emission line diagnostics including such lines can therefore be used to infer the presence of SXP<sub>ULX</sub> ionization.
- The intensity of very high-ionization lines (ionization potentials  $> 90$  eV) such as [Ne V]  $\lambda 3426$ ,  $14.3\mu\text{m}$  are strongly enhanced ( $> 10^5\times$ ) due to the addition of the SXP<sub>ULX</sub>; however, these lines are typically very weak in the simulations presented here (e.g.,  $\log(\tilde{f}_{\text{line}}/\tilde{f}_{\text{Pa}\beta}) \sim -6$  for coronal lines in the IR). This is due in large part to the fixed SXP<sub>ULX</sub> normalization relative to the SSP as a function of burst age and metallicity, where the maximum relative scaling is achieved for the lowest stellar metallicities. Because gas-phase and stellar metallicities are coupled in all simulations, the regime in which the SXP<sub>ULX</sub> reaches maximum ionizing contribution relative to the SSP is also the one where many elements have their lowest absolute abundances in the cloud, which can be the dominant factor in setting line intensity.
- SXP<sub>ULX</sub> photoionization is capable of reproducing the observed strengths of high-ionization emission line ratios (e.g., He II  $\lambda 4686/\text{H}\beta$ ), but primarily for instantaneous burst models with  $Z \lesssim 0.1 Z_{\odot}$  and  $t_{\text{burst}} > 10$  Myr. This is again a consequence of the coupling of the SXP<sub>ULX</sub> to the SSP as a fixed function of stellar metallicity and burst age. On timescales  $< 10$  Myr, the stellar ionizing continuum is still substantial, effectively diluting the SXP<sub>ULX</sub> ionizing output, particularly for high-ionization lines as measured relative to strong



nebular lines for which there is little  $\text{SXP}_{\text{ULX}}$  ionizing contribution. As a result, the  $\text{SXP}_{\text{ULX}}$  is unlikely to contribute significantly to producing strong high-ionization emission lines in galaxies with very recent ( $\lesssim 10$  Myr) bursts of star formation.

- Comparison of the simulation outputs to observations in terms of emission line ratios and/or typical X-ray observables (e.g.,  $L_X/\text{SFR}$ ) should be performed with careful consideration of the underlying assumptions, including  $\text{SXP}_{\text{ULX}}$  SED shape, cloud abundance patterns, assumed star formation history, and  $\text{SXP}_{\text{ULX}}$  detectability as a function of viewing angle and variability.
- Though the X-ray detectability of the  $\text{SXP}_{\text{ULX}}$  depends on viewing angle and duty cycle, the  $\text{SXP}_{\text{ULX}}$  production of high-ionization nebular emission lines is ubiquitous for the  $\text{SED}_{\text{ULX}}$  modeled here. This is due to the fact that the EUV and soft X-ray photons from the  $\text{SXP}_{\text{ULX}}$  emanate from the outflow component, which is assumed to be relatively isotropic. In this way, high-ionization emission lines can be indirect tracers of a transient or unfavorably oriented  $\text{SXP}_{\text{ULX}}$ .
- The outflow component of the  $\text{SXP}_{\text{ULX}}$  may additionally drive fast shocks and therefore shock ionization. We discuss complexities in joint modeling of shock and photoionization due to an  $\text{SXP}_{\text{ULX}}$ , and consider it a promising avenue for future study. This is particularly true given that  $\text{SXP}_{\text{ULX}}$  mechanical feedback due to a disk wind or outflow

could be similar in magnitude, if not timescale, to feedback from stellar winds and supernovae. As such, the  $\text{SXP}_{\text{ULX}}$  could contribute to conditions in the interstellar medium conducive to ionizing photon escape, and additionally provide a substantial number of soft (0.5–2 keV) photons that could directly contribute to heating the intergalactic medium prior to the epoch of reionization.

- 1 K.G.'s research was supported by an appointment
- 2 to the NASA Postdoctoral Program at NASA God-
- 3 dard Space Flight Center, administered by Oak
- 4 Ridge Associated Universities under contract with
- 5 NASA. We gratefully acknowledge support under NASA
- 6 award 80GSFC21M0002 (A.R.B., P.T.), NASA award
- 7 80NSSC22K0407 (K.G., A.R.B., P.T., A.H.), and *Chan-*
- 8 *dra* grant No. GO0-2JO76A (B.D.L., A.R.B.) C.R. ac-
- 9 knowledges the support of the Elon University Japheth
- 10 E. Rawls Professorship. K.G. would like to thank Jenna
- 11 Cann and Anna Ogorzałek for helpful conversations dur-
- 12 ing the preparation of this manuscript, and give a special
- 13 thanks to Nell Byler for inspiration.

*Software:* Cloudy (Ferland et al. 2017), CloudyFSPS (Byler 2018), FSPS (Conroy et al. 2009; Conroy & Gunn 2010), Python-FSPS (Johnson et al. 2023), XSPEC (Arnaud 1996), HEASoft (Nasa High Energy Astrophysics Science Archive Research Center (Heasarc) 2014), astropy (Astropy Collaboration et al. 2013, 2018, 2022), scipy (Virtanen et al. 2020), matplotlib (Hunter 2007), astroquery (Ginsburg et al. 2019), numpy (Harris et al. 2020)

## REFERENCES

- Abel, N. P., van Hoof, P. A. M., Shaw, G., Ferland, G. J., & Elwert, T. 2008, *ApJ*, 686, 1125, doi: [10.1086/591505](https://doi.org/10.1086/591505)
- Abolmasov, P., Karpov, S., & Kotani, T. 2009, *PASJ*, 61, 213, doi: [10.1093/pasj/61.2.213](https://doi.org/10.1093/pasj/61.2.213)
- Abolmasov, P. K., Swartz, D. A., Fabrika, S., et al. 2007, *ApJ*, 668, 124, doi: [10.1086/520828](https://doi.org/10.1086/520828)
- Allen, M. G., Groves, B. A., Dopita, M. A., Sutherland, R. S., & Kewley, L. J. 2008, *ApJS*, 178, 20, doi: [10.1086/589652](https://doi.org/10.1086/589652)
- Arellano-Córdova, K. Z., Berg, D. A., Chisholm, J., et al. 2022, *ApJL*, 940, L23, doi: [10.3847/2041-8213/ac9ab2](https://doi.org/10.3847/2041-8213/ac9ab2)
- Arnaud, K. A. 1996, in *Astronomical Society of the Pacific Conference Series*, Vol. 101, *Astronomical Data Analysis Software and Systems V*, ed. G. H. Jacoby & J. Barnes, 17
- Astropy Collaboration, Robitaille, T. P., Tollerud, E. J., et al. 2013, *A&A*, 558, A33, doi: [10.1051/0004-6361/201322068](https://doi.org/10.1051/0004-6361/201322068)
- Astropy Collaboration, Price-Whelan, A. M., Sipőcz, B. M., et al. 2018, *AJ*, 156, 123, doi: [10.3847/1538-3881/aabc4f](https://doi.org/10.3847/1538-3881/aabc4f)
- Astropy Collaboration, Price-Whelan, A. M., Lim, P. L., et al. 2022, *ApJ*, 935, 167, doi: [10.3847/1538-4357/ac7c74](https://doi.org/10.3847/1538-4357/ac7c74)
- Bachetti, M., Harrison, F. A., Walton, D. J., et al. 2014, *Nature*, 514, 202, doi: [10.1038/nature13791](https://doi.org/10.1038/nature13791)
- Bachetti, M., Heida, M., Maccarone, T., et al. 2022, *ApJ*, 937, 125, doi: [10.3847/1538-4357/ac8d67](https://doi.org/10.3847/1538-4357/ac8d67)
- Baldwin, J. A., Ferland, G. J., Martin, P. G., et al. 1991, *ApJ*, 374, 580, doi: [10.1086/170146](https://doi.org/10.1086/170146)
- Basu-Zych, A. R., Lehmer, B., Fragos, T., et al. 2016, *ApJ*, 818, 140, doi: [10.3847/0004-637X/818/2/140](https://doi.org/10.3847/0004-637X/818/2/140)

- Basu-Zych, A. R., Lehmer, B. D., Hornschemeier, A. E., et al. 2013, *ApJ*, 774, 152, doi: [10.1088/0004-637X/774/2/152](https://doi.org/10.1088/0004-637X/774/2/152)
- Begelman, M. C., King, A. R., & Pringle, J. E. 2006, *MNRAS*, 370, 399, doi: [10.1111/j.1365-2966.2006.10469.x](https://doi.org/10.1111/j.1365-2966.2006.10469.x)
- Belczynski, K., & Taam, R. E. 2008, *ApJ*, 685, 400, doi: [10.1086/590551](https://doi.org/10.1086/590551)
- Berg, D. A., Chisholm, J., Erb, D. K., et al. 2019, *ApJL*, 878, L3, doi: [10.3847/2041-8213/ab21dc](https://doi.org/10.3847/2041-8213/ab21dc)
- . 2021, *ApJ*, 922, 170, doi: [10.3847/1538-4357/ac141b](https://doi.org/10.3847/1538-4357/ac141b)
- Berg, D. A., Erb, D. K., Auger, M. W., Pettini, M., & Brammer, G. B. 2018, *ApJ*, 859, 164, doi: [10.3847/1538-4357/aab7fa](https://doi.org/10.3847/1538-4357/aab7fa)
- Berghea, C. T., & Dudik, R. P. 2012, *ApJ*, 751, 104, doi: [10.1088/0004-637X/751/2/104](https://doi.org/10.1088/0004-637X/751/2/104)
- Berghea, C. T., Dudik, R. P., Weaver, K. A., & Kallman, T. R. 2010, *ApJ*, 708, 364, doi: [10.1088/0004-637X/708/1/364](https://doi.org/10.1088/0004-637X/708/1/364)
- Brightman, M., Kosec, P., Fürst, F., et al. 2022, *ApJ*, 929, 138, doi: [10.3847/1538-4357/ac5e37](https://doi.org/10.3847/1538-4357/ac5e37)
- Brightman, M., Harrison, F. A., Fürst, F., et al. 2018, *Nature Astronomy*, 2, 312, doi: [10.1038/s41550-018-0391-6](https://doi.org/10.1038/s41550-018-0391-6)
- Brinchmann, J., Kunth, D., & Durret, F. 2008, *A&A*, 485, 657, doi: [10.1051/0004-6361/200809783](https://doi.org/10.1051/0004-6361/200809783)
- Brorby, M., & Kaaret, P. 2017, *MNRAS*, 470, 606, doi: [10.1093/mnras/stx1286](https://doi.org/10.1093/mnras/stx1286)
- Byler, N. 2018, *cloudyFSPS*, 1.0.0, Zenodo, doi: [10.5281/zenodo.1156412](https://doi.org/10.5281/zenodo.1156412)
- Byler, N., Dalcanton, J. J., Conroy, C., & Johnson, B. D. 2017, *ApJ*, 840, 44, doi: [10.3847/1538-4357/aa6c66](https://doi.org/10.3847/1538-4357/aa6c66)
- Byler, N., Dalcanton, J. J., Conroy, C., et al. 2018, *ApJ*, 863, 14, doi: [10.3847/1538-4357/aacd50](https://doi.org/10.3847/1538-4357/aacd50)
- Cann, J. M., Satyapal, S., Abel, N. P., et al. 2018, *ApJ*, 861, 142, doi: [10.3847/1538-4357/aac64a](https://doi.org/10.3847/1538-4357/aac64a)
- Carpano, S., Haberl, F., Maitra, C., & Vasilopoulos, G. 2018, *MNRAS*, 476, L45, doi: [10.1093/mnrasl/sly030](https://doi.org/10.1093/mnrasl/sly030)
- Cleri, N. J., Olivier, G. M., Hutchison, T. A., et al. 2023, *arXiv e-prints*, arXiv:2301.07745, doi: [10.48550/arXiv.2301.07745](https://doi.org/10.48550/arXiv.2301.07745)
- Colbert, E. J. M., & Mushotzky, R. F. 1999, *ApJ*, 519, 89, doi: [10.1086/307356](https://doi.org/10.1086/307356)
- Conroy, C. 2013, *ARA&A*, 51, 393, doi: [10.1146/annurev-astro-082812-141017](https://doi.org/10.1146/annurev-astro-082812-141017)
- Conroy, C., & Gunn, J. E. 2010, *ApJ*, 712, 833, doi: [10.1088/0004-637X/712/2/833](https://doi.org/10.1088/0004-637X/712/2/833)
- Conroy, C., Gunn, J. E., & White, M. 2009, *ApJ*, 699, 486, doi: [10.1088/0004-637X/699/1/486](https://doi.org/10.1088/0004-637X/699/1/486)
- Copperwheat, C., Cropper, M., Soria, R., & Wu, K. 2005, *MNRAS*, 362, 79, doi: [10.1111/j.1365-2966.2005.09223.x](https://doi.org/10.1111/j.1365-2966.2005.09223.x)
- Cseh, D., Corbel, S., Kaaret, P., et al. 2012, *ApJ*, 749, 17, doi: [10.1088/0004-637X/749/1/17](https://doi.org/10.1088/0004-637X/749/1/17)
- Das, A., Mesinger, A., Pallottini, A., Ferrara, A., & Wise, J. H. 2017, *MNRAS*, 469, 1166, doi: [10.1093/mnras/stx943](https://doi.org/10.1093/mnras/stx943)
- Doore, K., Monson, E. B., Eufrazio, R. T., et al. 2023, *arXiv e-prints*, arXiv:2304.06753, doi: [10.48550/arXiv.2304.06753](https://doi.org/10.48550/arXiv.2304.06753)
- Dopita, M. A., Kewley, L. J., Heisler, C. A., & Sutherland, R. S. 2000, *ApJ*, 542, 224, doi: [10.1086/309538](https://doi.org/10.1086/309538)
- Earnshaw, H. P., Roberts, T. P., & Sathyaprakash, R. 2018, *MNRAS*, 476, 4272, doi: [10.1093/mnras/sty501](https://doi.org/10.1093/mnras/sty501)
- Eldridge, J. J., Stanway, E. R., Xiao, L., et al. 2017, *PASA*, 34, e058, doi: [10.1017/pasa.2017.51](https://doi.org/10.1017/pasa.2017.51)
- Ferland, G. J., Chatzikos, M., Guzmán, F., et al. 2017, *RMxAA*, 53, 385. <https://arxiv.org/abs/1705.10877>
- Fragos, T., Lehmer, B. D., Naoz, S., Zezas, A., & Basu-Zych, A. 2013a, *ApJL*, 776, L31, doi: [10.1088/2041-8205/776/2/L31](https://doi.org/10.1088/2041-8205/776/2/L31)
- Fragos, T., Kalogera, V., Belczynski, K., et al. 2008, *ApJ*, 683, 346, doi: [10.1086/588456](https://doi.org/10.1086/588456)
- Fragos, T., Kalogera, V., Willems, B., et al. 2009, *ApJL*, 702, L143, doi: [10.1088/0004-637X/702/2/L143](https://doi.org/10.1088/0004-637X/702/2/L143)
- Fragos, T., Lehmer, B., Tremmel, M., et al. 2013b, *ApJ*, 764, 41, doi: [10.1088/0004-637X/764/1/41](https://doi.org/10.1088/0004-637X/764/1/41)
- Fürst, F., Walton, D. J., Harrison, F. A., et al. 2016, *ApJL*, 831, L14, doi: [10.3847/2041-8205/831/2/L14](https://doi.org/10.3847/2041-8205/831/2/L14)
- Garnett, D. R., Kennicutt, Robert C., J., Chu, Y.-H., & Skillman, E. D. 1991, *ApJ*, 373, 458, doi: [10.1086/170065](https://doi.org/10.1086/170065)
- Garofali, K. 2023, *kgarofali/sxp-cloudy: v1.0, v1.0*, Zenodo, doi: [10.5281/zenodo.8338911](https://doi.org/10.5281/zenodo.8338911)
- Garofali, K., Williams, B. F., Hillis, T., et al. 2018, *MNRAS*, 479, 3526, doi: [10.1093/mnras/sty1612](https://doi.org/10.1093/mnras/sty1612)
- Garofali, K., Lehmer, B. D., Basu-Zych, A., et al. 2020, *ApJ*, 903, 79, doi: [10.3847/1538-4357/abba2d](https://doi.org/10.3847/1538-4357/abba2d)
- Gierliński, M., Done, C., & Page, K. 2009, *MNRAS*, 392, 1106, doi: [10.1111/j.1365-2966.2008.14166.x](https://doi.org/10.1111/j.1365-2966.2008.14166.x)
- Gilbertson, W., Lehmer, B. D., Doore, K., et al. 2022, *ApJ*, 926, 28, doi: [10.3847/1538-4357/ac4049](https://doi.org/10.3847/1538-4357/ac4049)
- Ginsburg, A., Sipőcz, B. M., Brasseur, C. E., et al. 2019, *AJ*, 157, 98, doi: [10.3847/1538-3881/aafc33](https://doi.org/10.3847/1538-3881/aafc33)
- Gladstone, J. C., Copperwheat, C., Heinke, C. O., et al. 2013, *ApJS*, 206, 14, doi: [10.1088/0067-0049/206/2/14](https://doi.org/10.1088/0067-0049/206/2/14)
- Gladstone, J. C., Roberts, T. P., & Done, C. 2009a, *MNRAS*, 397, 1836, doi: [10.1111/j.1365-2966.2009.15123.x](https://doi.org/10.1111/j.1365-2966.2009.15123.x)
- . 2009b, *MNRAS*, 397, 1836, doi: [10.1111/j.1365-2966.2009.15123.x](https://doi.org/10.1111/j.1365-2966.2009.15123.x)

- Götberg, Y., de Mink, S. E., Groh, J. H., Leitherer, C., & Norman, C. 2019, *A&A*, 629, A134, doi: [10.1051/0004-6361/201834525](https://doi.org/10.1051/0004-6361/201834525)
- Grasha, K., Roy, A., Sutherland, R. S., & Kewley, L. J. 2021, *ApJ*, 908, 241, doi: [10.3847/1538-4357/abd6bf](https://doi.org/10.3847/1538-4357/abd6bf)
- Grevesse, N., Asplund, M., Sauval, A. J., & Scott, P. 2010, *Ap&SS*, 328, 179, doi: [10.1007/s10509-010-0288-z](https://doi.org/10.1007/s10509-010-0288-z)
- Grimm, H. J., Gilfanov, M., & Sunyaev, R. 2003, *MNRAS*, 339, 793, doi: [10.1046/j.1365-8711.2003.06224.x](https://doi.org/10.1046/j.1365-8711.2003.06224.x)
- Grisé, F., Kaaret, P., Corbel, S., et al. 2012a, *ApJ*, 745, 123, doi: [10.1088/0004-637X/745/2/123](https://doi.org/10.1088/0004-637X/745/2/123)
- . 2012b, *ApJ*, 745, 123, doi: [10.1088/0004-637X/745/2/123](https://doi.org/10.1088/0004-637X/745/2/123)
- Gúrpide, A., Parra, M., Godet, O., Contini, T., & Olive, J. F. 2022, *A&A*, 666, A100, doi: [10.1051/0004-6361/202142229](https://doi.org/10.1051/0004-6361/202142229)
- Guseva, N. G., Izotov, Y. I., & Thuan, T. X. 2000, *ApJ*, 531, 776, doi: [10.1086/308489](https://doi.org/10.1086/308489)
- Harris, C. R., Millman, K. J., van der Walt, S. J., et al. 2020, *Nature*, 585, 357, doi: [10.1038/s41586-020-2649-2](https://doi.org/10.1038/s41586-020-2649-2)
- Hatano, S., Ouchi, M., Umeda, H., et al. 2023, arXiv e-prints, arXiv:2305.02189, doi: [10.48550/arXiv.2305.02189](https://doi.org/10.48550/arXiv.2305.02189)
- Heida, M., Harrison, F. A., Brightman, M., et al. 2019a, *ApJ*, 871, 231, doi: [10.3847/1538-4357/aafa77](https://doi.org/10.3847/1538-4357/aafa77)
- Heida, M., Jonker, P. G., Torres, M. A. P., et al. 2016, *MNRAS*, 459, 771, doi: [10.1093/mnras/stw695](https://doi.org/10.1093/mnras/stw695)
- . 2014, *MNRAS*, 442, 1054, doi: [10.1093/mnras/stu928](https://doi.org/10.1093/mnras/stu928)
- Heida, M., Lau, R. M., Davies, B., et al. 2019b, *ApJL*, 883, L34, doi: [10.3847/2041-8213/ab4139](https://doi.org/10.3847/2041-8213/ab4139)
- HERA Collaboration, Abdurashidova, Z., Adams, T., et al. 2023, *ApJ*, 945, 124, doi: [10.3847/1538-4357/acaaf50](https://doi.org/10.3847/1538-4357/acaaf50)
- Hunter, J. D. 2007, *Computing in Science & Engineering*, 9, 90, doi: [10.1109/MCSE.2007.55](https://doi.org/10.1109/MCSE.2007.55)
- Israel, G. L., Belfiore, A., Stella, L., et al. 2017, *Science*, 355, 817, doi: [10.1126/science.aai8635](https://doi.org/10.1126/science.aai8635)
- Izotov, Y. I., Thuan, T. X., & Guseva, N. G. 2021, *MNRAS*, 508, 2556, doi: [10.1093/mnras/stab2798](https://doi.org/10.1093/mnras/stab2798)
- Izotov, Y. I., Thuan, T. X., & Privon, G. 2012, *MNRAS*, 427, 1229, doi: [10.1111/j.1365-2966.2012.22051.x](https://doi.org/10.1111/j.1365-2966.2012.22051.x)
- Jaskot, A. E., & Oey, M. S. 2013, *ApJ*, 766, 91, doi: [10.1088/0004-637X/766/2/91](https://doi.org/10.1088/0004-637X/766/2/91)
- Jaskot, A. E., & Ravindranath, S. 2016, *ApJ*, 833, 136, doi: [10.3847/1538-4357/833/2/136](https://doi.org/10.3847/1538-4357/833/2/136)
- Johnson, B., Foreman-Mackey, D., Sick, J., et al. 2023, *dfm/python-fsps: python-fsps v0.4.5rc1, v0.4.5rc1*, Zenodo, doi: [10.5281/zenodo.8384410](https://doi.org/10.5281/zenodo.8384410)
- Johnson, B. D., Leja, J., Conroy, C., & Speagle, J. S. 2021, *ApJS*, 254, 22, doi: [10.3847/1538-4365/abef67](https://doi.org/10.3847/1538-4365/abef67)
- Justham, S., & Schawinski, K. 2012, *MNRAS*, 423, 1641, doi: [10.1111/j.1365-2966.2012.20985.x](https://doi.org/10.1111/j.1365-2966.2012.20985.x)
- Kaaret, P., Brorby, M., Casella, L., & Prestwich, A. H. 2017, *MNRAS*, 471, 4234, doi: [10.1093/mnras/stx1945](https://doi.org/10.1093/mnras/stx1945)
- Kaaret, P., & Corbel, S. 2009, *ApJ*, 697, 950, doi: [10.1088/0004-637X/697/1/950](https://doi.org/10.1088/0004-637X/697/1/950)
- Kaaret, P., Feng, H., Wong, D. S., & Tao, L. 2010, *ApJL*, 714, L167, doi: [10.1088/2041-8205/714/1/L167](https://doi.org/10.1088/2041-8205/714/1/L167)
- Kehrig, C., Guerrero, M. A., Vílchez, J. M., & Ramos-Larios, G. 2021, *ApJL*, 908, L54, doi: [10.3847/2041-8213/abe41b](https://doi.org/10.3847/2041-8213/abe41b)
- Kehrig, C., Vílchez, J. M., Guerrero, M. A., et al. 2018, *MNRAS*, 480, 1081, doi: [10.1093/mnras/sty1920](https://doi.org/10.1093/mnras/sty1920)
- Kennicutt, Robert C., J. 1998, *ARA&A*, 36, 189, doi: [10.1146/annurev.astro.36.1.189](https://doi.org/10.1146/annurev.astro.36.1.189)
- Kennicutt, R. C., & Evans, N. J. 2012, *ARA&A*, 50, 531, doi: [10.1146/annurev-astro-081811-125610](https://doi.org/10.1146/annurev-astro-081811-125610)
- Kewley, L. J., Dopita, M. A., Leitherer, C., et al. 2013, *ApJ*, 774, 100, doi: [10.1088/0004-637X/774/2/100](https://doi.org/10.1088/0004-637X/774/2/100)
- King, A., & Lasota, J.-P. 2016, *MNRAS*, 458, L10, doi: [10.1093/mnrasl/slw011](https://doi.org/10.1093/mnrasl/slw011)
- King, A., Lasota, J.-P., & Kluźniak, W. 2017, *MNRAS*, 468, L59, doi: [10.1093/mnrasl/slx020](https://doi.org/10.1093/mnrasl/slx020)
- King, A., Lasota, J.-P., & Middleton, M. 2023, *NewAR*, 96, 101672, doi: [10.1016/j.newar.2022.101672](https://doi.org/10.1016/j.newar.2022.101672)
- King, A. R. 2009, *MNRAS*, 393, L41, doi: [10.1111/j.1745-3933.2008.00594.x](https://doi.org/10.1111/j.1745-3933.2008.00594.x)
- King, A. R., Davies, M. B., Ward, M. J., Fabbiano, G., & Elvis, M. 2001, *ApJL*, 552, L109, doi: [10.1086/320343](https://doi.org/10.1086/320343)
- Kosec, P., Pinto, C., Fabian, A. C., & Walton, D. J. 2018a, *MNRAS*, 473, 5680, doi: [10.1093/mnras/stx2695](https://doi.org/10.1093/mnras/stx2695)
- Kosec, P., Pinto, C., Walton, D. J., et al. 2018b, *MNRAS*, 479, 3978, doi: [10.1093/mnras/sty1626](https://doi.org/10.1093/mnras/sty1626)
- Kosec, P., Pinto, C., Reynolds, C. S., et al. 2021, *MNRAS*, 508, 3569, doi: [10.1093/mnras/stab2856](https://doi.org/10.1093/mnras/stab2856)
- Kovlakas, K., Fragos, T., Schaerer, D., & Mesinger, A. 2022, arXiv e-prints, arXiv:2207.09331, <https://arxiv.org/abs/2207.09331>
- Kovlakas, K., Zezas, A., Andrews, J. J., et al. 2020, *MNRAS*, 498, 4790, doi: [10.1093/mnras/staa2481](https://doi.org/10.1093/mnras/staa2481)
- Kramida, A., Yu. Ralchenko, Reader, J., & and NIST ASD Team. 2022, NIST Atomic Spectra Database (ver. 5.10), [Online]. Available: <https://physics.nist.gov/asd> [2023, April 21]. National Institute of Standards and Technology, Gaithersburg, MD.
- Kubota, A., & Done, C. 2018, *MNRAS*, 480, 1247, doi: [10.1093/mnras/sty1890](https://doi.org/10.1093/mnras/sty1890)
- Lau, R. M., Heida, M., Walton, D. J., et al. 2019, *ApJ*, 878, 71, doi: [10.3847/1538-4357/ab1b1c](https://doi.org/10.3847/1538-4357/ab1b1c)

- Lebouteiller, V., Péquignot, D., Cormier, D., et al. 2017, *A&A*, 602, A45, doi: [10.1051/0004-6361/201629675](https://doi.org/10.1051/0004-6361/201629675)
- Lehmer, B. D., Eufrazio, R. T., Basu-Zych, A., et al. 2022, *ApJ*, 930, 135, doi: [10.3847/1538-4357/ac63a7](https://doi.org/10.3847/1538-4357/ac63a7)
- Lehmer, B. D., Basu-Zych, A. R., Mineo, S., et al. 2016, *ApJ*, 825, 7, doi: [10.3847/0004-637X/825/1/7](https://doi.org/10.3847/0004-637X/825/1/7)
- Lehmer, B. D., Eufrazio, R. T., Markwardt, L., et al. 2017, *ApJ*, 851, 11, doi: [10.3847/1538-4357/aa9578](https://doi.org/10.3847/1538-4357/aa9578)
- Lehmer, B. D., Eufrazio, R. T., Tzanavaris, P., et al. 2019, arXiv e-prints. <https://arxiv.org/abs/1905.05197>
- Lehmer, B. D., Eufrazio, R. T., Basu-Zych, A., et al. 2021, *ApJ*, 907, 17, doi: [10.3847/1538-4357/abcec1](https://doi.org/10.3847/1538-4357/abcec1)
- Leitherer, C., Schaerer, D., Goldader, J. D., et al. 1999, *ApJS*, 123, 3, doi: [10.1086/313233](https://doi.org/10.1086/313233)
- Linden, T., Kalogera, V., Sepinsky, J. F., et al. 2010, *ApJ*, 725, 1984, doi: [10.1088/0004-637X/725/2/1984](https://doi.org/10.1088/0004-637X/725/2/1984)
- Lipunova, G. V. 1999, *Astronomy Letters*, 25, 508. <https://arxiv.org/abs/astro-ph/9906324>
- Liu, J.-F., Bregman, J. N., & Seitzer, P. 2004, *ApJ*, 602, 249, doi: [10.1086/380994](https://doi.org/10.1086/380994)
- López, K. M., Jonker, P. G., Heida, M., et al. 2019, *MNRAS*, 489, 1249, doi: [10.1093/mnras/stz2127](https://doi.org/10.1093/mnras/stz2127)
- Madau, P., & Dickinson, M. 2014, *ARA&A*, 52, 415, doi: [10.1146/annurev-astro-081811-125615](https://doi.org/10.1146/annurev-astro-081811-125615)
- Mapelli, M., Ripamonti, E., Zampieri, L., Colpi, M., & Bressan, A. 2010, *MNRAS*, 408, 234, doi: [10.1111/j.1365-2966.2010.17048.x](https://doi.org/10.1111/j.1365-2966.2010.17048.x)
- Middleton, M. J., Heil, L., Pintore, F., Walton, D. J., & Roberts, T. P. 2015, *MNRAS*, 447, 3243, doi: [10.1093/mnras/stu2644](https://doi.org/10.1093/mnras/stu2644)
- Middleton, M. J., & King, A. 2017, *MNRAS*, 470, L69, doi: [10.1093/mnrasl/slx079](https://doi.org/10.1093/mnrasl/slx079)
- Mineo, S., Gilfanov, M., & Sunyaev, R. 2012, *MNRAS*, 419, 2095, doi: [10.1111/j.1365-2966.2011.19862.x](https://doi.org/10.1111/j.1365-2966.2011.19862.x)
- Motch, C., Pakull, M. W., Grisé, F., & Soria, R. 2011, *Astronomische Nachrichten*, 332, 367, doi: [10.1002/asna.201011501](https://doi.org/10.1002/asna.201011501)
- Nasa High Energy Astrophysics Science Archive Research Center (Heasarc). 2014, HEASoft: Unified Release of FTOOLS and XANADU, Astrophysics Source Code Library, record ascl:1408.004. <http://ascl.net/1408.004>
- Nicholls, D. C., Sutherland, R. S., Dopita, M. A., Kewley, L. J., & Groves, B. A. 2017, *MNRAS*, 466, 4403, doi: [10.1093/mnras/stw3235](https://doi.org/10.1093/mnras/stw3235)
- Olivier, G. M., Berg, D. A., Chisholm, J., et al. 2022, *ApJ*, 938, 16, doi: [10.3847/1538-4357/ac8f2c](https://doi.org/10.3847/1538-4357/ac8f2c)
- Oskinova, L. M., & Schaerer, D. 2022, *A&A*, 661, A67, doi: [10.1051/0004-6361/202142520](https://doi.org/10.1051/0004-6361/202142520)
- Paczynski, B. 1992, *AcA*, 42, 145
- Pinto, C., Middleton, M. J., & Fabian, A. C. 2016, *Nature*, 533, 64, doi: [10.1038/nature17417](https://doi.org/10.1038/nature17417)
- Plat, A., Charlot, S., Bruzual, G., et al. 2019, *MNRAS*, 490, 978, doi: [10.1093/mnras/stz2616](https://doi.org/10.1093/mnras/stz2616)
- Polimera, M. S., Kannappan, S. J., Richardson, C. T., et al. 2022, *ApJ*, 931, 44, doi: [10.3847/1538-4357/ac6595](https://doi.org/10.3847/1538-4357/ac6595)
- Poutanen, J., Lipunova, G., Fabrika, S., Butkevich, A. G., & Abolmasov, P. 2007, *MNRAS*, 377, 1187, doi: [10.1111/j.1365-2966.2007.11668.x](https://doi.org/10.1111/j.1365-2966.2007.11668.x)
- Prestwich, A. H., Jackson, F., Kaaret, P., et al. 2015, *ApJ*, 812, 166, doi: [10.1088/0004-637X/812/2/166](https://doi.org/10.1088/0004-637X/812/2/166)
- Prestwich, A. H., Tsantaki, M., Zezas, A., et al. 2013, *ApJ*, 769, 92, doi: [10.1088/0004-637X/769/2/92](https://doi.org/10.1088/0004-637X/769/2/92)
- Ramambason, L., Lebouteiller, V., Bik, A., et al. 2022, *A&A*, 667, A35, doi: [10.1051/0004-6361/202243866](https://doi.org/10.1051/0004-6361/202243866)
- Richardson, C. T., Simpson, C., Polimera, M. S., et al. 2022, *ApJ*, 927, 165, doi: [10.3847/1538-4357/ac510c](https://doi.org/10.3847/1538-4357/ac510c)
- Schaerer, D. 1996, *ApJL*, 467, L17, doi: [10.1086/310193](https://doi.org/10.1086/310193)
- Schaerer, D., Fragos, T., & Izotov, Y. I. 2019, *A&A*, 622, L10, doi: [10.1051/0004-6361/201935005](https://doi.org/10.1051/0004-6361/201935005)
- Senchyna, P., Stark, D. P., Charlot, S., et al. 2021, *MNRAS*, 503, 6112, doi: [10.1093/mnras/stab884](https://doi.org/10.1093/mnras/stab884)
- Senchyna, P., Stark, D. P., Chevallard, J., et al. 2019, *MNRAS*, 488, 3492, doi: [10.1093/mnras/stz1907](https://doi.org/10.1093/mnras/stz1907)
- Senchyna, P., Stark, D. P., Mirocha, J., et al. 2020, *MNRAS*, 494, 941, doi: [10.1093/mnras/staa586](https://doi.org/10.1093/mnras/staa586)
- Senchyna, P., Stark, D. P., Vidal-García, A., et al. 2017, *MNRAS*, 472, 2608, doi: [10.1093/mnras/stx2059](https://doi.org/10.1093/mnras/stx2059)
- Shakura, N. I., & Sunyaev, R. A. 1973, *A&A*, 24, 337
- Shirazi, M., & Brinchmann, J. 2012, *MNRAS*, 421, 1043, doi: [10.1111/j.1365-2966.2012.20439.x](https://doi.org/10.1111/j.1365-2966.2012.20439.x)
- Simmonds, C., Schaerer, D., & Verhamme, A. 2021, *A&A*, 656, A127, doi: [10.1051/0004-6361/202141856](https://doi.org/10.1051/0004-6361/202141856)
- Soria, R., & Kong, A. 2016, *MNRAS*, 456, 1837, doi: [10.1093/mnras/stv2671](https://doi.org/10.1093/mnras/stv2671)
- Soria, R., Kuntz, K. D., Winkler, P. F., et al. 2012, *ApJ*, 750, 152, doi: [10.1088/0004-637X/750/2/152](https://doi.org/10.1088/0004-637X/750/2/152)
- Stanway, E. R., & Eldridge, J. J. 2019, *A&A*, 621, A105, doi: [10.1051/0004-6361/201834359](https://doi.org/10.1051/0004-6361/201834359)
- Stark, D. P. 2016, *ARA&A*, 54, 761, doi: [10.1146/annurev-astro-081915-023417](https://doi.org/10.1146/annurev-astro-081915-023417)
- Stasińska, G., Izotov, Y., Morisset, C., & Guseva, N. 2015, *A&A*, 576, A83, doi: [10.1051/0004-6361/201425389](https://doi.org/10.1051/0004-6361/201425389)
- Steidel, C. C., Strom, A. L., Pettini, M., et al. 2016, *ApJ*, 826, 159, doi: [10.3847/0004-637X/826/2/159](https://doi.org/10.3847/0004-637X/826/2/159)
- Sutton, A. D., Roberts, T. P., & Middleton, M. J. 2013, *MNRAS*, 435, 1758, doi: [10.1093/mnras/stt1419](https://doi.org/10.1093/mnras/stt1419)
- Tao, L., Feng, H., Grisé, F., & Kaaret, P. 2011, *ApJ*, 737, 81, doi: [10.1088/0004-637X/737/2/81](https://doi.org/10.1088/0004-637X/737/2/81)



- Telford, O. G., Chisholm, J., McQuinn, K. B. W., & Berg, D. A. 2021, *ApJ*, 922, 191, doi: [10.3847/1538-4357/ac1ce2](https://doi.org/10.3847/1538-4357/ac1ce2)
- Thuan, T. X., & Izotov, Y. I. 2005, *ApJS*, 161, 240, doi: [10.1086/491657](https://doi.org/10.1086/491657)
- Tranin, H., Webb, N., & Godet, O. 2023, arXiv e-prints, arXiv:2304.11216, doi: [10.48550/arXiv.2304.11216](https://doi.org/10.48550/arXiv.2304.11216)
- Umeda, H., Ouchi, M., Nakajima, K., et al. 2022, *ApJ*, 930, 37, doi: [10.3847/1538-4357/ac602d](https://doi.org/10.3847/1538-4357/ac602d)
- Urquhart, R., & Soria, R. 2016, *MNRAS*, 456, 1859, doi: [10.1093/mnras/stv2293](https://doi.org/10.1093/mnras/stv2293)
- Vink, J. S., de Koter, A., & Lamers, H. J. G. L. M. 2001, *A&A*, 369, 574, doi: [10.1051/0004-6361:20010127](https://doi.org/10.1051/0004-6361:20010127)
- Vinokurov, A., Fabrika, S., & Atapin, K. 2013, *Astrophysical Bulletin*, 68, 139, doi: [10.1134/S1990341313020028](https://doi.org/10.1134/S1990341313020028)
- Virtanen, P., Gommers, R., Oliphant, T. E., et al. 2020, *Nature Methods*, 17, 261, doi: [10.1038/s41592-019-0686-2](https://doi.org/10.1038/s41592-019-0686-2)
- Walton, D. J., Fuerst, F., Harrison, F., et al. 2013, *ApJ*, 779, 148, doi: [10.1088/0004-637X/779/2/148](https://doi.org/10.1088/0004-637X/779/2/148)
- Walton, D. J., Harrison, F. A., Grefenstette, B. W., et al. 2014, *ApJ*, 793, 21, doi: [10.1088/0004-637X/793/1/21](https://doi.org/10.1088/0004-637X/793/1/21)
- Walton, D. J., Bachetti, M., Fürst, F., et al. 2018, *ApJL*, 857, L3, doi: [10.3847/2041-8213/aabadc](https://doi.org/10.3847/2041-8213/aabadc)
- Weaver, K. A., Meléndez, M., Mushotzky, R. F., et al. 2010, *ApJ*, 716, 1151, doi: [10.1088/0004-637X/716/2/1151](https://doi.org/10.1088/0004-637X/716/2/1151)
- West, L., Garofali, K., Lehmer, B. D., et al. 2023, *ApJ*, 952, 22, doi: [10.3847/1538-4357/acd9aa](https://doi.org/10.3847/1538-4357/acd9aa)
- Wiktorowicz, G., Lasota, J.-P., Belczynski, K., et al. 2021, *ApJ*, 918, 60, doi: [10.3847/1538-4357/ac0cf7](https://doi.org/10.3847/1538-4357/ac0cf7)
- Wiktorowicz, G., Lasota, J.-P., Middleton, M., & Belczynski, K. 2019, *ApJ*, 875, 53, doi: [10.3847/1538-4357/ab0f27](https://doi.org/10.3847/1538-4357/ab0f27)
- Wiktorowicz, G., Sobolewska, M., Lasota, J.-P., & Belczynski, K. 2017, *ApJ*, 846, 17, doi: [10.3847/1538-4357/aa821d](https://doi.org/10.3847/1538-4357/aa821d)
- Wilms, J., Allen, A., & McCray, R. 2000, *ApJ*, 542, 914, doi: [10.1086/317016](https://doi.org/10.1086/317016)
- Yao, Y., & Feng, H. 2019, *ApJL*, 884, L3, doi: [10.3847/2041-8213/ab44c7](https://doi.org/10.3847/2041-8213/ab44c7)

## APPENDIX

**Table A.1.** Line list used in photoionization simulations, including vacuum wavelength, line identifier, and Cloudy specific identifier. Bolded lines are those available in FSPS. The full version of this table is available online.

Vacuum Wavelength (Å)	Line ID	Cloudy ID
(1)	(2)	(3)
917.473	O I 917.473	O 1 917.473A
917.726	O I 917.726	O 1 917.726A
917.970	O I 917.97	O 1 917.970A
918.147	P III 918.147	P 3 918.147A
918.493	Ar I 918.493	Ar 1 918.493A
...	...	...
1486.50	<b>N IV] 1486.5</b>	N 4 1486.50A
1533.43	Si II 1533.43	Si 2 1533.43A
1548.19	<b>C IV 1548.19</b> †	C 4 1548.19A
1550.78	<b>C IV 1550.78</b> †	C 4 1550.78A
1561.33	C I 1561.33	C 1 1561.33A
1577.10	C III 1577.1	C 3 1577.10A
1640.43	<b>He II 1640.43</b> *	He 2 1640.43A
...	...	...
242135.	[Ne V] <b>24.2135</b> μm‡	Ne 5 24.2065m
245191.	Fe II 24.5191μm	Fe 2 24.5120m
258906.	<b>O IV 25.8906</b> μm*	O 4 25.8832m
...	...	...
1455370.	<b>O I 145.537</b> μm	O 1 145.495m
1576810.	<b>C II 157.681</b> μm	C 2 157.636m
2053030.	<b>N II 205.303</b> μm	N 2 205.244m
3703750.	[C I] <b>370.375</b> μm	C 1 370.269m
6097650.	[C I] <b>609.765</b> μm	C 1 609.590m

Table A.1 *continued*

**Table A.1** (*continued*)

Vacuum Wavelength ( $\text{\AA}$ )	Line ID	Cloudy ID
(1)	(2)	(3)

\*Line that is strong relative to  $H\beta$  or  $Pa\beta$ , and strongly enhanced by the addition of the  $SXP_{ULX}$ , relative to SSP-only models.

†Line that is strong relative to  $H\beta$  or  $Pa\beta$ , but not strongly enhanced relative to SSP-only models.

‡Line that is weak relative to  $H\beta$  or  $Pa\beta$ , but strongly enhanced relative to SSP-only models.

||Line that is weak relative to  $H\beta$  or  $Pa\beta$  (or has zero flux), and is not strongly enhanced relative to SSP-only models.

NOTE—Criteria for strength relative to  $H\beta$  or  $Pa\beta$ , or enhancement relative to the SSP-only models are described in Section 5.1. Only lines with ionization potentials  $\geq 54$  eV are marked in the table according to the above criteria.

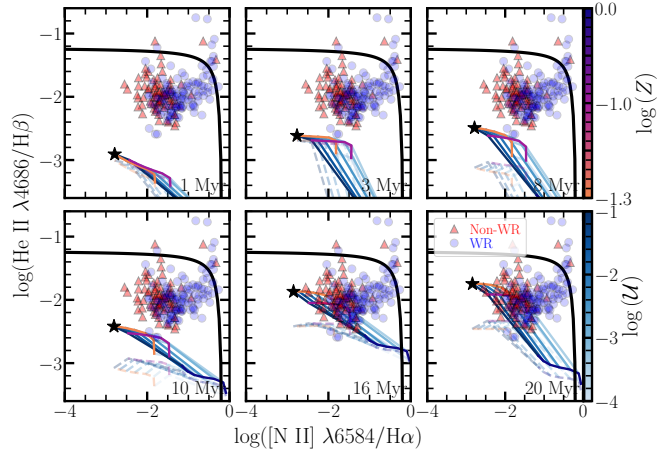


**Figure A.1.** Same as Figure 8, but with the strict delay-time dependence for the  $SXP_{ULX}$  removed. Here we show  $t_{\text{burst}} = 1\text{--}3$  Myr in the top left and center panels to illustrate the effect of allowing the  $SXP_{ULX}$  to form immediately with the corresponding SSP.

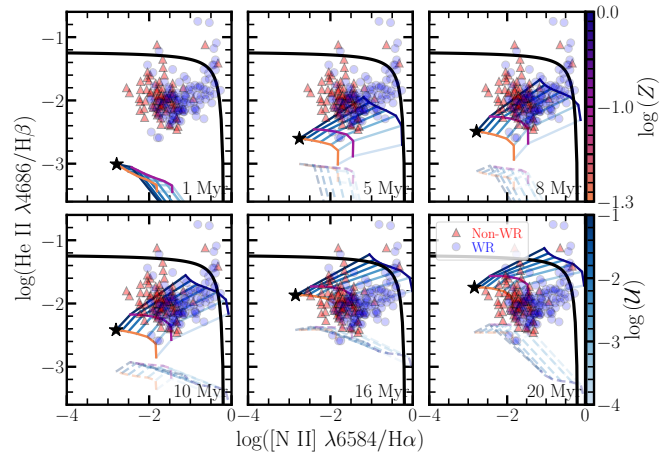


**Figure A.2.** Same as Figure 8, but with the strict correspondence of the metallicity dependence of the  $\text{SXP}_{\text{ULX}}$  relative to the SSP removed. In this case, the grid with  $\text{SXP}_{\text{ULX}}$  contribution overlaps with nearly the entire range of observed line ratios, even at very extreme  $\text{He II } \lambda 4686/\text{H}\beta$ , but requires extremely high, and therefore likely unphysical X-ray production efficiencies (i.e.,  $L_{\text{X}}/\text{SFR}$ ) for ULXs at high metallicity in order to do so.